

PHOTOLUMINESCENCE IMAGING OF
SEMICONDUCTOR STRUCTURES GROWN USING
SELECTIVE AREA EPITAXY

PHOTOLUMINESCENCE IMAGING OF SEMICONDUCTOR STRUCTURES GROWN
USING SELECTIVE AREA EPITAXY

By ALAA SHARAFELDIN, B.Sc

A Thesis Submitted to the School of Graduate Studies in Partial Fulfillment of the
Requirements for the Degree Master of Applied Science

McMaster University © Copyright by Alaa Sharafeldin, September 2022

MASTER OF APPLIED SCIENCE (2022)

McMaster University

Hamilton, Ontario

Department of Engineering Physics

TITLE: Photoluminescence Imaging of Semiconductor Structures Grown Using
Selective Area Epitaxy

AUTHOR: Alaa Sharafeldin, B.Sc (University of Waterloo)

SUPERVISOR: Professors R.N. Kleiman, R.B Lewis

NUMBER OF PAGES: ix, 89

Abstract

Selective Area Growth (SAG) is a technique developed for cost savings in semiconductor manufacturing, allowing for local area growth manipulation. In this work, SAG was accomplished by using a lithographic direct-write laser system that creates silica (SiO_2) masks on the surface of a III-V semiconductor substrate. The III-V semiconductor substrate used was a semi-insulating GaAs (SI-GaAs) wafer of (100) orientation. A lattice-matched InGaP/GaAs/InGaP heterostructure was grown using Molecular Beam Epitaxy (MBE). This heterostructure has a theoretical photoluminescence (PL) emission peak of approximately 875 nm and exhibited strong PL. A micro-photoluminescence (μ -PL) apparatus was successfully built and consists of a HeNe laser of 633 nm emission wavelength as the excitation source. The μ -PL apparatus captured the emission spectrum of the sample with a spatial resolution of approximately 6 μm and a peak wavelength around 878 nm. The images are scans of various area sizes, ranging from 0.0413-6.25 mm^2 . The images showed that the silica structures are non-growth sites due to the absence of PL. The images also showed a reduction in PL intensity in areas near silica structures. This is hypothesized to be due to variations in the InGaP layers that ultimately affect growth quality and carrier confinement. No change in PL wavelength was observed in the growth regions, as would be expected for a binary system grown by MBE. The PL imaging of selectively grown heterostructure materials enables further process development for integration of semiconductors with multiple bandgaps on a chip for fiber optic transmission.

Acknowledgements

I would like to thank my supervisors, Dr. Rafael Kleiman and Dr. Ryan Lewis, for their help and guidance throughout my graduate degree. To David McShannon, thank you for your great work ethic and teamwork throughout the project. To Syed Ali Zaidi, thank you for all your contributions in this work. To Paramita Bhattacharyya and Spencer McDermott, thank you for all your help and support. A special thank you to Doris Stevanovic, Shahram Tavakoli, and Nebile Isik for all your assistance and support in the CEDT facilities. I wish to extend my special thanks to my family and close friends who were always there to encourage me. Most importantly, my warm and heartfelt thanks go to my husband, Mohamed Moussa, for his tremendous support and encouragement.

Contents

1	Introduction	1
1.1	Motivation	1
1.1.1	Wavelength Division Multiplexing	2
1.2	Photonic Integrated Circuitry	4
2	Literature Review	7
2.1	III-V Semiconductors	7
2.2	Semiconductor Heterostructures	9
2.2.1	Quantum Well Lasers	12
2.3	Epitaxial Growth	15
2.3.1	Selective Area Growth	19
3	Experimental Methods	26
3.1	Semiconductor Wafer Processing	26
3.2	Micro-Photoluminescence Spectroscopy	33
4	Results & Discussion	41
4.1	Photoluminescence Imaging	41
4.2	Microscope Imaging	68
4.2.1	SEM Imaging	83
5	Conclusion & Future Work	84
6	References	86

List of Figures

1	Serial interface rates and WDM capacities of optical networks versus year. Reproduced from [6].	4
2	Sketch describing the effect of diffusion from a dielectric mask onto an open growth area, and the resulting longitudinal thickness modulation of the struc- tures. Reproduced from [9].	6
3	Band structure of GaAs. Reproduced from [13].	8
4	Schematic of a double heterostructure laser. Reproduced from [5].	10
5	Physical phenomena in classical heterostructures. Reproduced from [15] . . .	11
6	InGaN–GaN MQW laser. Reproduced from [26].	14
7	Bandgap as a function of lattice constant for III-V compounds and their ternary and quaternary alloys. Reproduced from [28].	15
8	MOCVD system schematic. Reproduced from [33].	18
9	Top view of a simple MBE chamber. Reproduced from [34].	18
10	Selective MOCVD process. Reproduced from [5].	20
11	Schematic of the growth pattern with the dimensions W_m , W_o , L , W_x , and W_y . Three points are also marked: $O(0,0)$, $M(0,W_y/2)$, and $N(W_x/2,0)$. Reproduced from [8].	24
12	Schematic of the periodic window calculation with governing equations and boundary conditions. Reproduced from [8].	24
13	One group in the full pattern. 400 μm scale.	28
14	Full pattern on quarter wafer. 2000 μm scale.	29

15	Sample after developing: the photoresist is removed except on the structures.	30
16	Sample after etching: the silica is removed except on the structures.	31
17	Processed sample before growth.	32
18	Semiconductor heterostructure grown using molecular beam epitaxy.	32
19	Micro-photoluminescence apparatus schematic.	35
20	MBE patterned growth of InGaP/GaAs/InGaP on SI-GaAs.	36
21	MBE uniform growth of InGaP/GaAs/InGaP on SI-GaAs.	36
22	Optical path.	39
23	Full setup.	40
24	Scan 1.	43
25	Scan 2.	44
26	Scan 3.	45
27	Scan 4.	46
28	Scan 5.	47
29	Scan 6.	48
30	Scan 7.	49
31	Scan 8.	50
32	Scan 9.	51
33	Scan 10.	52
34	Scan 11.	53
35	Scan 12.	54
36	Scan 13.	55
37	Scan 14.	56

38	Scan 15.	57
39	Scan 16.	58
40	PL intensity of the X values corresponding to Y = 8883 of Scan 12.	63
41	Peak wavelength of the Scans 9-11.	65
42	Histogram of peak wavelength of the Scans 9-11.	66
43	Histogram of peak voltage of the Scans 9-11.	66
44	Peak voltage of the Scans 9-11.	67
45	5x objective.	69
46	10x objective.	70
47	20x objective: vertical structures.	71
48	20x objective: horizontal structures.	72
49	20x objective: diagonal structures.	73
50	50x objective: vertical structures.	74
51	50x objective: horizontal structures.	75
52	50x objective: diagonal structures.	76
53	100x objective: vertical structures.	77
54	100x objective: vertical structures.	78
55	100x objective: horizontal structures.	79
56	100x objective: vertical structures with curved side.	80
57	100x objective: horizontal structures with curved side.	81
58	100x objective: vertical tapered structures with curved side.	82
59	SEM of the InGaAs/GaAs quantum well structure.	83

List of Tables

1	Summary of photoluminescence images.	42
---	--	----

1 Introduction

1.1 Motivation

A photonic integrated circuit (PIC) is an optical circuit that contains components that work with light. PICs offer advantages such as miniaturization, higher speed, low thermal effects, and large integration capacity [1]. PICs also allow for compatibility with existing process flows that allow for high yield, volume manufacturing, and lower prices [1]. The use of light instead of electricity to drive the photonic components is much faster for data transmission and communication and offers a solution to the limitations of electronics such as integration and heat generation [1].

Fiber optics communication is a method of transmitting information by sending pulses of light through an optical fiber. The benefits of using fiber networks are high bandwidth, low attenuation, low interference, high security, and high reliability over long distances [2]. An optical fiber is a flexible transparent optical waveguide used to carry propagating light [2]. The light pulses transport communication signals between devices. Optical fibres are composed of two coaxial layers: core, and cladding. The core is the inner part of the optical fiber and is used to guide the light. The core is surrounded by cladding which is a glass or plastic layer [3]. The cladding is characterized by a refractive index that is lower compared to the core refractive index, confining the light by total internal reflection to propagate through the core [3]. Fiber optic cables with small inner cores (10 μm or less) have only one path for the light and are referred to as single-mode fiber [3]. Fiber optic cables with larger cores (50 and 62.5 μm) have multiple paths for the light and are referred to as multimode [3]. The cladding of both types of fiber is a standard value of 125 μm [3]. Single-mode fibres are

capable of wide bandwidths, therefore making them ideal for long-haul and high-capacity circuits [4].

Waveguide dispersion causes the broadening of light pulses and is a critical factor limiting the quality of signal transmission of an optical fiber. Silica-based optical fibers have zero dispersion near 1300 nm wavelength and have lowest loss near 1550 nm wavelength [5]. Therefore, semiconductor lasers emitting near 1300 nm and 1550 nm are of interest for fiber optic transmission applications [5]. Many of the fiber optic transmission systems are deployed using InGaAsP/InP materials operating at these wavelengths [5]. Initially these lasers were fabricated using liquid phase epitaxy (LPE) [5]. As the growth techniques developed over time, metal-organic chemical vapour deposition (MOCVD) and molecular beam epitaxy (MBE) improved the quality of the devices [5]. The fabrication processes were further improved when advancements in laser designs such as quantum wells were incorporated.

1.1.1 Wavelength Division Multiplexing

Wavelength division multiplexing (WDM) is a fiber optics transmission technique that enables the use of multiple light wavelengths to send data over the same medium [5]. Signals of many different wavelengths are simultaneously modulated via multiplexing and transmitted through a single fiber [5]. The received signal with many wavelengths is optically demultiplexed into separate channels, which are then processed electronically in a conventional form [5]. Such a WDM system requires transmitters with many lasers at specific wavelengths. Like electronic circuits, it is ideal to have all these laser sources on a single chip for compactness and ease of fabrication [5]. This is very important for transporting large amounts of data between sites; instead of using one fiber per data needed to transmit,

one fiber is used for many wavelengths/frequencies of data. WDM has applications in fields including computer networking and broadcasting, internet and cable television, undersea environments, military, space, and medical [6]. Given the long-haul applications of WDM systems, most WDM systems operate on single mode fibres [5].

The evolution of electronic circuitry is approaching a plateau due to the quantum mechanical effects of decreasing feature sizes. In electronic circuitry, Moore's law states that the number of transistors on a chip doubles every two years while the cost is halved. The market demand for higher capacity transmission was amplified by the fact that computers continued to become more powerful and needed to be interconnected [5]. This higher capacity transmission demand of optical fiber technology parallels that of computer processing. These technologies have combined to meet the explosive global demand for new information services including data, internet, and broadband services [5].

There have been tremendous advancements in semiconductor lasers which led to worldwide deployments over the last few decades. Using WDM, the bandwidth of a fiber can be divided into many channels supporting a combined bit rate in the range of hundreds of terabits per second, as seen in Figure 1 [6]. This is a significant advancement considering the first WDM systems were developed in the 1980s and combined only two signals [5]. The need for higher capacity is pushing the deployment of WDM-based transmission, which needs tunable or frequency-settable lasers [5]. An important research area will continue to be the development of lasers with very stable and settable frequency. Integration of many such lasers on a single substrate will provide the ideal source for WDM systems. Advancements in laser development will not be possible without advancements in semiconductor material processing. A major challenge in improving laser technology is directly linked to

challenges in material growth. This includes the investigation of new material systems along with improvements in existing technologies to allow more reliable, cheaper, reproducible, and predictable devices.

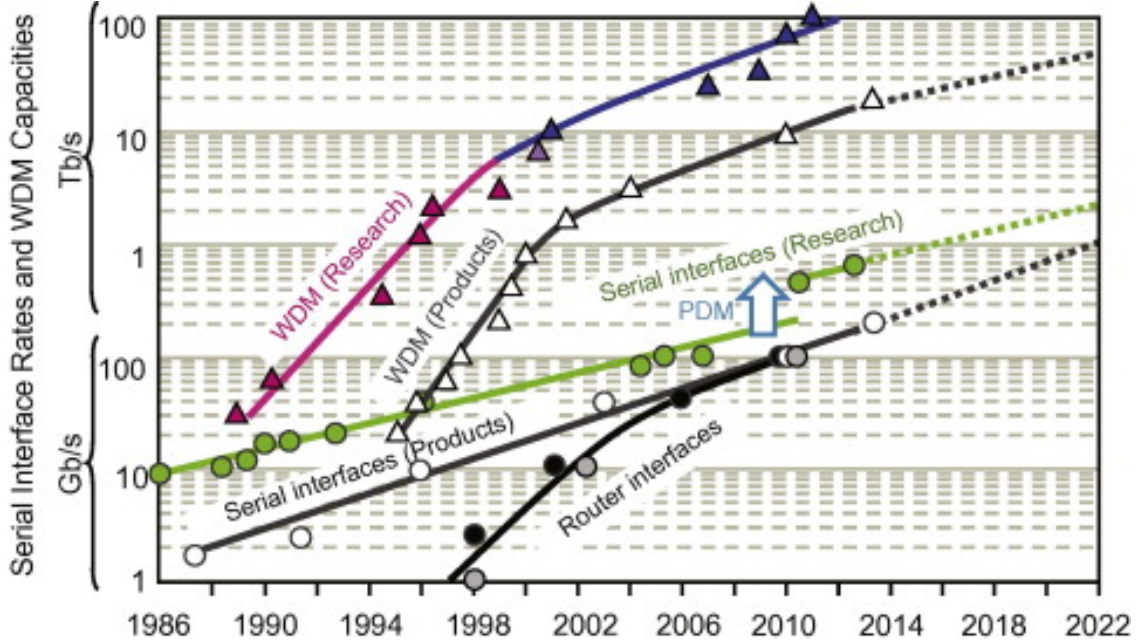


Figure 1: Serial interface rates and WDM capacities of optical networks versus year. Reproduced from [6].

1.2 Photonic Integrated Circuitry

The exploration of manufacturing techniques is of high priority in order to meet the demands of higher capacity transmission of optical fibres. Single-chip integration of functional components of a semiconductor optical device necessitates multiple wavelengths on a chip [7]. Selective Area Growth (SAG) is a technique that was developed for cost savings in semiconductor manufacturing, allowing for local area semiconductor growth manipulation [7]. SAG is a growth method that is used by varying the local epitaxial growth formation on the surface of a substrate [7]. This then allows the localized growth of quantum wells; a

heterostructure design that is of incredible importance to semiconductor devices.

To achieve regions with multiple semiconductor bandgaps in a single growth using SAG, a mask made of a dielectric amorphous layer is used to outline certain regions on the semiconductor substrate [8]. Provided that the active precursors in the growth do not nucleate on dielectric amorphous surfaces, they diffuse and allow growth in certain regions of the semiconductor, i.e in the vicinity of the masked zone [8]. In the case of ternary or quaternary III-V semiconductors, the mask induces a spatial compositional shift and thickness variation due to the different decomposition and diffusion rates of group-III elements [8]. This compositional shift produces a bandgap variation around the mask, thus achieving regions with multiple semiconductor bandgaps in a single growth. Figure 2 shows the thickness variation of the growth due to the effect of the diffusion from the dielectric mask. The bandgap is the key parameter used in producing the laser emission wavelength. SAG can be used to vary local material growths with an emission spectra that is altered laterally across the semiconductor wafer. This is controlled via the masking structures of the amorphous dielectric that affect the thickness and stoichiometry of the growth [7].

In this work, SAG is accomplished by using a laser-based direct-write lithography system that created masks on silica (SiO_2) films that were deposited on the surface of a III-V semiconductor substrate. The III-V semiconductor substrate used was a semi-insulating GaAs (SI-GaAs) of (100) orientation wafer, with approximately 100 nm of silica deposited. An InGaP/GaAs/InGaP structure was grown using MBE. This heterostructure device is fabricated between the silica mask regions and has a theoretical photoluminescence (PL) emission peak of approximately 875 nm. A micro-photoluminescence (μ -PL) apparatus was successfully built to capture the emission spectra of the sample with spatial resolution. The

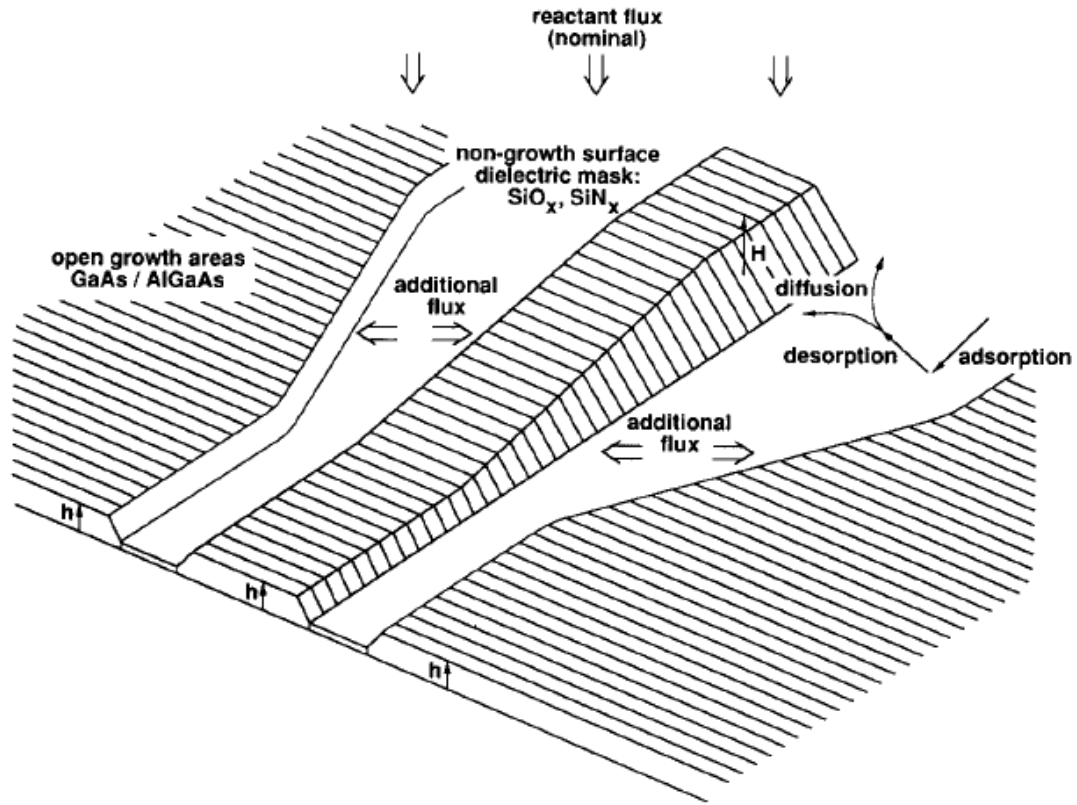


Figure 2: Sketch describing the effect of diffusion from a dielectric mask onto an open growth area, and the resulting longitudinal thickness modulation of the structures. Reproduced from [9].

emission spectrum is measured at a single wavelength across the sample, producing a map of PL intensity readings. These images are analyzed to understand the effect of silica masking on MBE growth. Ultimately, SAG will allow for the development of faster, more reliable, and cheaper methods for manufacturing at the device level.

2 Literature Review

2.1 III-V Semiconductors

Optoelectronic devices such as light emitting diodes (LEDs), semiconductor lasers, photodetectors, and some solar cells are composed of III-V semiconductor materials. A III-V semiconductor is an alloy containing elements from groups III and V in the periodic table. In photonic circuitry, III-V semiconductors are dominant due to their high performance, with InP being the most commercially used as it has high electron velocity [10]. In electronic circuitry, silicon is the dominant semiconductor. III-V semiconductors are the basis for photonic integrated circuits due to their unique optical properties such as high electron mobility, direct energy bandgap, and low exciton binding energy [11]. Among the most common III-V materials are GaAs, InAs, GaN, InN, InP, and their alloys. III-V ternary and quaternary alloy systems are of great importance for many high-speed electronic and optoelectronic devices due to their natural means of tuning the bandgap during SAG. Most semiconductor optoelectronics technologies are based on the epitaxial growth of compound semiconductor films (such as InGaAs, InGaP, GaAsP alloys) on binary compound semiconductor substrates (such as GaAs or InP wafers) [5].

The bandgap of a semiconductor is measured using PL spectroscopy, where the peak emission wavelength is inversely proportional to the bandgap:

$$E = \frac{hc}{\lambda} \approx \frac{1242 \text{ eV nm}}{\lambda} \quad (2.1)$$

where E is the energy, h is Planck's constant, c is the speed of light, and λ is the

wavelength. The bandgap is the minimum amount of energy required to excite an electron into the conduction band [12]. It is the energy difference between the maximum-energy state in the valence band and the minimum-energy state in the conduction band. In the case of GaAs, 1.42 eV is the bandgap, and therefore it has an emission wavelength of approximately 875 nm [13]. Figure 3, the band structure of GaAs, shows the energy vs wavevector of GaAs. GaAs has a direct energy bandgap at room temperature, meaning there is no momentum component between the valence band and conduction band.

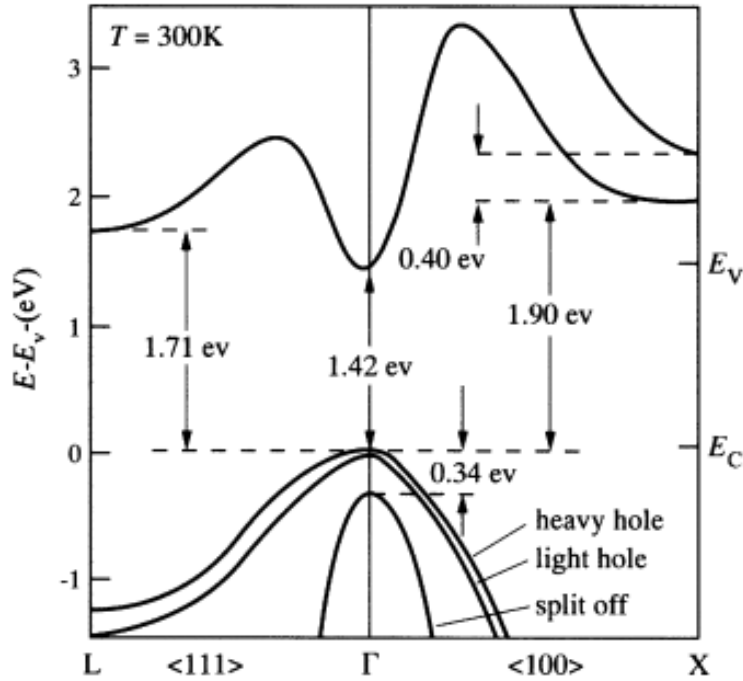


Figure 3: Band structure of GaAs. Reproduced from [13].

PL of a semiconductor is classified by the energy of the exciting photon with respect to the emission [14]. When supplied with sufficient energy (a minimum value equal to the bandgap) via a light source, a charged carrier is excited from the valence band into the conduction band and will release the energy in the form of light (proportional to the bandgap) as it

relaxes back into the valence band [14]. PL is an important technique for measuring the purity and quality of crystalline structures and/or growth of semiconductors.

2.2 Semiconductor Heterostructures

Semiconductor heterostructures, particularly double heterostructures (DHs), constitute two thirds of semiconductor physics research [15]. Heterostructures, including quantum wells, wire, and dots, allow the control of fundamental parameters inside the semiconductor crystals and devices such as bandgaps, effective masses of the charge carriers, electron energy spectrum, refractive indices, etc. [15]. Classical lasers started with a homojunction structure, i.e., a single material. However, these lasers were not efficient due to the high optical and electrical losses; threshold currents were very high, and lasing required low temperature [15]. Other homojunction-based devices at the time, such as LEDs, had very low efficiency due to high internal losses. The concept of a DHs was introduced in 1963 to confine carriers in the active region of the structure [15]. Kroemer proposed that “laser action should be obtainable in many of the indirect gap semiconductors and improved in the direct gap ones, if [it] is possible to supply them with a pair of heterojunction injectors” [15]. A DH is formed when a larger bandgap semiconductor is used as the outer layers (cladding) of a smaller bandgap material [5][16]. The interface of dissimilar material is referred to as the junction; there are two junctions in the DH. As seen in Figure 4, one of the cladding layers is p-doped and the other n-doped while the active region is undoped, forming a p-i-n structure. When current is applied, charged carriers (electrons and holes) are injected into the heterostructures and are confined in the active region. This is due to the smaller bandgap of the active region

causing an energy discontinuity at the junctions. By confining carriers within the active region, the threshold of the required current density is reduced and more electron-hole (e-h) pairs are available for the laser optical amplification process [5][15].

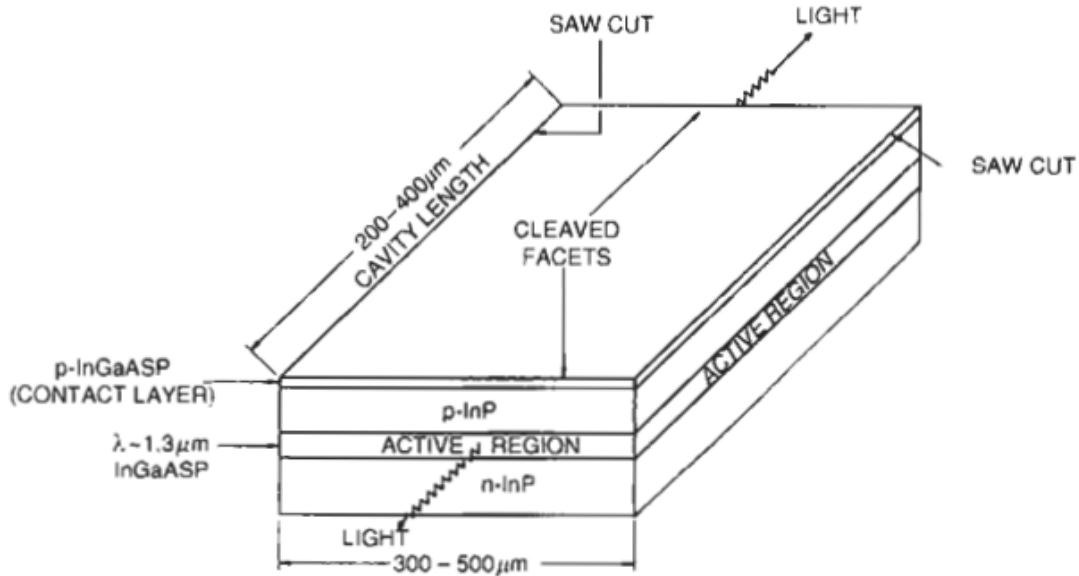


Figure 4: Schematic of a double heterostructure laser. Reproduced from [5].

The semiconductor heterostructure allows the superinjection of carriers, optical confinement, and electron confinement (Figure 5) [15]. The superinjection of carriers is attributed to the smaller bandgap active layer, where there is an increase in the concentration of electrons and holes when a forward bias is applied. The carrier concentration in this active region reaches values that are orders of magnitude higher than those in the outer layers, allowing more electrons and holes to radiatively recombine [15].

Optical confinement describes how “large” or “wide” the light mode is in the active region of the DH. In principle, there are two general mechanisms of optical confinement in semiconductor laser structures: index-guiding and gain-guiding [17]. Index-guiding refers to

the variation of the refractive index which leads to the wave-guiding effect while in the case of gain-guiding, the optical gain/loss variation provides a directional light propagation [17]. The optical confinement is quantified with the parameter Γ , the optical confinement factor. The optical confinement factor is defined as the fraction of the squared electric field confined to the active region [18]. It is an important parameter used to calculate the threshold current for semiconductor lasers.

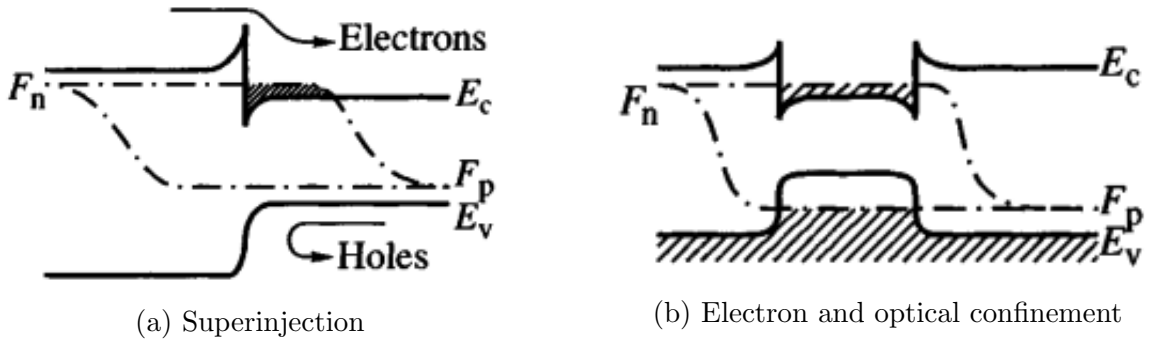


Figure 5: Physical phenomena in classical heterostructures. Reproduced from [15]

Excitons are fundamental electronic excitations in semiconductor materials associated to bound states of e-h pairs [19]. The electron and hole in the exciton are confined to an exciton Bohr radius and exist in a continuous band of energy states. Equations 2.2 and 2.3 correspond to the exciton energy and radius associated in a bulk semiconductor, respectively:

$$R^* = \frac{2m_{re}^*e^4}{\hbar^2(8\pi\epsilon)^2} \quad (2.2)$$

$$a_B^* = \frac{4\pi\epsilon\hbar^2}{m_{re}^*e^2} \quad (2.3)$$

where m_{re}^* is the reduced mass of the e-h pair, and ϵ is the permittivity of the semiconductor [19]. This electron confinement is of significant importance for DHs because in cases such as

quantum wells, the carriers can be confined further.

Non-radiative recombination mechanisms such as Shockley Read Hall (SRH) and Auger recombinations limit the performance of laser devices. The presence of impurities in the semiconductor materials gives rise to “localized states” in the bandgap, ultimately affecting the lifetime of carriers [20]. SRH recombination is a phenomenon in which carriers are trapped and lose their energy to localized states [21]. In this case, a photon is not released due to the carrier being non-radiatively recombined with a localized state. Auger recombination is a process in which the excess energy from an electron-hole recombination is transferred to electrons or holes (which then become excited) instead of giving off photons [22]. Both SRH and Auger recombination mechanisms provide non-radiative pathways in many different semiconductor devices, limiting the overall efficiency.

2.2.1 Quantum Well Lasers

The most important parameter of a heterostructure is the active region thickness. The quantum well (QW) laser is a special case of the DH laser where the active region is very thin, less than 10 nm, rather than the typical range of 0.1-0.3 μm [16][23]. When the thickness of the active layer is reduced, the carriers are forced to exist in bound states with discrete allowed energies. This reduces the density of states to a “two-dimensional-like” density of states where the system is quantum confined in the direction perpendicular to the plane (z-growth direction) of the material [24]. This modification of the density of states results in several improvements in laser characteristics such as lower threshold current, higher efficiency, higher modulation bandwidth, and lower continuous wave and dynamic spectral width [25]. The reduction in dimension influences the exciton energy and

radius of the carriers, allowing enhanced excitonic effects. In summary, QW lasers have two main differences with DH lasers: (i) The number of available quantum states in the active region is strongly diminished because the thickness modulation reduces the allowed values of momentum to one or a few quantized values in the z-direction whereas the number in a DH laser would amount to a few tens; (ii) The efficiency of the emitted photons to interact with e-h pairs to induce another stimulated recombination process is strongly reduced due to poor optical confinement [24]. This is because at very small thicknesses, the waveguiding properties of a DH are poor, and the confined optical wave tends to one wavelength [24]. In addition, the rather wide optical wave has an overlap with the active layer which diminishes as d (thickness) [24]. Therefore both effects tend to diminish the optical confinement factor as d^2 , and can be approximated by:

$$\Gamma \approx \left(\frac{d}{\lambda_0}\right)^2 (2\pi)^2 n \Delta n \quad (2.4)$$

where λ_0 is the wavelength in vacuum, n and Δn are the average and differences in indices of the refractive indices of the materials, respectively [24].

It has been found that it is more favourable to fabricate a laser using multiple quantum wells (MQWs) due to increased device performance. MQW lasers have a larger density of states; the potential barrier of the confining material is the highest and therefore limits carrier leaking [24]. Gain appears at lower injected current for single quantum wells (SQWs) than in MQWs due to the smaller density of states in the SQW [24]. QW lasers must operate at high volume-gain and thus high-carrier densities. Auger recombination dominates at higher carrier densities and is increased in SQWs, making MQWs preferred for lasers [24].

Figure 6 shows an InGaN-GaN laser fabricated using MQWs. The device consists of a sapphire substrate, followed by a GaN buffer layer, an n-doped GaN contact layer, an active zone, and then finally a p-doped contact layer. Using MOCVD, GaN epilayers are deposited on the surface of patterned sapphire substrate, where the patterning is done by dry etching [27]. Ammonia (NH_3) is used as a nitrogen source as it dissociates during growth and atomic hydrogen is present in the crystal structure [20]. If Mg is present in the crystal, a magnesium hydrogen complex is formed (Mg-H) [20]. Thermal annealing allows the hydrogen to diffuse out of the crystal, resulting in a p-type GaN [20]. The GaN buffer layer is grown first because it has been experimentally shown to have higher electron mobility which is a contributing factor in the quality of the crystal [20]. On the other hand, an n-type doped semiconductor can be achieved by using silicon doping from a compound such as Silane [27].

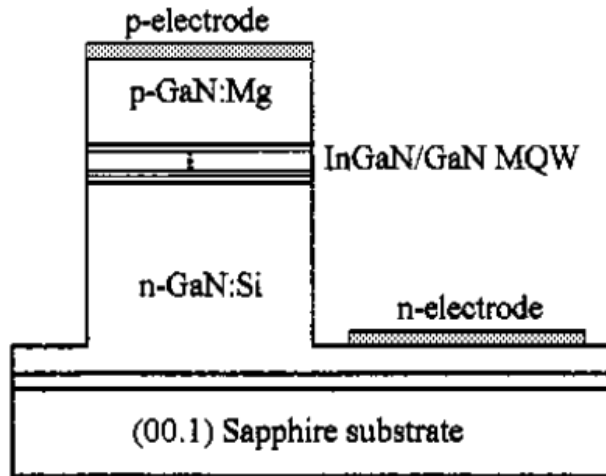


Figure 6: InGaN-GaN MQW laser. Reproduced from [26].

2.3 Epitaxial Growth

Having multiple layers of different materials gives rise to limitations in device performance due to lattice mismatch, strain, and high dislocation density. The lattice mismatch is quantified by the lattice constant of a semiconductor; the spacing in angstroms of the atoms in the crystal of that material [29]. Figure 7 shows the bandgap vs lattice constant for common III-V semiconductors.

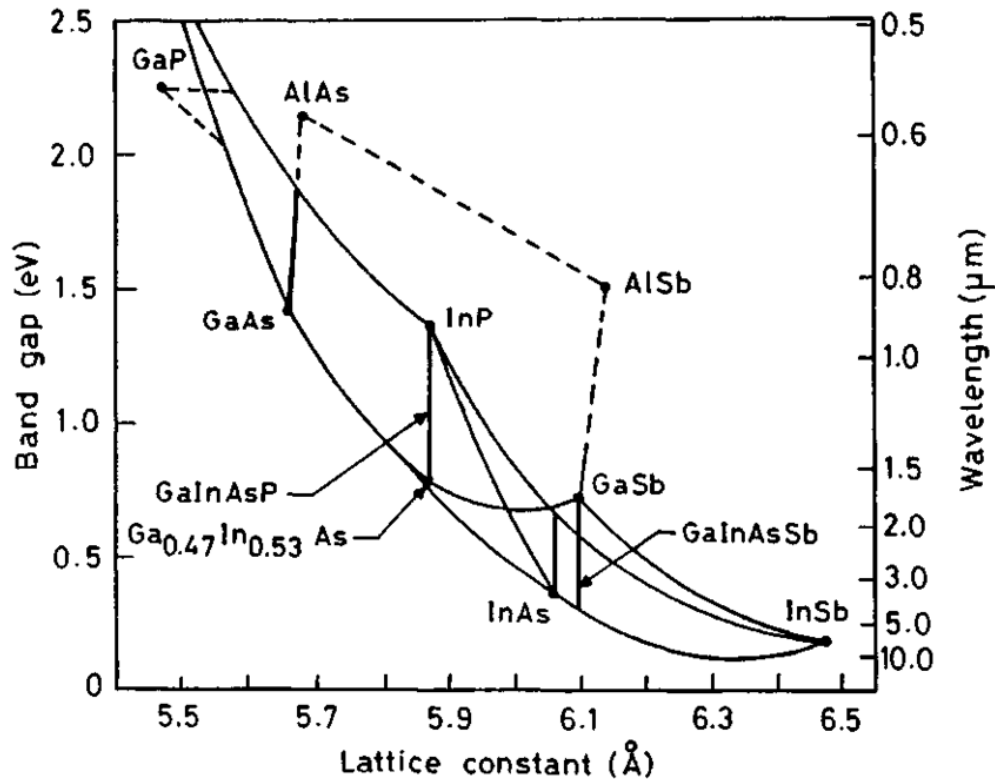


Figure 7: Bandgap as a function of lattice constant for III-V compounds and their ternary and quaternary alloys. Reproduced from [28].

The preparation of device-quality semiconductor epitaxial layers requires that the lattice constants of the growth layers and their substrates be closely matched [30]. If the lattice constants between materials are different enough, the mismatching positions of the atoms in the crystal at the boundaries cause strain [29]. This strain can cause cracking and high defect

densities that propagate through the lattice [29]. Lattice matching is critical for effective operation of laser devices because mismatch between layers results in defects that reduce efficiency and can shorten device lifetime [30]. Alloys can be lattice-matched by changing contents of some materials. In Figure 7, GaInAs is lattice-matched to InP when the Ga/In atomic fraction is 0.47/0.53. Many optoelectronic devices, such as blue LEDs and lasers, rely on sapphire as the substrate for growth, as seen in Figure 6. However, one of the limitations in the development of high efficiency blue LEDs is the high dislocation densities that are present due to the use of a sapphire substrate [20].

Dislocations act as non-radiative recombination sites, which strongly deteriorate the performance of devices by reducing minority carrier lifetime [31]. The growth conditions in the fabrication process are of critical importance when growing high-quality materials with minimal cracks and dislocations. Several techniques, such as two-step growth, strained layer superlattice, post-annealing, epitaxial lateral overgrowth, and graded buffers, have been investigated to reduce the defect density of materials, especially in the case of lattice mismatch [31]. Methods such as MOCVD and MBE allow for high-quality crystalline growth and thus minimize defects that hinder device performance. The MOCVD technology has become the dominant epitaxial growth method for III-V compound semiconductors in both research and production [32].

The developments and improvements over the past 20 years have allowed the growth of high-quality materials and many III-V devices to be commercially viable [32]. In MOCVD, metal-organic species, which are a combination of group-III atoms and alkyls, diffuse and adsorb on the substrate surface [5]. MOCVD relies on the gas-phase transfer of the materials to be deposited on the substrate by chemical reaction, typically at or near atmospheric

pressure, resulting in high-quality epitaxial thin-film deposition [33]. Because the MOCVD uses heated gas flow and surface chemical reaction, substrate temperatures are in the range of 500-1500 °C, typically higher than MBE [33]. In addition, the sample can be rotated at speeds as high as 1500 rpm, allowing enhanced growth uniformity and film quality [33]. MOCVD is now the dominant technology for the production of LEDs, solar cells, photodetectors, injection lasers, heterojunction bipolar transistors and a variety of other solid-state devices [32]. Figure 8 shows the schematic of the MOCVD sold by k-Space Associates, Inc.

MBE is a growth process for growing thin epitaxial films for a variety of materials, ranging from oxides to semiconductors to metals [34]. It is mostly used for the growth of compound semiconductors due to the high technological value of such materials to the electronics industry [34]. The MBE uses localized beams of atoms or molecules in an ultra-high vacuum environment to provide a source of the constituents to the growing surface of a substrate [34]. Figure 9 shows the top view of a simple MBE chamber showing the essential growth courses, shutters, beam flux detector and the RHEED system for monitoring structure during growth [34]. In contrast to the MOCVD, the growth of crystals using MBE is by physical deposition and not by chemical reaction. In the UHV environment, the beam atoms and molecules travel in nearly collision-free paths until arriving at either the substrate or at the walls of the chamber where they condense and are removed from the system; this minimizes contamination of the growing surface [34]. This allows the growth of high-quality films, and more importantly, the ability to change the composition of the arriving atom stream very abruptly [34]. Even though MBE produces high-quality epitaxial films, it has a lower throughput compared to the MOCVD. The MOCVD is more suitable for mass production as it is faster and cheaper [34].

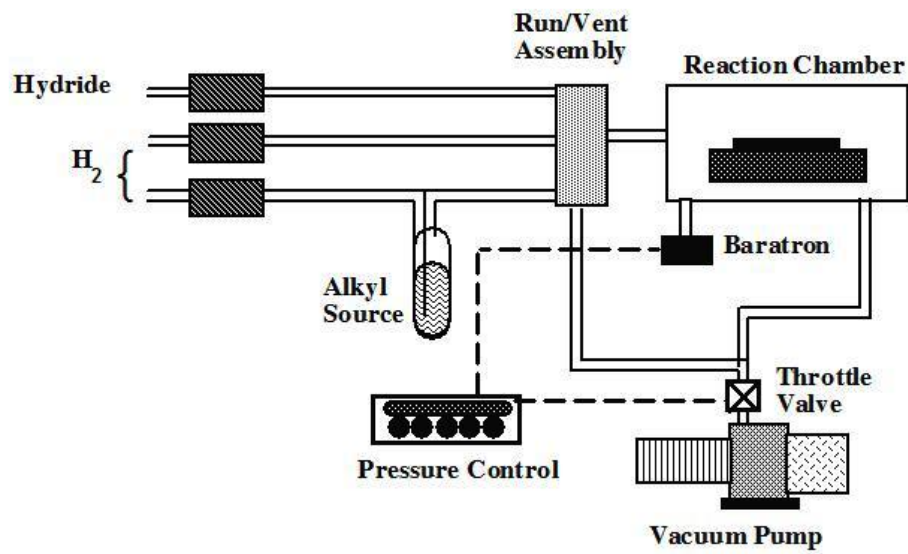


Figure 8: MOCVD system schematic. Reproduced from [33].

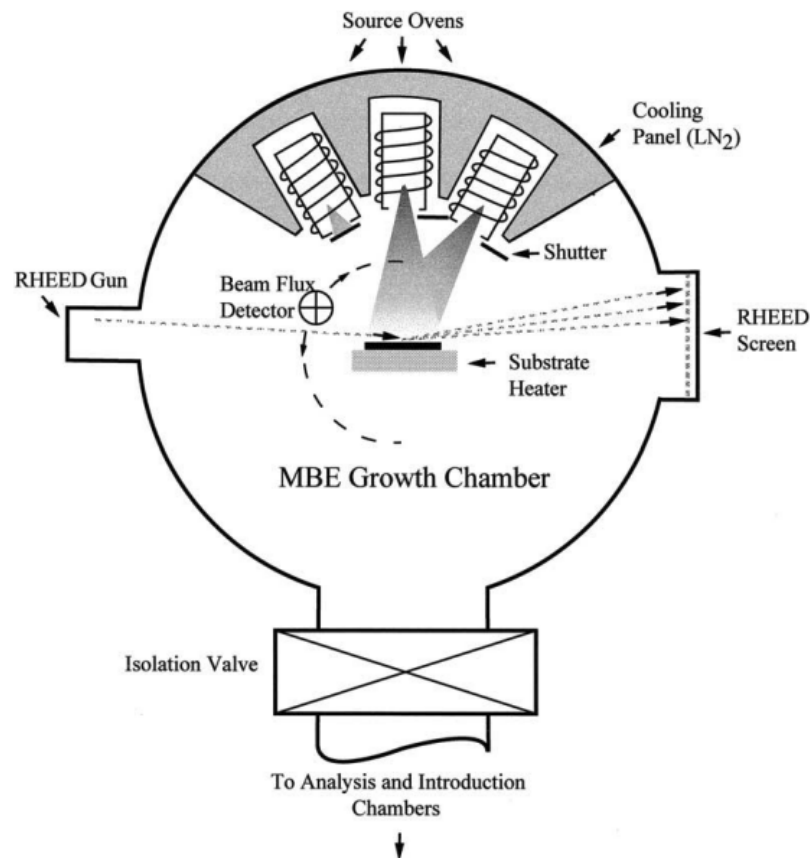


Figure 9: Top view of a simple MBE chamber. Reproduced from [34].

2.3.1 Selective Area Growth

SAG is a technique that is developed for cost savings in semiconductor manufacturing, allowing for local variation of epitaxial growth formation on the surface of a substrate [7]. With this technology, semiconductors with different bandgaps can be grown simultaneously in a single epitaxial growth, leading to well controlled simplified processing, rather than etch-regrowth-based methods [7]. SAG occurs when growth is done on a patterned substrate; the pattern is formed by having silica regions on the sample, blocking growth. SAG can be simply defined as when the epitaxial layer is confined to the window region and no deposition of the material occurs on the masked regions [35].

In selective area MOCVD growth, group-III precursors are incident on the surface, and are re-distributed in the lateral direction around the masks, leading to in-plane modulation of thickness [7]. When more than two group-III elements are involved, enhancement of growth rate around a mask is different among group-III vapour-phase precursors, leading to modulation of group-III atomic content as well as thickness [7]. Compared to bulk layers, the PL from MQWs has larger modulation due to their quantum confinement effects. A mask width should be more than 100 μm in order to obtain substantial modulation of the wavelength [7].

There are two diffusion mechanisms governing the local growth rate in a patterned growth: surface diffusion (migration in Figure 10) and vapour-phase diffusion. Surface diffusion is effectively only within several μm from the mask edge and has a small effect on modulation while vapour-phase diffusion exhibits its effect with an order of 100 μm from the mask edge and thus has a large effect on modulation [7]. The vapour phase diffusion occurs when metal-

organic group-III precursors such as trimethylindium (TMIn), trimethylgallium (TMGa), and triethylgallium (TEGa) are supplied [5]. Growth rate enhancement d/d_0 increases either with an increased mask width W_m or with decreasing mask opening W_o , where d is the thickness of the selectively grown layer and d_0 is the thickness of the reference layer [5]. Selective MOCVD growth is a very complicated technique and is not fully understood, however the diffusion of group-III species is recognized to be the driving force of growth enhancement. In the exposed region, adsorbed species are incorporated into the surface atoms in a relatively short period of time and the concentration of species on the surface is very low [5]. In the masked region, the concentration of species is not zero, however most adsorbed species will evaporate or migrate [5]. This difference in the species' concentration on the two surfaces results in a lateral concentration gradient in the gas phase [5]. Therefore, the lateral diffusion of group-III species occurs from the masked region to the growth region [5].

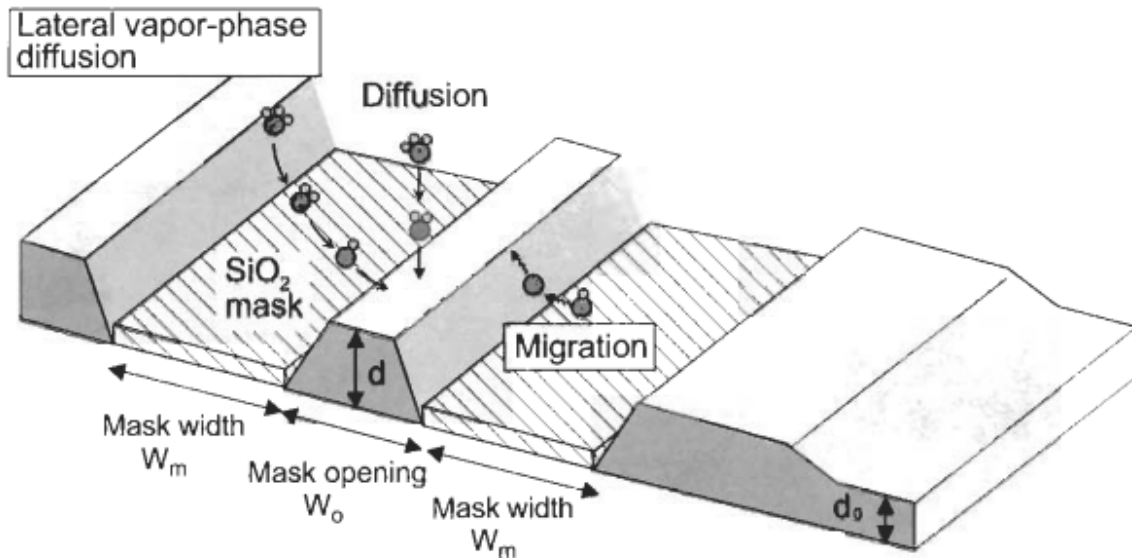


Figure 10: Selective MOCVD process. Reproduced from [5].

Studies have shown that selective area MOCVD growth results in alloy composition shift of the grown layer by changing the mask pattern. A change in atomic content will change the bandgap of the compound, ultimately resulting in a wavelength shift during measured PL. For example, in the case of InGaAsP layers, the In content will increase with an increase in mask width [5]. The group-III atomic content shift can be explained by the difference in surface migration rates or by the accelerated gas phase diffusion and incorporation of In-containing species as opposed to Ga-containing species [5]. In MOCVD, the V/III ratio is large and hence the transportation rates of As and P atoms to selectively grown layers seem comparable [5]. Therefore, compared to the shift in group-III compounds, the shift in the group-V atomic content is rather small and is in fact almost never observed [5]. It is also important that the In content enhancement is dependent on the Ga source. In content enhancements in InGaAs and InGaP layers grown by TMGa as a Ga source were greater than using TEGa, due to the difference in decomposition temperature of the metal organic species [36]. The decomposition temperature of TMGa is greater than TEGa, with TMIIn having the lowest temperature of the three species [5]. Note that the decomposed group-III species appeared to have higher diffusion coefficients, which can account for their enhanced incorporation [37]. It is also important to note that the atomic modulation is dependent on the spatial compositional shift. This shift produces a bandgap variation around the mask, especially in the case of MQWs where the electronic transitions are strongly dependent on the well thickness [8]. Sugiyama et al. found that PL shift in wavelength from the bulk layers is the result of more In-rich atomic content in InGaAsP for wider masks [7]. They also found that PL from MQWs exhibits more red shift according to the wider masks, which, as well as the compositional change described above, reflects reduced quantum confinement

effect due to increased thickness of the well [7].

Caneau et al. also investigated the growth rate enhancement for the binary compounds GaAs, InAs, GaP, and InP, and for InGaAs and InGaP lattice-matched to InP and GaAs, respectively. The growth rate enhancements for the binaries are $R(\text{InAs}) > R(\text{InP}) > R(\text{GaAs}) > R(\text{GaP})$ [38]. This is because of the order of the decomposition rates of TMIIn and TMGa in the presence of AsH_3 and PH_3 , respectively [38]. The decomposition rate of AsH_3 is higher and thus enhances the growth rate of TMIIn [38].

The thickness and composition modulation of a layer is determined by a single parameter D/k_s , which is the vapour-phase mass diffusivity / surface incorporation rate coefficient and is proportional to the concentration adjacent to the surface [7]. D/k_s is regarded as an effective lateral diffusion length of a group-III precursor in the vapour phase and has a unit of length [7]. D is inversely proportional to the reactor pressure and is strongly affected by the kind of carrier gas (D with H_2 carrier gas is much larger than with N_2) [7]. Therefore D/k_s depends on the growth conditions. The value of D/k_s can be extracted experimentally as it varies based on specific material and growth conditions [7]. For example, InAs has larger k_s (sticking coefficient) than GaAs, meaning that In “sticks” on the surface more readily than Ga on an As surface, under the same growth conditions [7]. It is important to note that nothing grows on the silica mask because SiO_2 has a very low sticking coefficient when placed within the MOCVD chamber with respect to the materials deployed [9].

Figure 11 shows the schematic of the growth pattern in SAG. W_m and L are the dimensions of the silica mask regions, and W_o is the mask opening where growth will occur. Dupuis et al. presented a vapour phase diffusion model for AlGaInAs alloys to model the selective area growth regime [8]. The approach was to ignore surface diffusion on the mask,

which means the only source of material supply is from vapour phase diffusion, and thus assuming laminar flow [8]. The Laplace equation of the concentration is given by equation (2.5) and is solved in three dimensions with boundary conditions given in Figure 12. Since surface diffusion is ignored, the mask flux is zero and therefore at $z=0$ equation (2.6) is valid. On the crystal, the Langmuir isotherm condition is assumed, thus at $z=0$ it results in equation (2.7), where D and k_s are the diffusion and sticking coefficient, respectively. Solving these equations and using fast Fourier Transform, the diffusion lengths at specific growth conditions can be extracted for the group-III elements; $D/k_s=50, 85, 10 \mu\text{m}$ for Al, Ga, In, respectively [8]. The In species has the shortest effective diffusion length which is highly enriched near the vicinity of the mask [8]. Al and Ga extend further from the mask edge due to their longer diffusion length and tend to homogenize their concentration distribution on a larger surface [8]. Therefore, their contribution to the alloy is generally less than the In precursor [8].

$$\nabla^2 N = 0 \quad (2.5)$$

$$\frac{\partial N}{\partial z} = 0 \quad (2.6)$$

$$\frac{\partial N}{\partial z} = \frac{k_s N}{D} \quad (2.7)$$

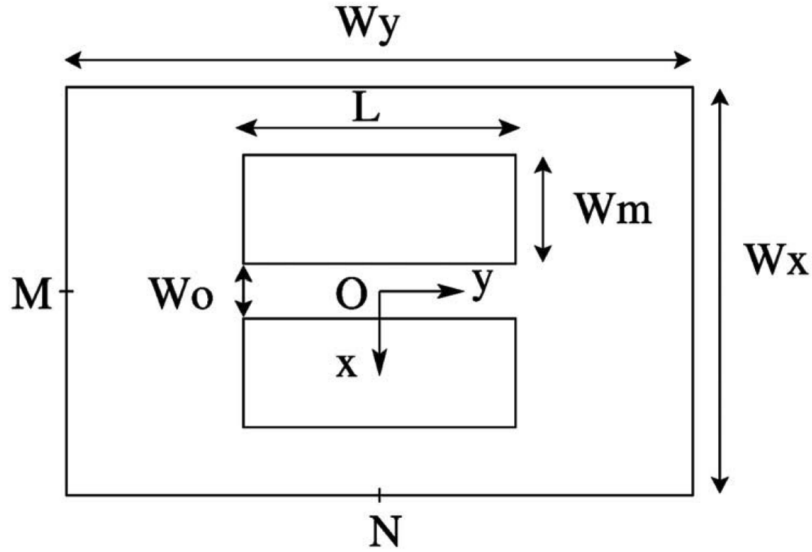


Figure 11: Schematic of the growth pattern with the dimensions W_m , W_o , L , W_x , and W_y . Three points are also marked: $O(0,0)$, $M(0,W_y/2)$, and $N(W_x/2,0)$. Reproduced from [8].

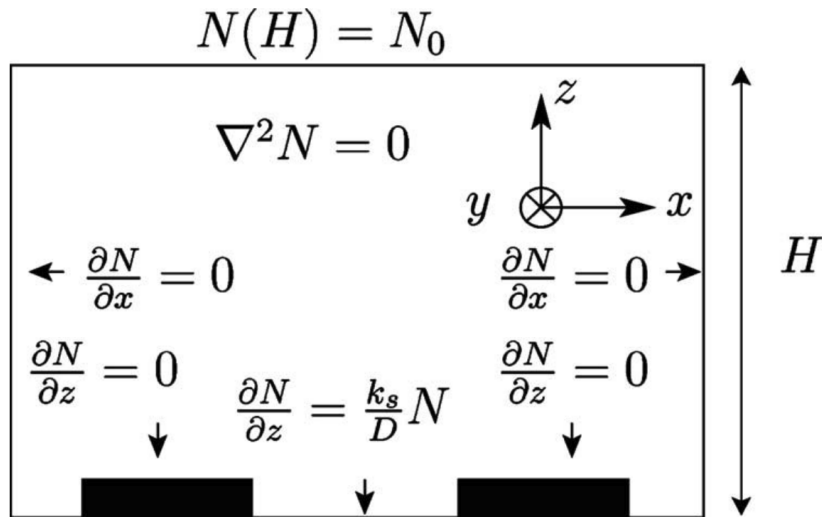


Figure 12: Schematic of the periodic window calculation with governing equations and boundary conditions. Reproduced from [8].

Bacchin et al. compared the degree of selectivity, morphology and growth mechanics of SAG performed by periodic supply molecular beam epitaxy (PSE/MBE) and conventional MBE [39]. It was found that the degree of selectivity is considerably higher in PSE/MBE than in MBE [39]. This is because selective growth is very difficult for solid source MBE under usual growth conditions [39]. Unlike the MOCVD which uses metalorganic compounds, the MBE uses elemental group-III materials making the suppression of growth on the mask more difficult [39]. There have been many attempts made to achieve selective area MBE growth with modulation however only recently was it possible when using the PSE technique [35]. An important and very interesting research area beyond the scope of this project would be to understand the difference in SAG between growth using the MOCVD vs MBE. In this work, the heterostructure has a binary active region (GaAs), and therefore a change in bandgap near the masked regions is not expected with MBE growth.

3 Experimental Methods

3.1 Semiconductor Wafer Processing

The processing of the semiconductor wafer is of great importance to successfully grow a DH laser. In this work, the semiconductor wafer used is an undoped SI-GaAs of $(100) \pm 0.1^\circ$ orientation. SI-GaAs is produced through defect engineering (via arsenic antisite defects). There are 4 major steps that must be done before this sample can be tested: chemical vapour deposition (CVD), lithography, etching, and growth. CVD is one of the most popular nanomaterials manufacturing techniques that produces high-quality thin films on large area wafers or complex patterned substrates [40].

This work uses silica as the dielectric thin film in order to achieve selective growth. The silica is grown using the silicon oxynitride chemical vapour deposition (Technics) at McMaster's CEDT facility. Silicon dioxide and oxynitride films are of great importance in the fabrication of GaAs-based devices because of their low dielectric constant, low current leakage, high breakdown voltage, and good mechanical, thermal, and chemical stability [41]. These films are used for many applications, however the most useful property for the purposes of SAG is the film's acting as a diffusion barrier.

CVD is used to deposit the amorphous dielectric layer that will block growth when placed in the MBE. This is accomplished at high temperature ($\approx 300^\circ\text{C}$) in vacuum by introducing the precursor gases. The precursor gases silane (SiH_4) and nitrous oxide (N_2O) are introduced into the chamber. This requires high vapour pressure since the precursor and the substrate must be heated to a specific temperature to allow the deposition reaction and the motion of adatoms [40]. Approximately 100 nm of silica is deposited, which is measured

using the ellipsometer.

The next step in the processing is to prepare the sample for lithography. The sample is first cleaned to remove any residue or oils with an acetone bath, followed by methanol, isopropanol, and DI water. It is then dried with nitrogen gas. The MPHP (hexamethyldisilazane) primer covers the surface of the sample via spin coating at 4000 RPM for 30 seconds; an essential step to promote adhesion of the photoresist to the substrate. The photoresist S1808 is then spin coated at the same speed and time as the primer, leaving a thickness of 800 nm of positive photoresist on the substrate. The sample is then placed on a hot plate for 90 seconds at 110 °C to solidify the film. Conventionally, photolithography is done using a photolithographic mask. The mask has a certain pattern, such that when the sample is exposed to light, some light will make it through the mask and other areas are blocked. The areas exposed to light will affect the photoresist. The photoresist either breaks down or hardens where it is exposed to light depending on the type of photoresist (positive or negative). For the positive photoresist, the exposed areas will be removed and with the negative photoresist, the exposed areas will remain.

In this work, a direct writer is used instead of the conventional photolithography method. The direct writer used is the Heidelberg μ PG 101 - Table top Micro Pattern Generator. This direct writer has advantages including better resolution as well as the flexibility to easily modify the mask and invert the pattern rather than having to switch between positive and negative photoresist. The mask is created in KLayout producing CIF (crystallographic information files) that the direct writer reads as a mask. Figure 13 shows a single group in the full pattern. This group is repeated on the sample in 45° and 90° rotations. The full pattern used on the sample is shown in Figure 14, on a scale of 2000 μ m. The pattern in

Figure 13 is designed to have a constant mask length L of $175\ \mu\text{m}$ while the mask width W_m and mask opening W_o vary. W_m varies in the vertical direction, meaning each row has the same mask width. W_o varies in the horizontal, meaning each column has the same mask opening. The mask width steps through $100\ \mu\text{m}$, $80\ \mu\text{m}$, $60\ \mu\text{m}$, $40\ \mu\text{m}$, $20\ \mu\text{m}$, and $10\ \mu\text{m}$ from top to bottom. The mask opening steps through $10\ \mu\text{m}$, $20\ \mu\text{m}$, $40\ \mu\text{m}$, $60\ \mu\text{m}$, $80\ \mu\text{m}$, and $100\ \mu\text{m}$ from left to right between the pairs. The direct writer settings are set to $11\ \text{mW}$ power and 60% duty cycle using write mode III. Once the direct writer exposure is complete, which takes about an hour for the pattern in Figure 14, the sample is prepared for etching.

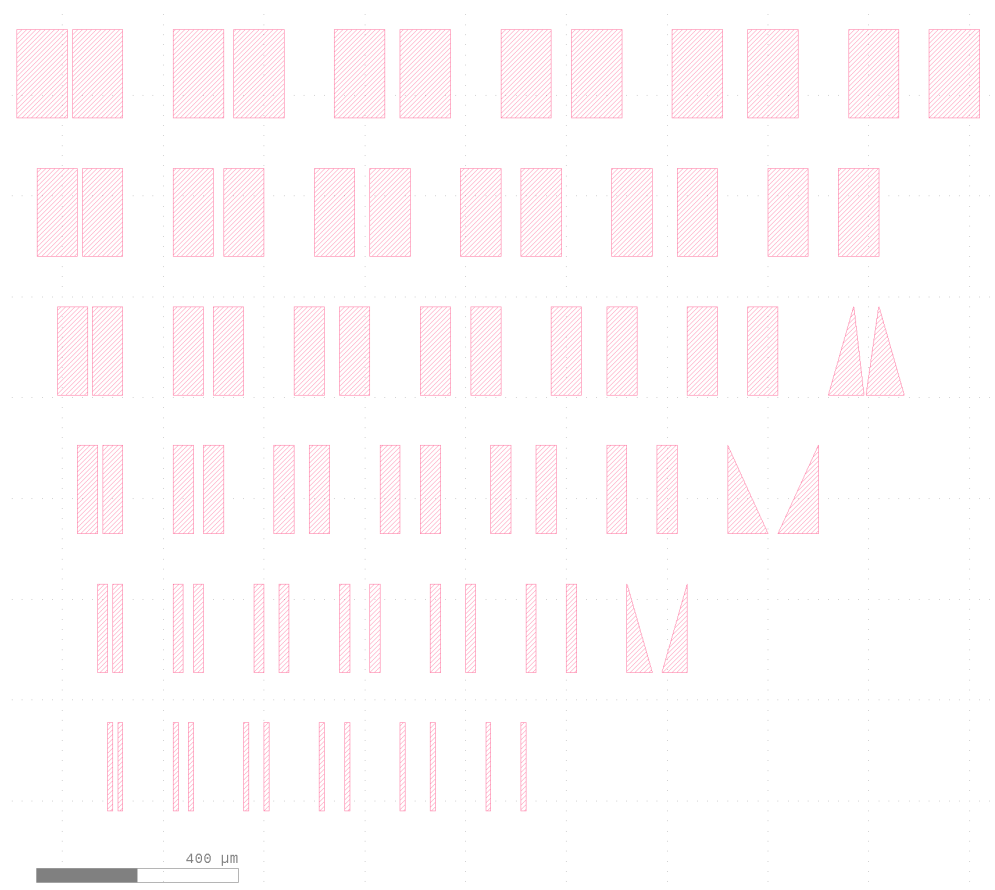


Figure 13: One group in the full pattern. $400\ \mu\text{m}$ scale.

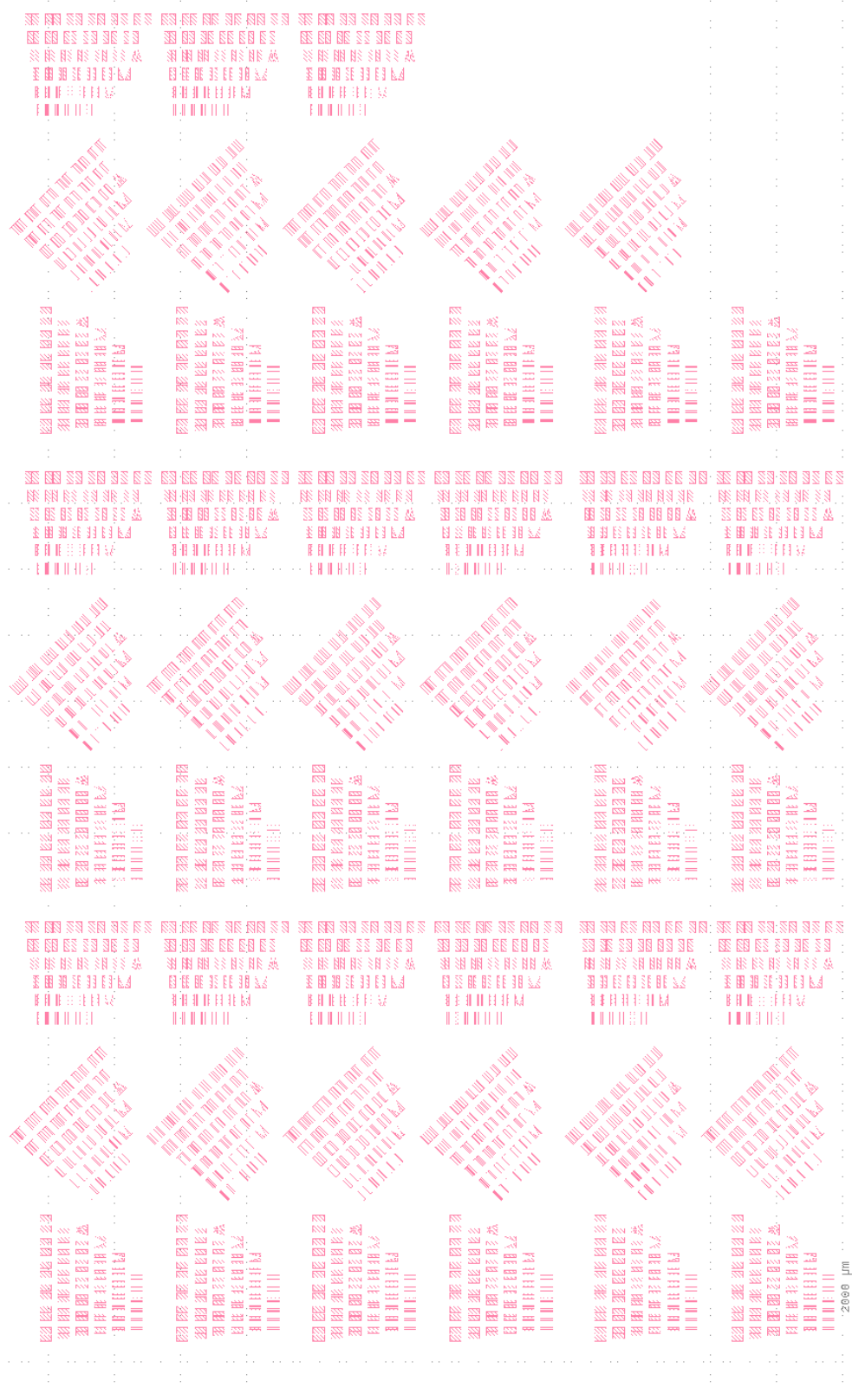


Figure 14: Full pattern on quarter wafer. 2000 μm scale.

Now that the pattern is exposed the sample is developed using the MF319 solution by manually agitating the sample in the solution. This solution removes the photoresist off the regions exposed during lithography, leaving behind photoresist only on the structures.

Figure 15 shows the sample after developing under 5x magnification.

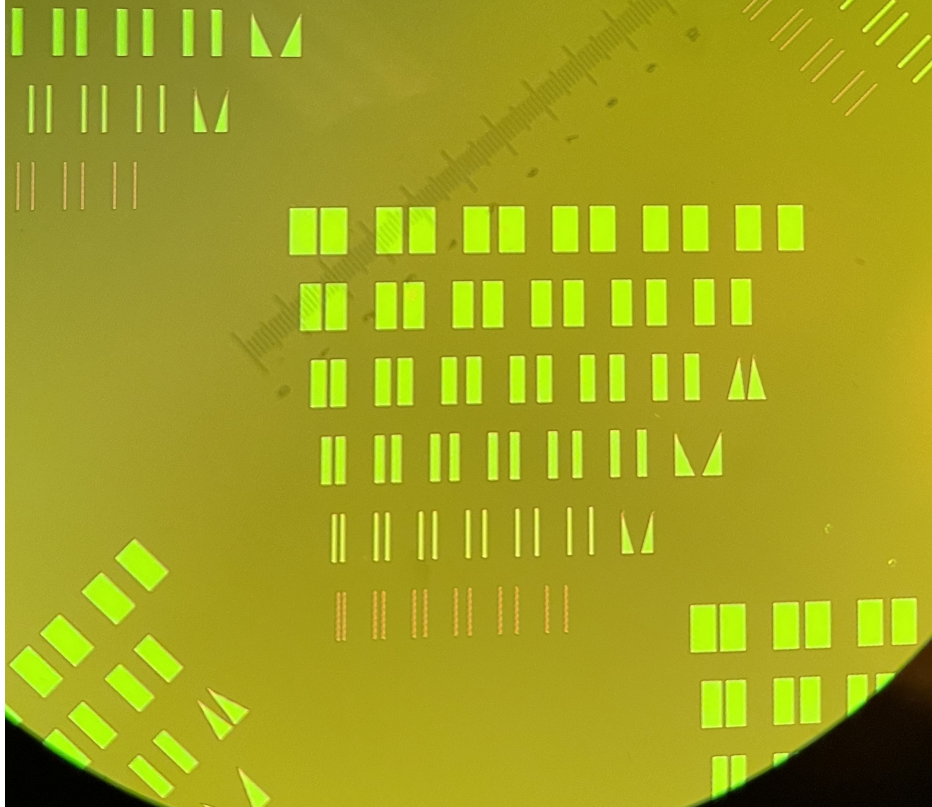


Figure 15: Sample after developing: the photoresist is removed except on the structures.

The next step is to remove the silica from the sample via etching in all the exposed regions. The silica is removed using hydrofluoric (HF) acid, specifically buffered HF 1/10. The buffered HF removes silica at 60 nm per minute. This means that approximately 100 seconds are needed to remove 100 nm of silica. The photoresist on the structures will prevent the HF solution from removing the silica under it. Once the etching is complete, the photoresist is removed with acetone, and the sample is cleaned and dried with nitrogen gas.

At this point, the sample is processed with silica structures and ready for growth. Figure 16 shows the etched sample under the microscope at 5x magnification. The yellow regions are the SI-GaAs substrate, and the darker regions are the silica structures that will act as non-growth sites when placed in the MOCVD or MBE. The fully processed SI-GaAs quarter wafer is shown in Figure 17.

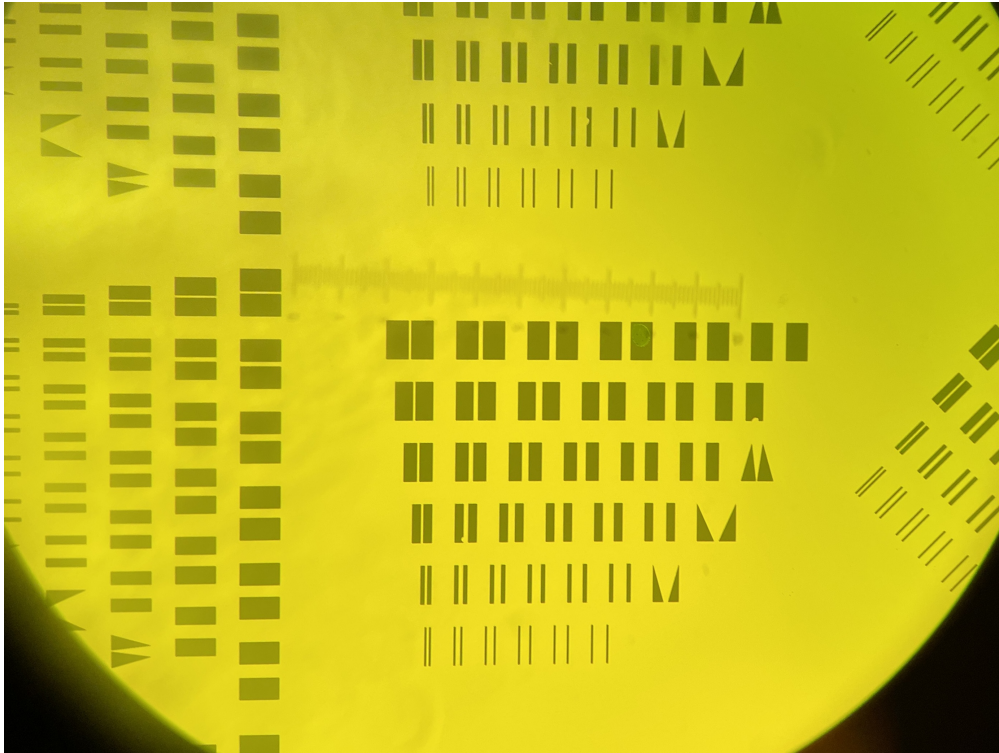


Figure 16: Sample after etching: the silica is removed except on the structures.

The final step in the process is to grow the DH on the patterned substrate. The semiconductor structure grown is 50 nm InGaP/400 nm GaAs/25 nm InGaP using the MBE (Figure 18). A structure is grown on a SI-GaAs wafer without any processing done, as calibration. This calibration wafer will be important for PL measurements where the effect of non-uniformity of the processed sample can be analyzed. InGaP and GaAs are lattice-matched and thus will prevent strain and reduce the dislocation density in the lattice, ultimately

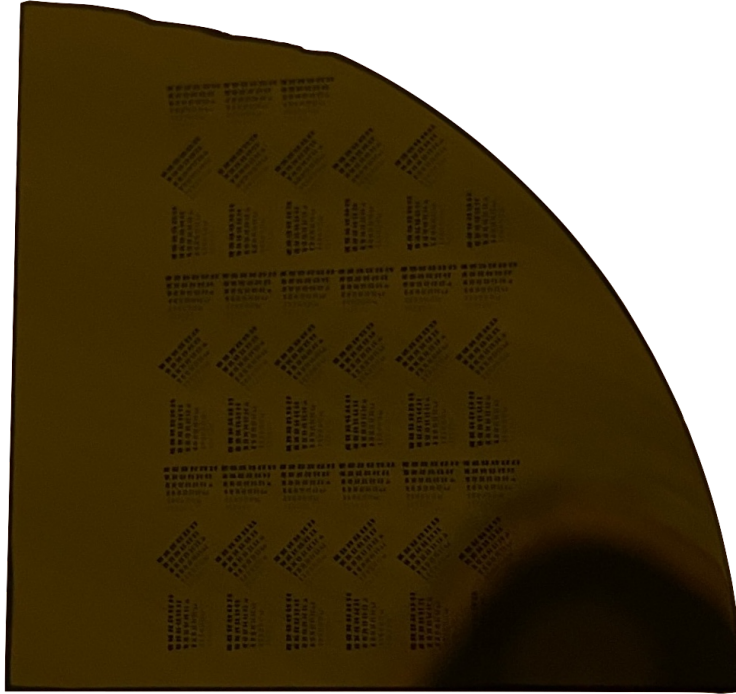


Figure 17: Processed sample before growth.

allowing stronger PL intensity [42]. In this structure, the InGaP confines the carriers to the GaAs, producing PL at approximately 875 nm, the bandgap of GaAs. Since the substrate is semi-insulating, there is no PL from the substrate. When a nominally undoped or lightly doped substrate was measured, a significant PL background in the wavelength range of interest was observed.

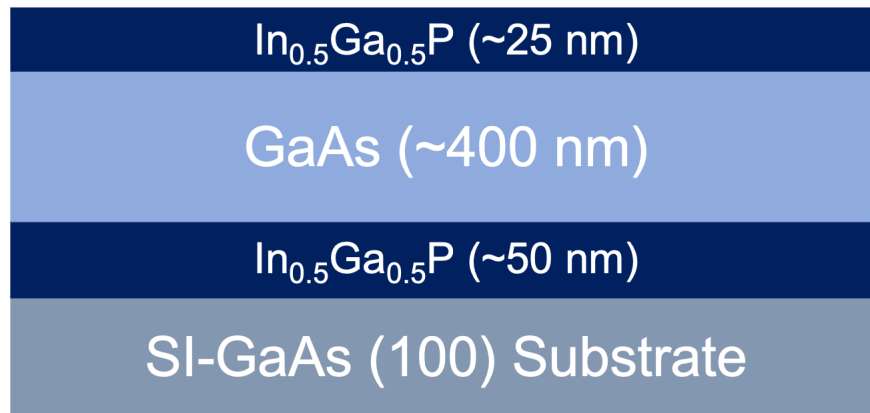


Figure 18: Semiconductor heterostructure grown using molecular beam epitaxy.

3.2 Micro-Photoluminescence Spectroscopy

The PL of the sample is measured using a room temperature μ -PL apparatus that was built as a part of this work. A schematic of the setup is shown in Figure 19. A Newport R-39635 HeNe laser system of 17 mW power, random polarization, and 633 nm emission wavelength is used as the excitation source. To excite the semiconductor, the photon energy supplied must be equal to or greater than the bandgap. In this case, GaAs has an emission wavelength of 875 nm, a lower energy than 633 nm, making the HeNe laser sufficient for excitation. The laser light reflects off three mirrors at different angles and hits the sample from above. The sample is placed on a motorized XY aperture stage (Zaber ASR series model ASR100B120B-T3-K0047), controlled by a two-axis stepper motor controller (Zaber X-MCB2 series model X-MCB2-KX14B).

After reflecting off the last mirror, the light goes through a Thorlabs DMSP650R dichroic beamsplitter. The dichroic beamsplitter is a shortpass filter with a cutoff value of 650 nm. The transmission band has an average value greater than 90% between 410-633 nm, and an average reflection band value greater than 95% between 685-1600 nm. This means that the laser light goes through the objective lens and the PL from the sample is transmitted to the monochromator input while blocking the 633 nm light reflected from the sample. The objective lens used is the 378-806-2 Mitutoyo M Plan Apo 100x Objective, with a working distance of 6 mm, focal length of 2 mm, and wavelength range of 435-655 nm. This objective lens allows a spot size in the single microns range. After the PL passes through the dichroic beamsplitter, the light is collimated using a 2 inch diameter focusing lens before reaching the monochromator input. The focusing lens's focal length is matched to the $f\#$ of the

monochromator.

The Oriel MS257 USB/RS232 (model 77781) monochromator steps through a wide range of wavelengths depending on the grating and allows a specific wavelength output. The monochromator is set to the third grating, which has a blaze wavelength of 750 nm. The slit width of the input and output are set to 1600 μm . This is wide enough to capture PL response without losing too much resolution. The signal from the monochromator output is detected using a Newport model 2031 silicon detector. The detector's responsivity (A/W) peaks between 800 nm and 1000 nm, making it suitable for GaAs PL. The silicon detector at high sensitivity has a transimpedance gain of 2×10^6 V/A and has a typical maximum responsivity of 0.6 A/W at 900 nm. The detector is connected to the Stanford Research Systems model SR830 DSP lock-in amplifier to reduce noise. This is possible by chopping the laser to a frequency of 100 Hz. The laser is modulated by a Gentec SDC-5000 digital optical chopper, making the chopper frequency the reference signal. The signal detected by the detector is combined with the reference signal and then integrated over the lock-in's measurement time constant. This results in narrower effective bandwidth and ultimately a cleaner PL signal. Finally, the oscilloscope displays the signals, and a Keysight 34461A digital multimeter is connected to the lock-in amplifier and displays the voltage reading of the PL from the sample. These instruments are integrated and controlled using the software LabVIEW. The XY stage, monochromator, and voltmeter are connected to the computer to obtain measurements. Figure 20 is a PL scan of the SI-GaAs patterned sample with lock-in settings of 1 mV sensitivity and 3 second time average. Figure 21 is of the uniform calibration sample with 2 mV sensitivity and 1 second time average. Note that the PL scans in Figures 20 and 21 are in increments of 5 nm from 750-950 nm.

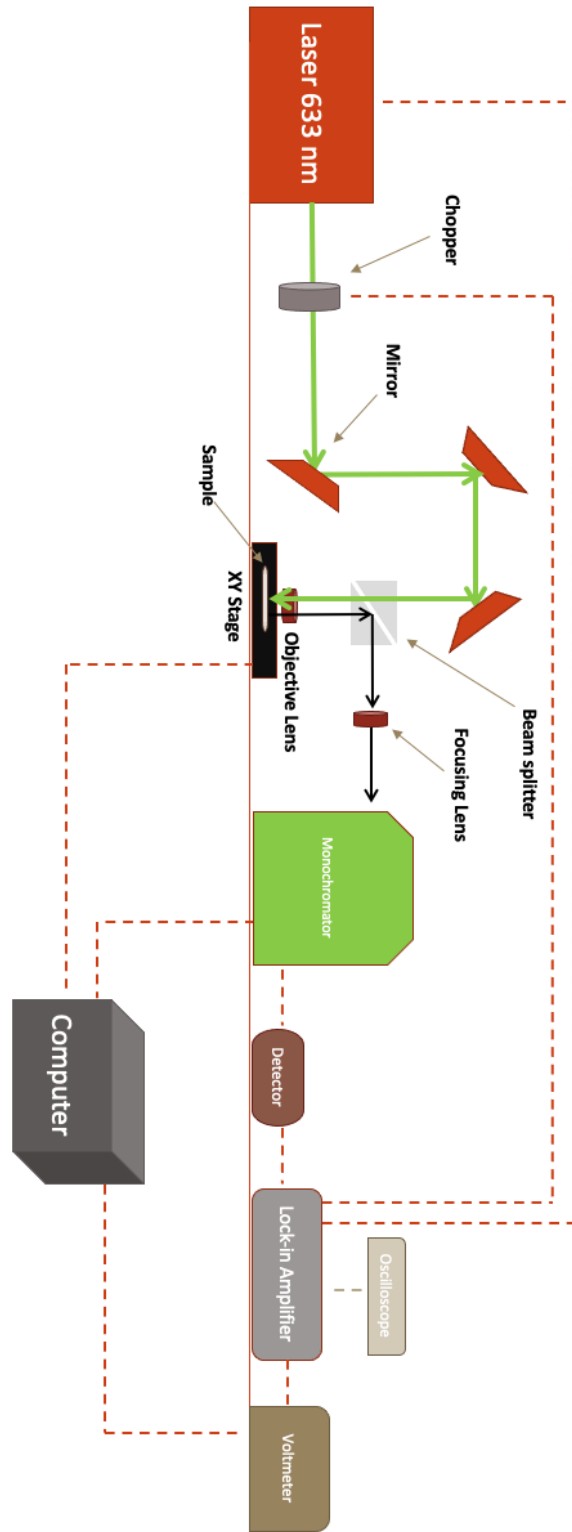


Figure 19: Micro-photoluminescence apparatus schematic.

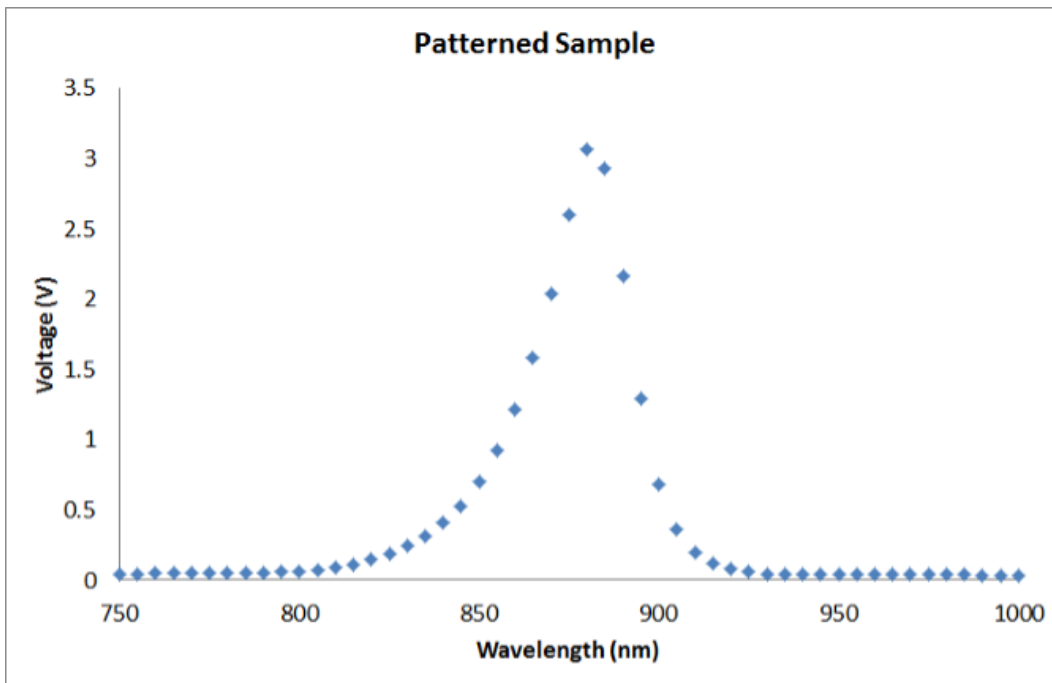


Figure 20: MBE patterned growth of InGaP/GaAs/InGaP on SI-GaAs.

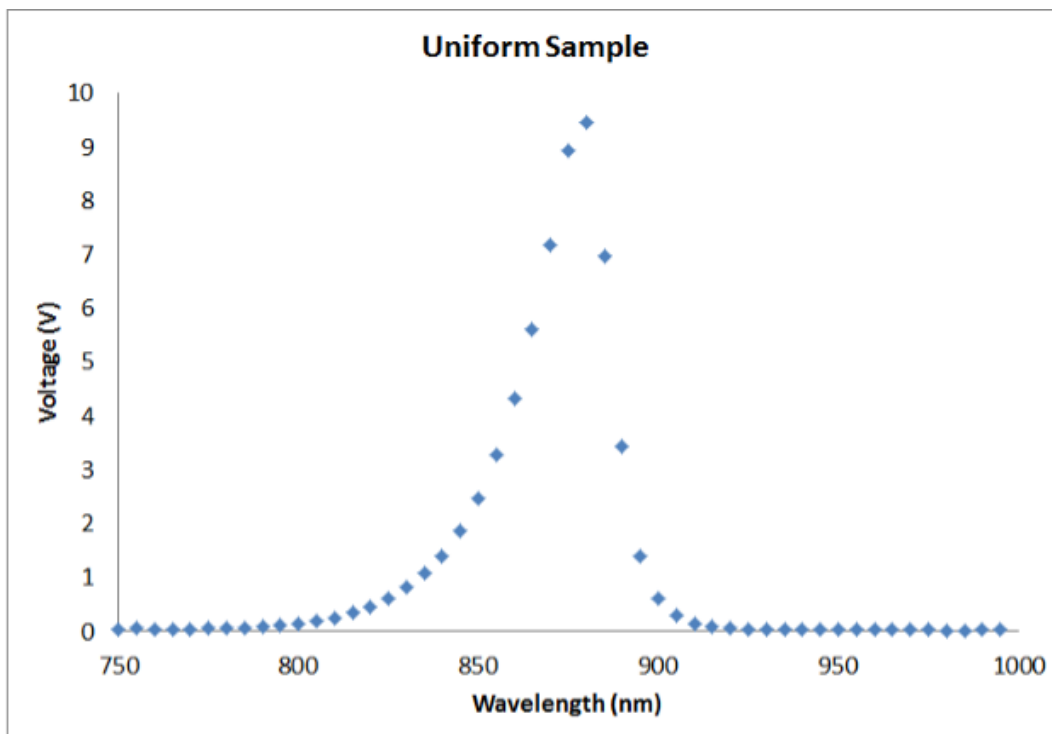


Figure 21: MBE uniform growth of InGaP/GaAs/InGaP on SI-GaAs.

It is important to note some differences between the PL of the uniform and patterned samples. Even though both samples were grown under the same conditions, the patterned sample requires more time averaging for a clean signal, otherwise the signal is too noisy. In addition, the PL intensity of the patterned sample is significantly weaker; Figures 20 and 21 suggest a decrease in PL intensity by a factor of 6. This was calculated by comparing the peak voltages at their respective sensitivities. It is important to note that Figure 20 is averaging over an unknown region that includes silica structures. These plots show clearly that the PL is suppressed but the shape of the PL curve is the same. The difference in PL intensity can be attributed to the introduction of non-uniformity via silica structures. However, this is highly dependant on the location of the sample. In Figure 13, the pink shapes are the silica structures that will act as non-growth sites when placed in the MBE or MOCVD, while all surrounding regions will experience growth. It is useful to think of these silica structures as “obstacles” in the way of growth. Usually when growth is done on a uniform surface, the resulting growth is typically more uniform. However, when adding structures in the way, whether intentional or not, the growth uniformity is affected. Even though this uniform growth is being used as an advantage to simultaneously grow different bandgap materials, one possible drawback is the PL intensity is lessened.

The HeNe laser shines light on the sample through the optical path shown in red in Figure 22. Figure 23 shows a picture of the full setup. In summary, the PL from the sample is reflected toward the monochromator input, the detector will detect the output of the monochromator at a particular wavelength, and a voltage reading is recorded at that wavelength. The computer however allows us to take step measurements, where the stage initializes the position, the monochromator scans through wavelength, and the voltmeter

records the voltage after each wavelength. Ultimately, an area on the sample can be scanned to produce PL images at a particular wavelength. This is accomplished by setting the wavelength to a constant value, typically around the peak value (880 nm), then measuring the voltage in the X and Y direction by doing a raster scan. It is also possible to collect the full spectrum at each spatial point, however since the monochromator moves slowly, it is preferred to spatially scan at a fixed wavelength and then change wavelength to obtain spectral information.

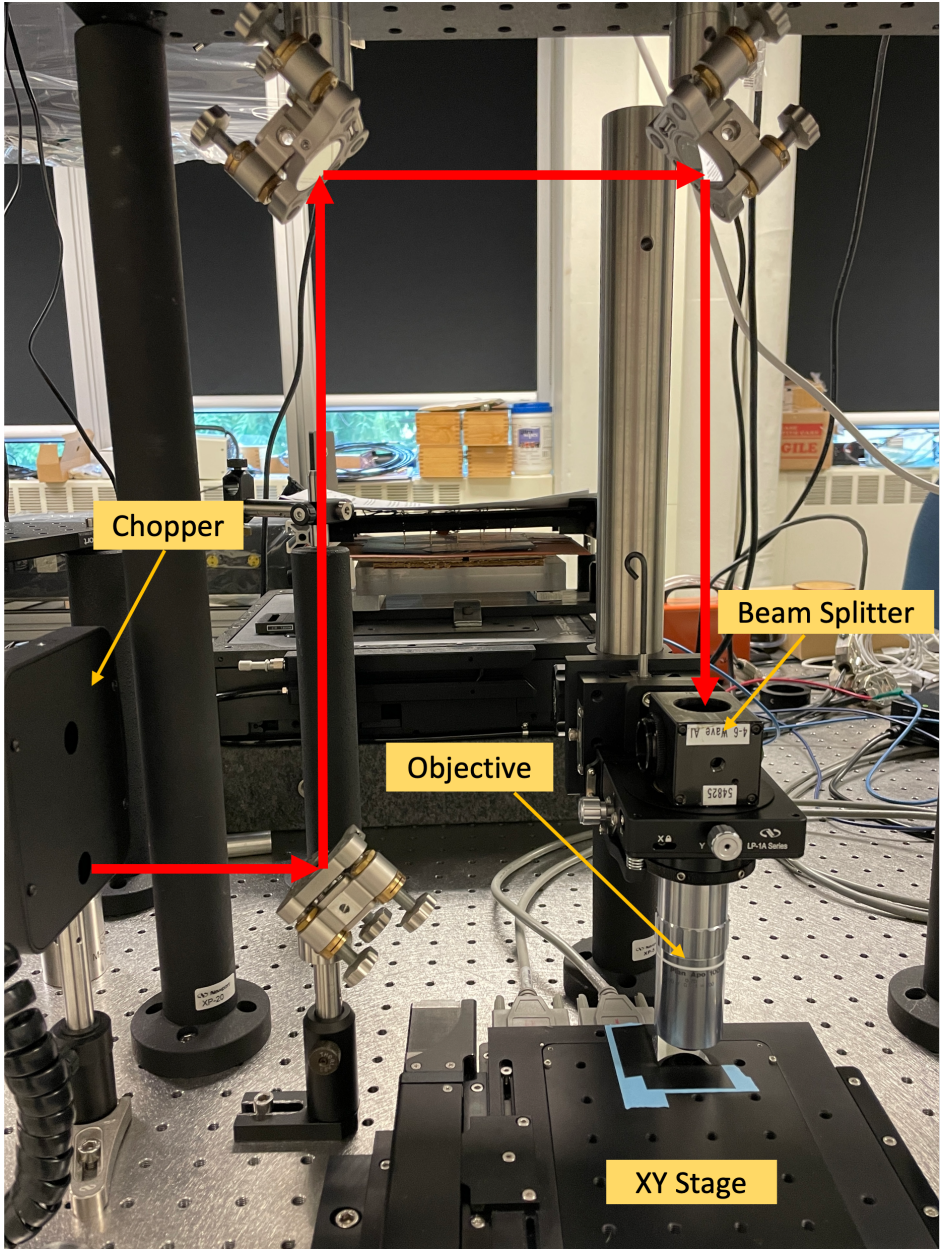


Figure 22: Optical path.

4 Results & Discussion

4.1 Photoluminescence Imaging

The conditions for the PL measurements of the SI-GaAs patterned sample are summarized in Table 1. The detector sensitivity is set to high, and the lock-in has a sensitivity of 50 mV and time constant of 1 second. The stepping in X and Y is always 100 points, making each image 10000 points. The stage has an origin, i.e. the home position of the axes. The sample is placed with the home position at the bottom right corner of Figure 17. This means that at the home position, the laser shines in the area left of the bottom left group. The X-Y Position coordinates in Table 1 refer to the position (in microsteps) on the sample relative to the origin (0,0). The sample is placed on the XY stage with default units in microsteps, where 1 μm corresponds to 6.4 microsteps. For example, “48000, 52000 - 48000, 52000” means the X axis is scanned from position 48000 to 52000, and so is the Y axis. The stage also allows independent movement of the axes. This means that the user can specify which direction should scan first in the raster scan.

Each PL image is scanned at a constant monochromator wavelength, set around the peak wavelength of 880 nm. Scans 9-11 scan the same region at different monochromator wavelengths. As seen in Figure 20, the peak wavelength value is between 870 and 890 nm. Having these three points, one below the peak wavelength, one above the peak wavelength, and another in between, will allow an approximation of the peak value by fitting to a parabola. This is very useful in cases where a wavelength shift is expected due to selective area growth. Finally, the delay is the time set in the program to wait before moving to the next point during a scan. This should match the time constant of the lock-in amplifier for

clearer images.

Scan	Order	X, Y distance (μm)	λ (nm)	Delay (ms)	X-Y Position
1	X/Y	625, 625	880	0	48000, 52000 - 48000, 52000
2	X/Y	625, 625	880	650	48000, 52000 - 48000, 52000
3	X/Y	1250, 1250	880	700	48000, 56000 - 48000, 56000
4	X/Y	625, 625	880	700	52000, 56000 - 48000, 52000
5	X/Y	313, 313	880	700	54000, 56000 - 48000, 50000
6	X/Y	1250, 1250	880	1000	48000, 56000 - 48000, 56000
7	X/Y	1719, 1953	880	1000	47000, 58000 - 44000, 56500
8	X/Y	859, 977	880	1000	52500, 58000 - 44000, 50250
9	X/Y	859, 977	880	700	52500, 58000 - 44000, 50250
10	X/Y	859, 977	870	700	52500, 58000 - 44000, 50250
11	X/Y	859, 977	890	700	52500, 58000 - 44000, 50250
12	Y/X	203, 203	870	700	56200, 57500 - 44900, 46200
13	X/Y	2500, 2500	880	700	24000, 40000 - 24000, 40000
14	Y/X	1250, 1250	880	700	20000, 28000 - 32000, 40000
15	Y/X	625, 625	880	700	20000, 24000 - 36000, 40000
16	Y/X	1250, 1250	880	700	32000, 40000 - 32000, 40000

Table 1: Summary of photoluminescence images.

Figures 24-39 show the corresponding images to Table 1.

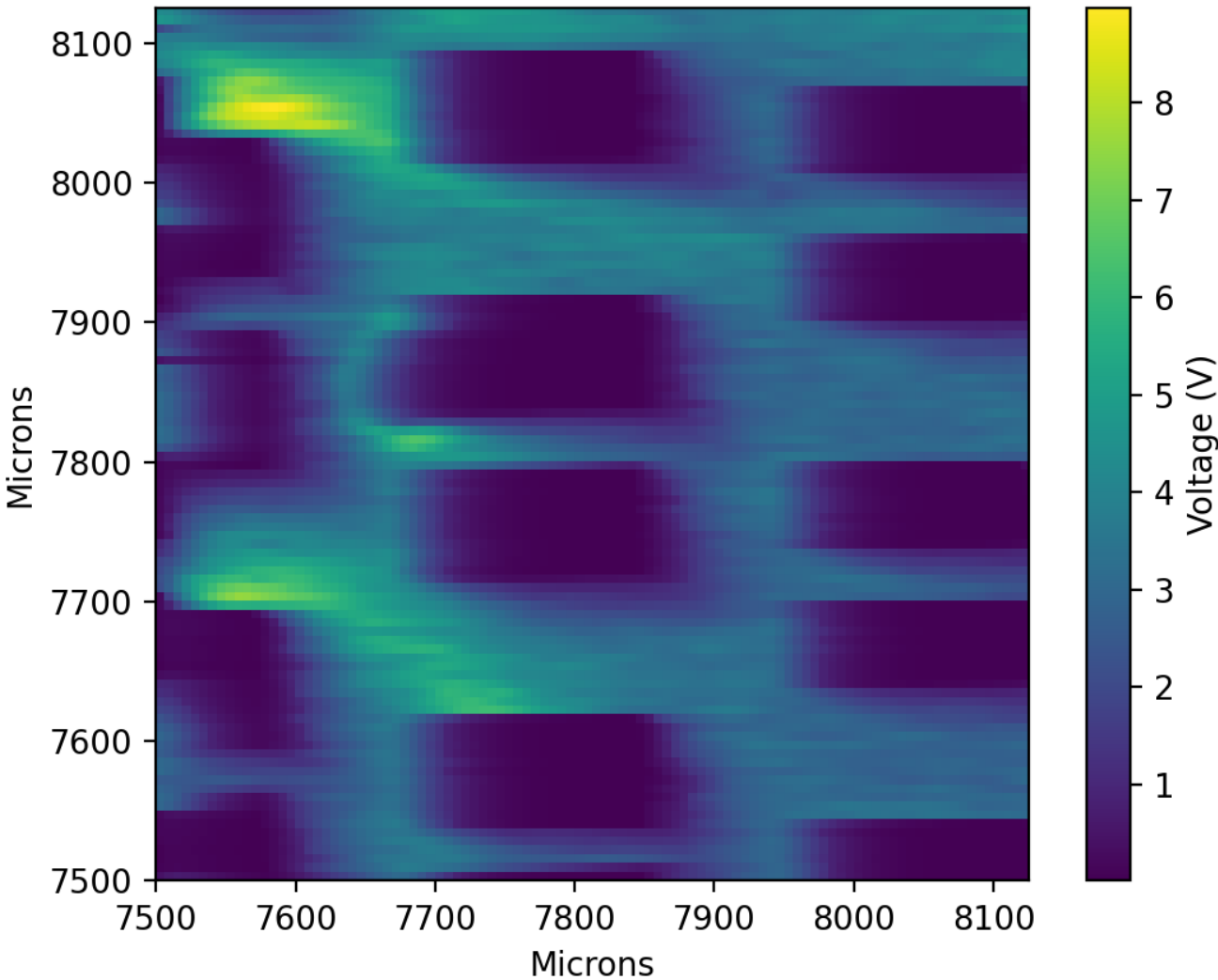


Figure 24: Scan 1.

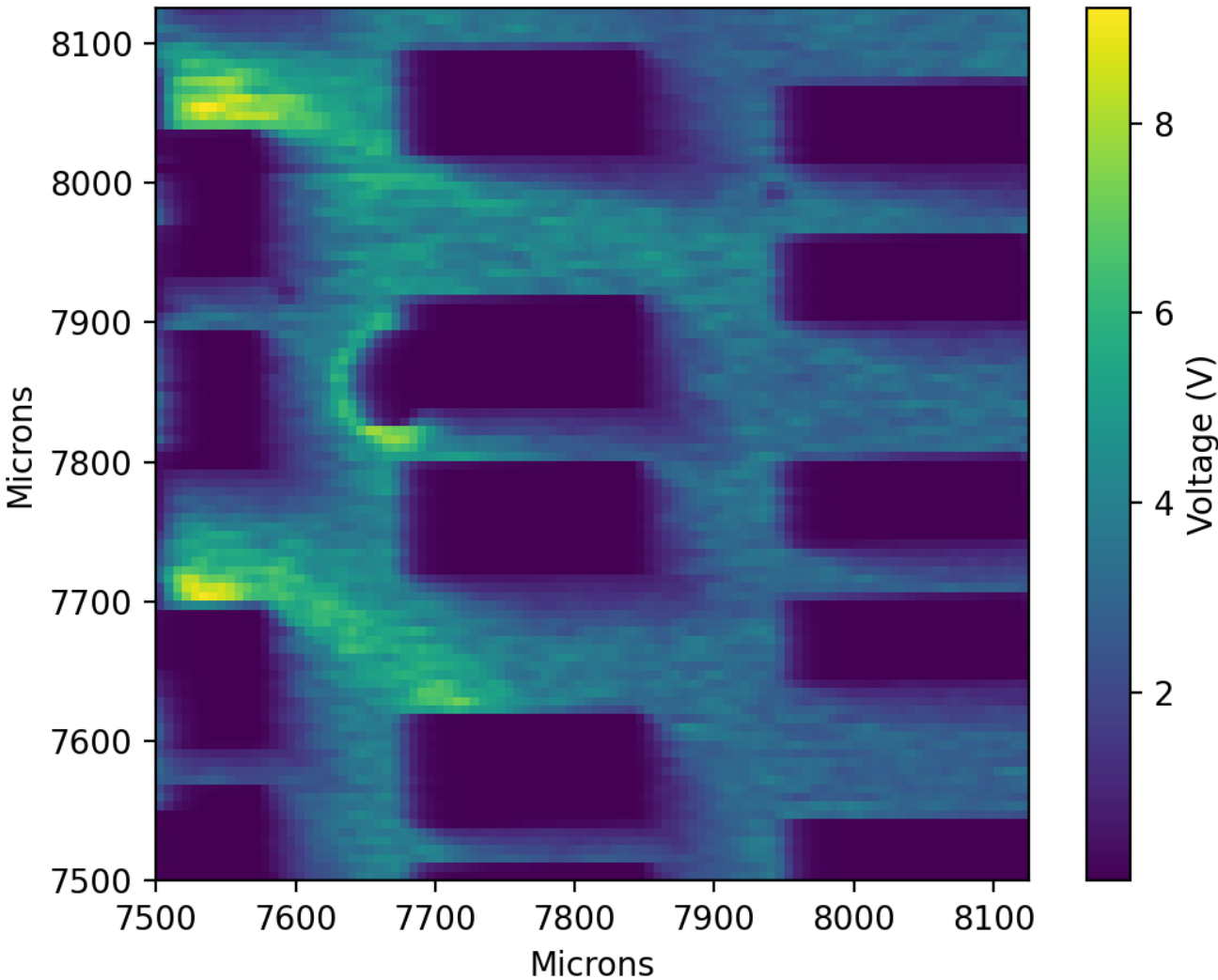


Figure 25: Scan 2.

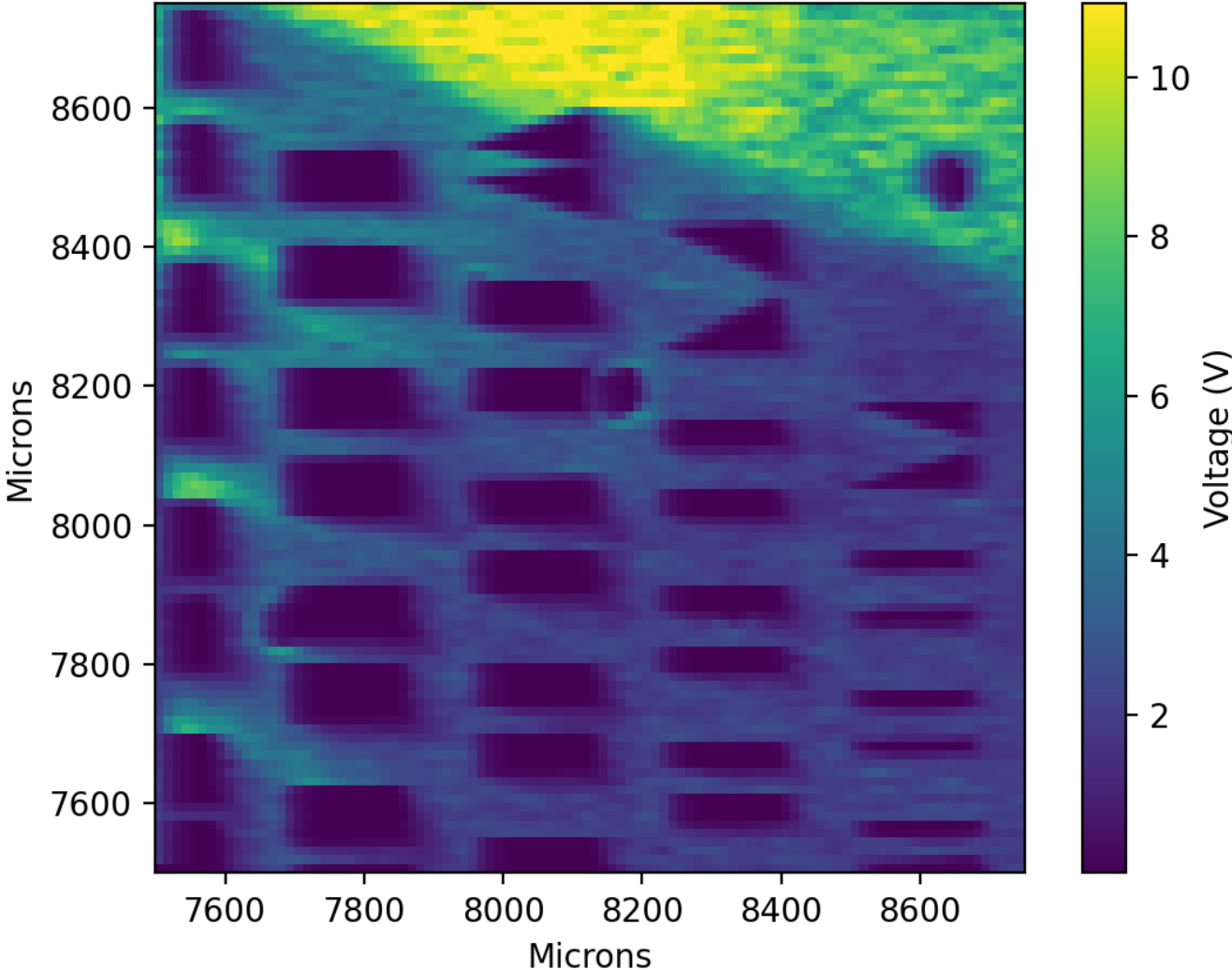


Figure 26: Scan 3.

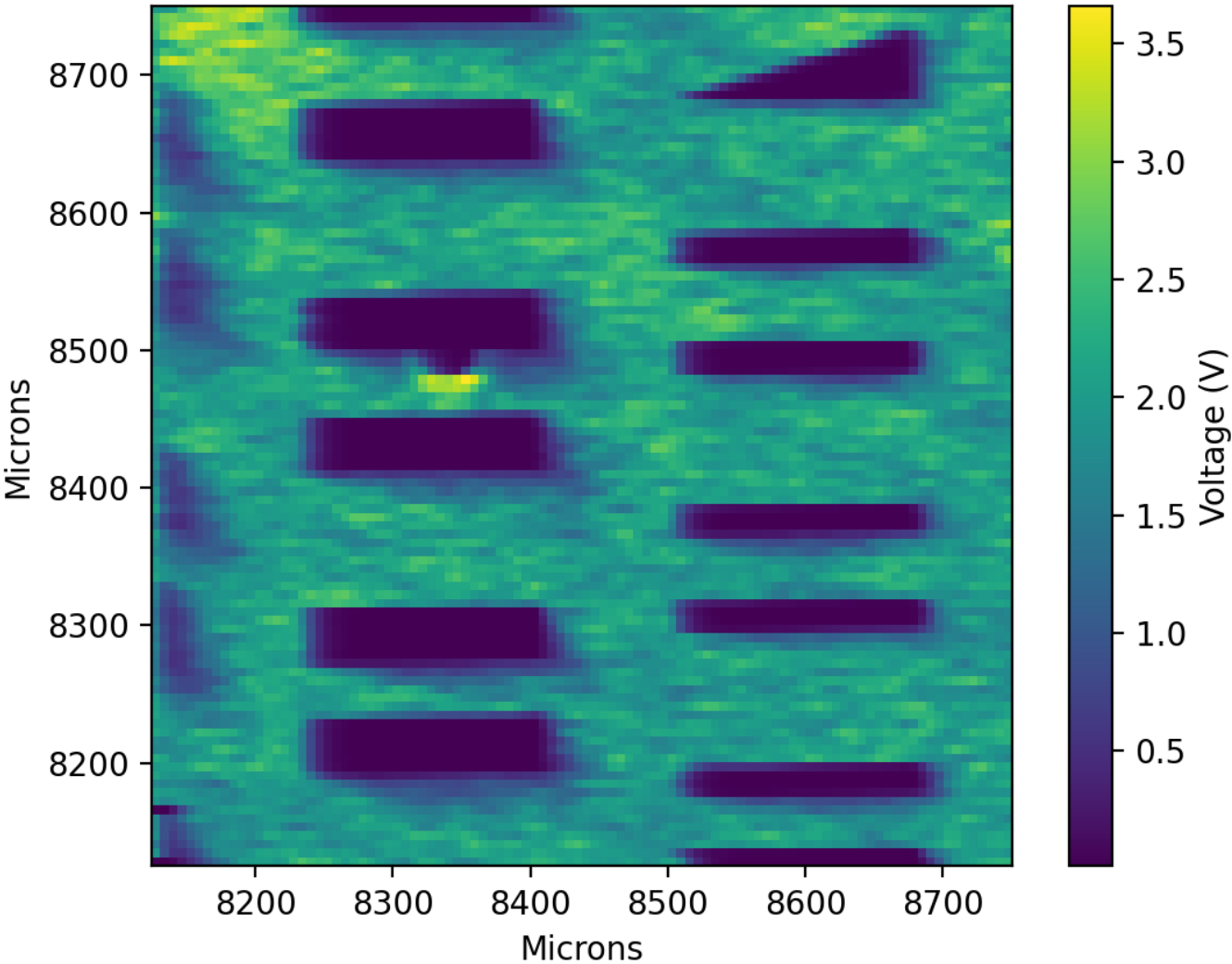


Figure 27: Scan 4.

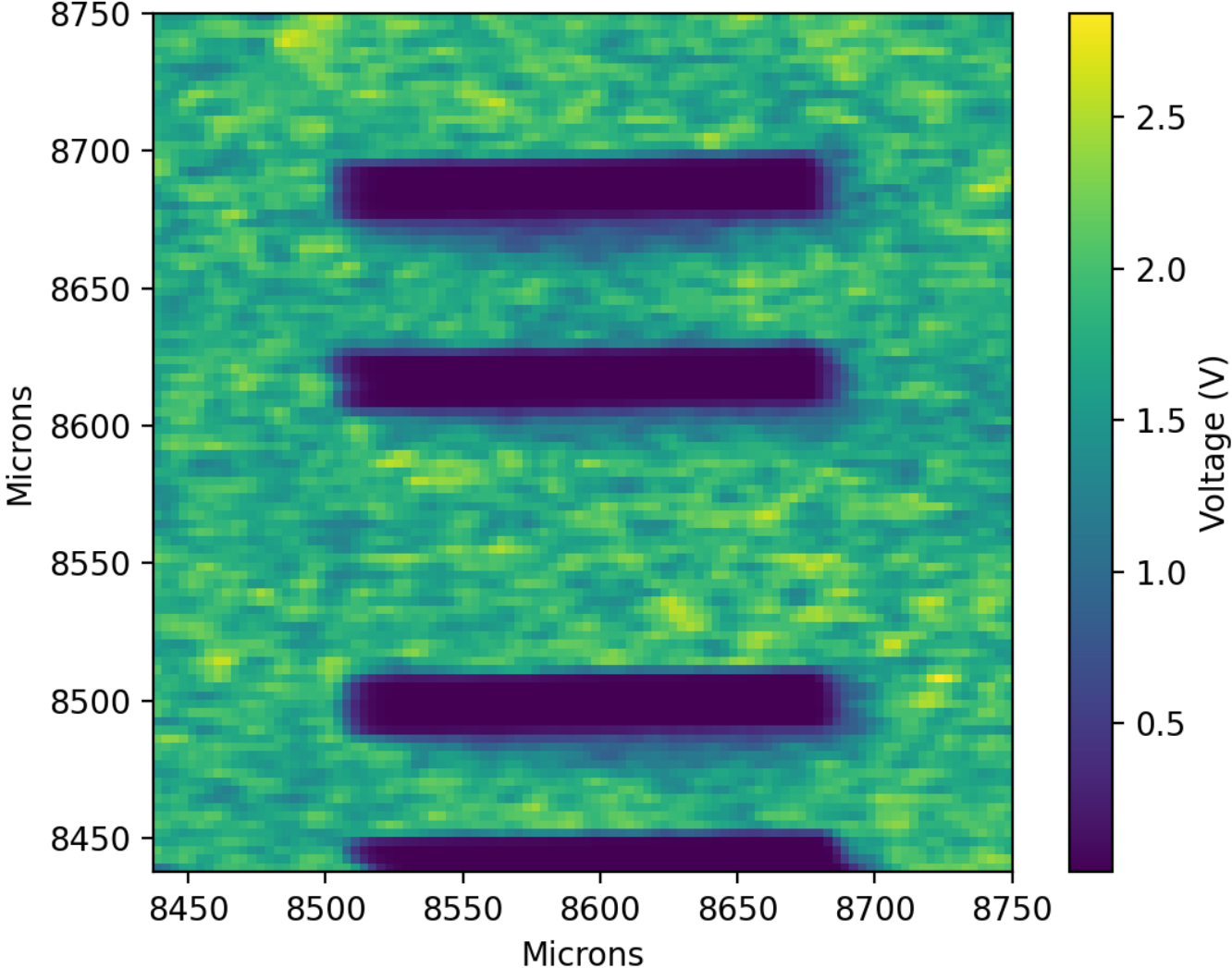


Figure 28: Scan 5.

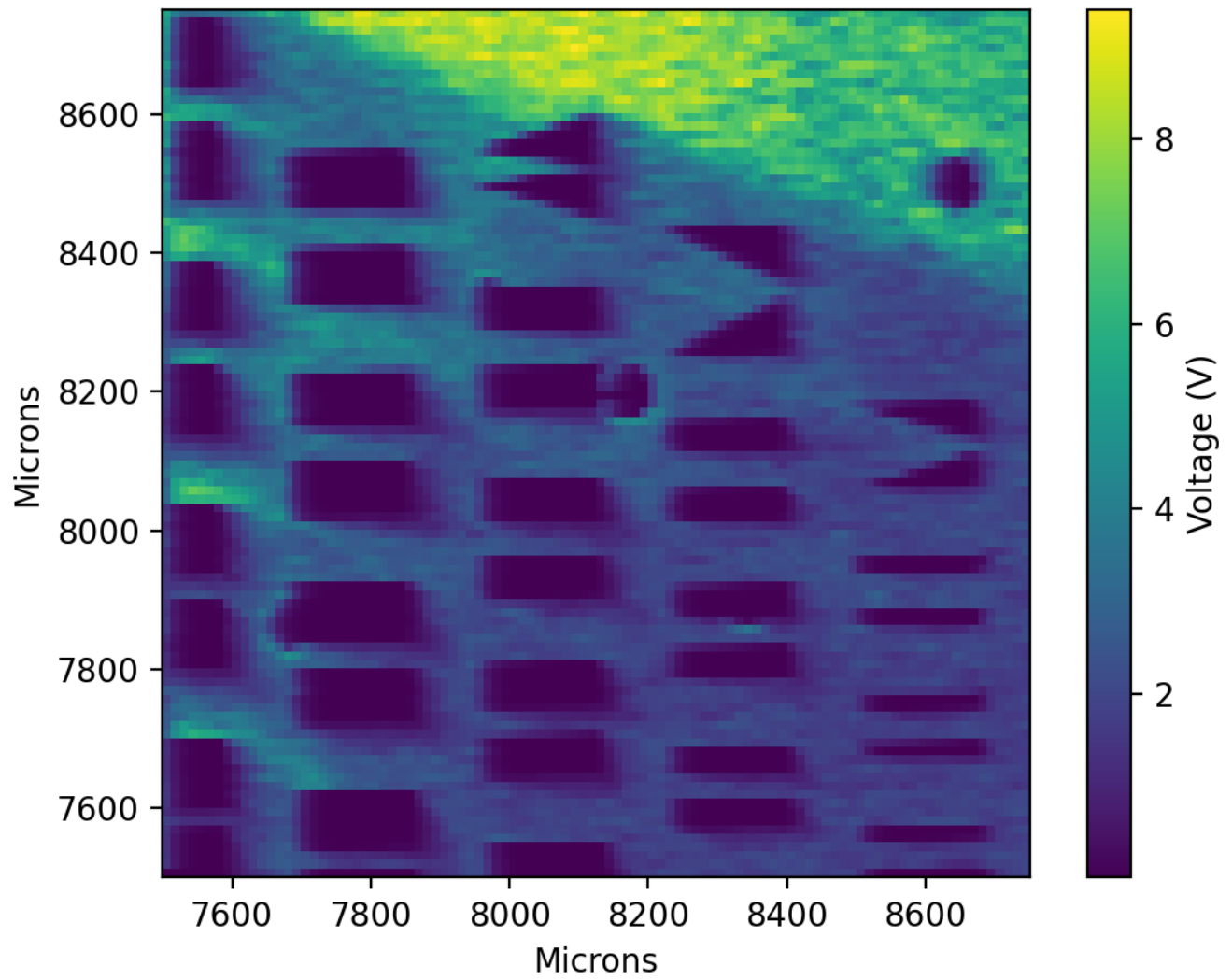


Figure 29: Scan 6.

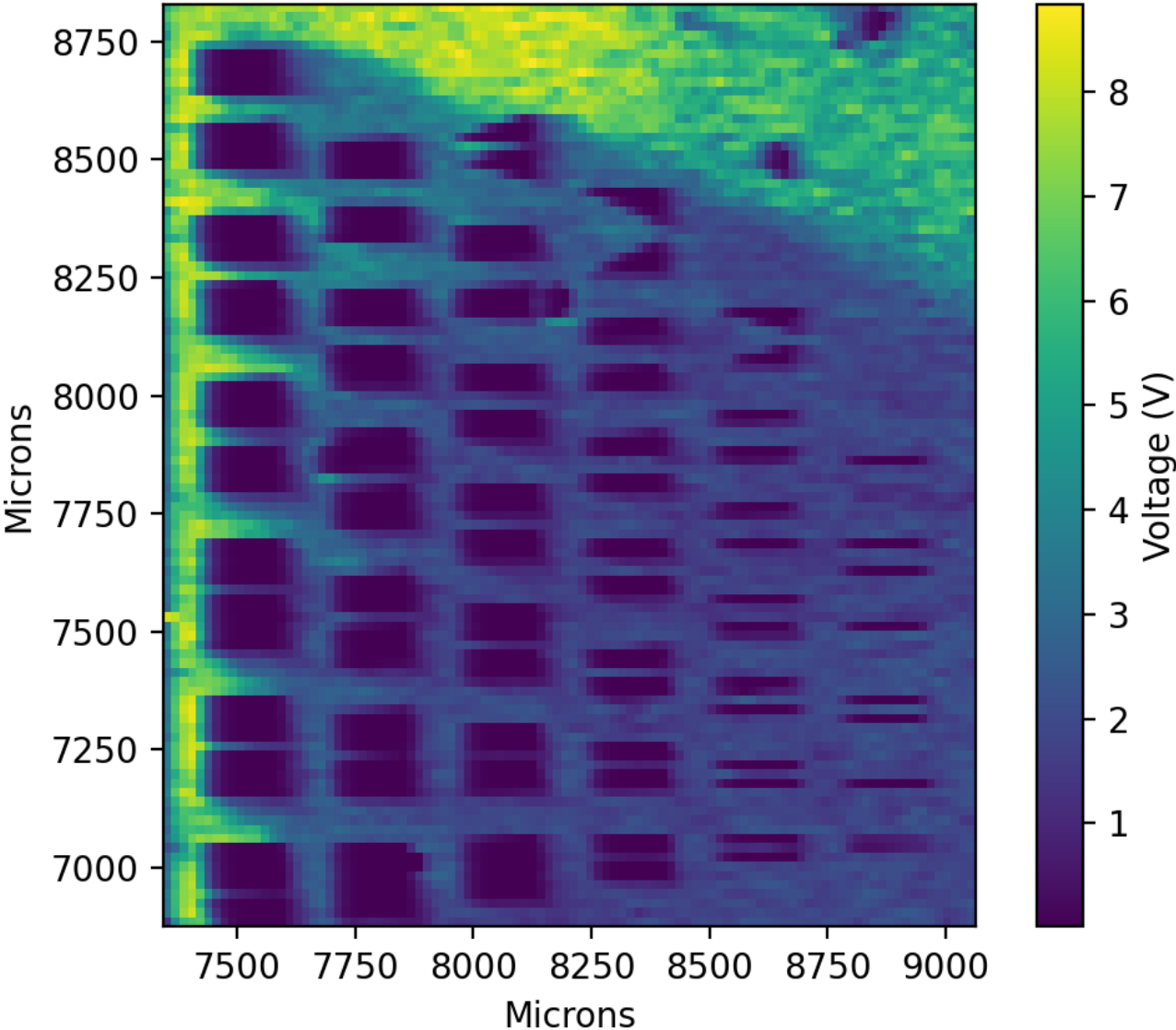


Figure 30: Scan 7.

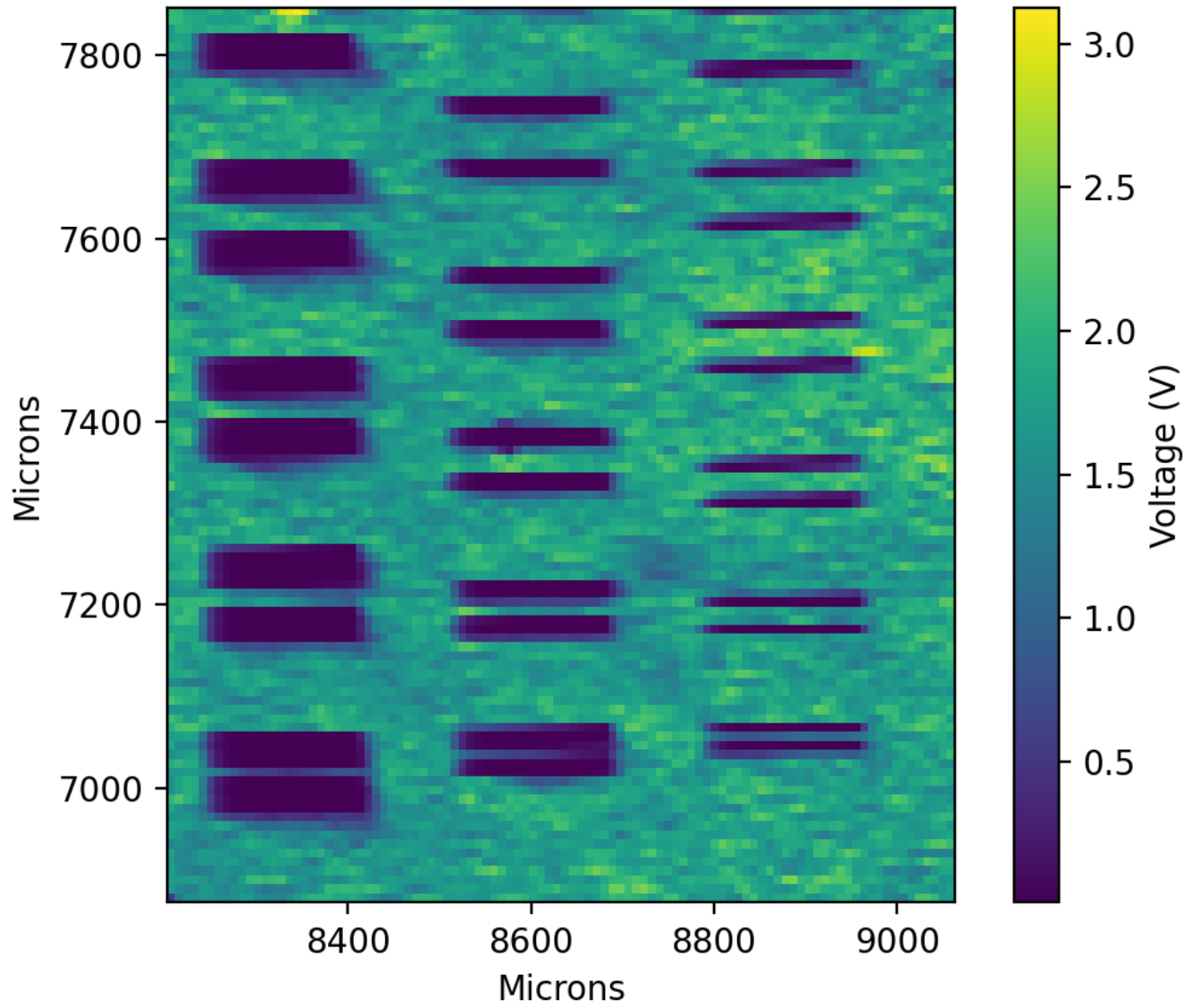


Figure 31: Scan 8.

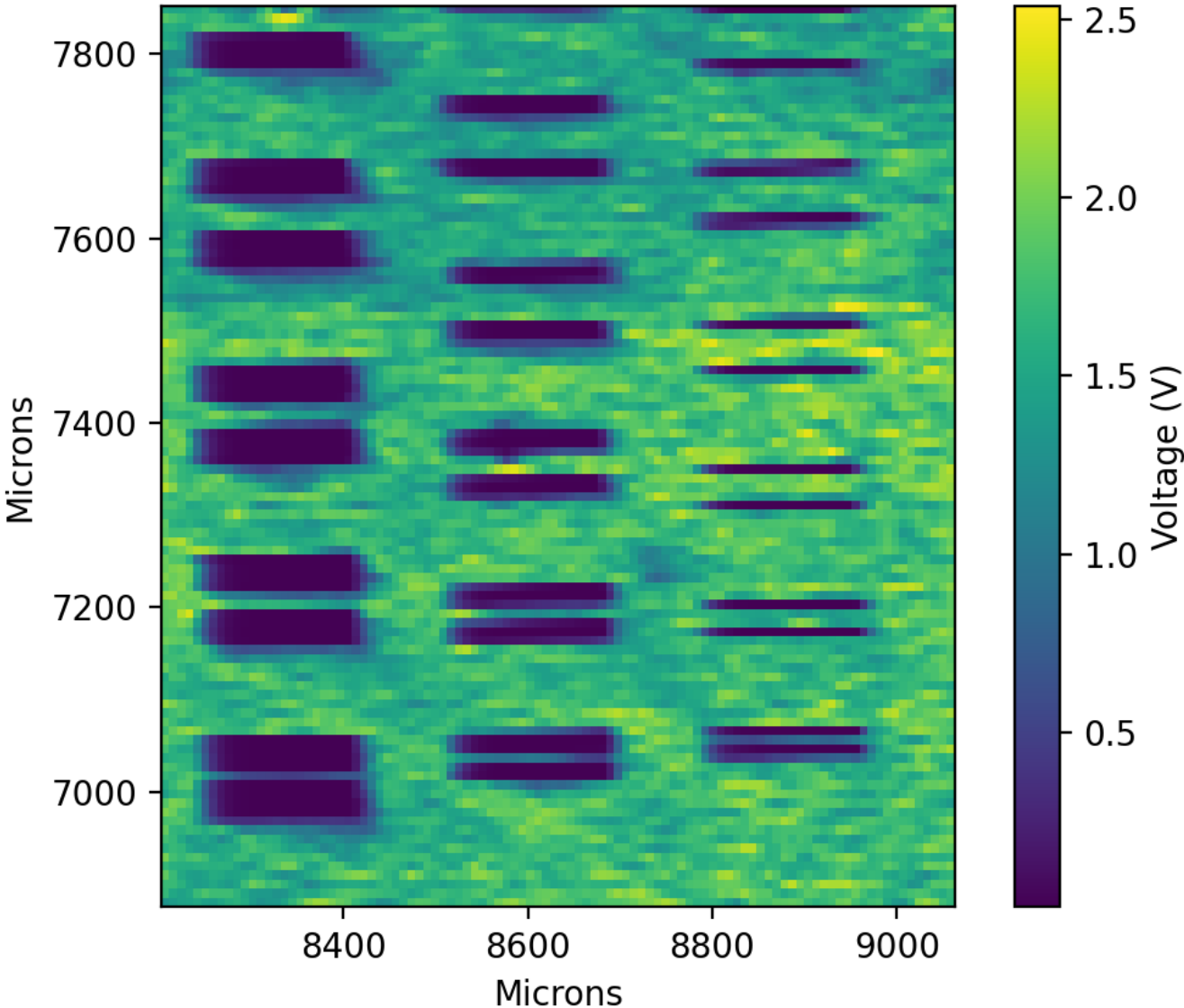


Figure 32: Scan 9.

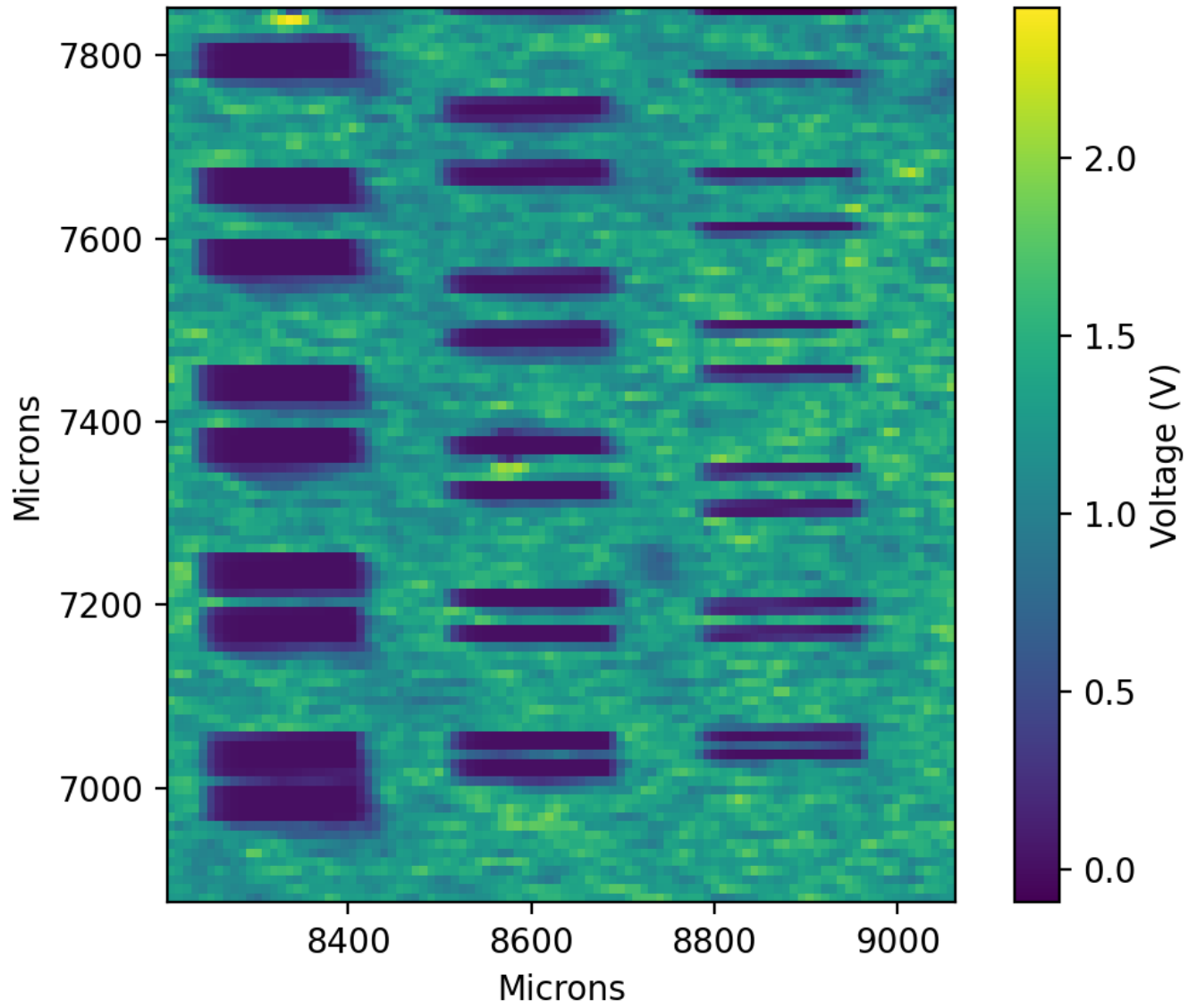


Figure 33: Scan 10.

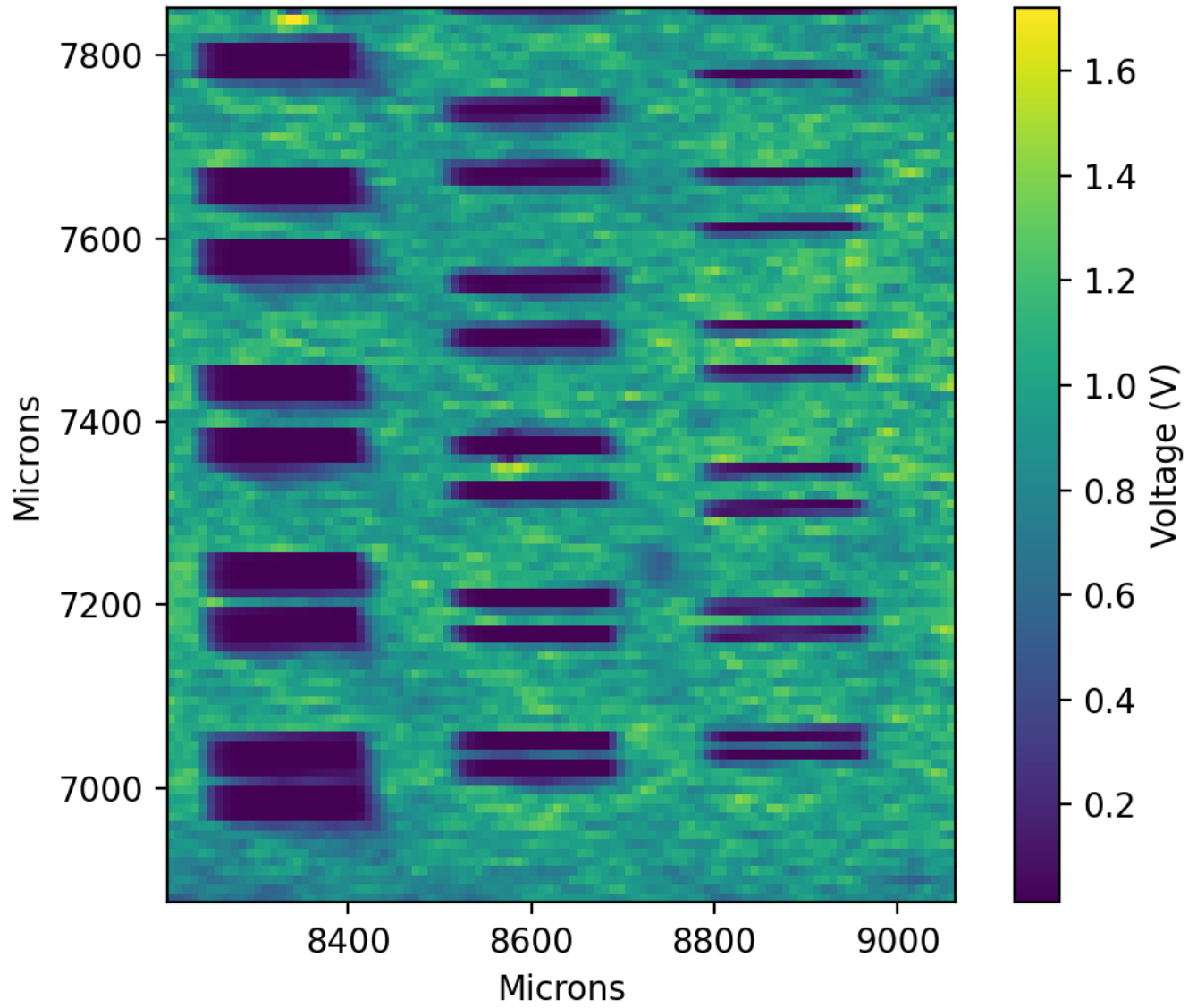


Figure 34: Scan 11.

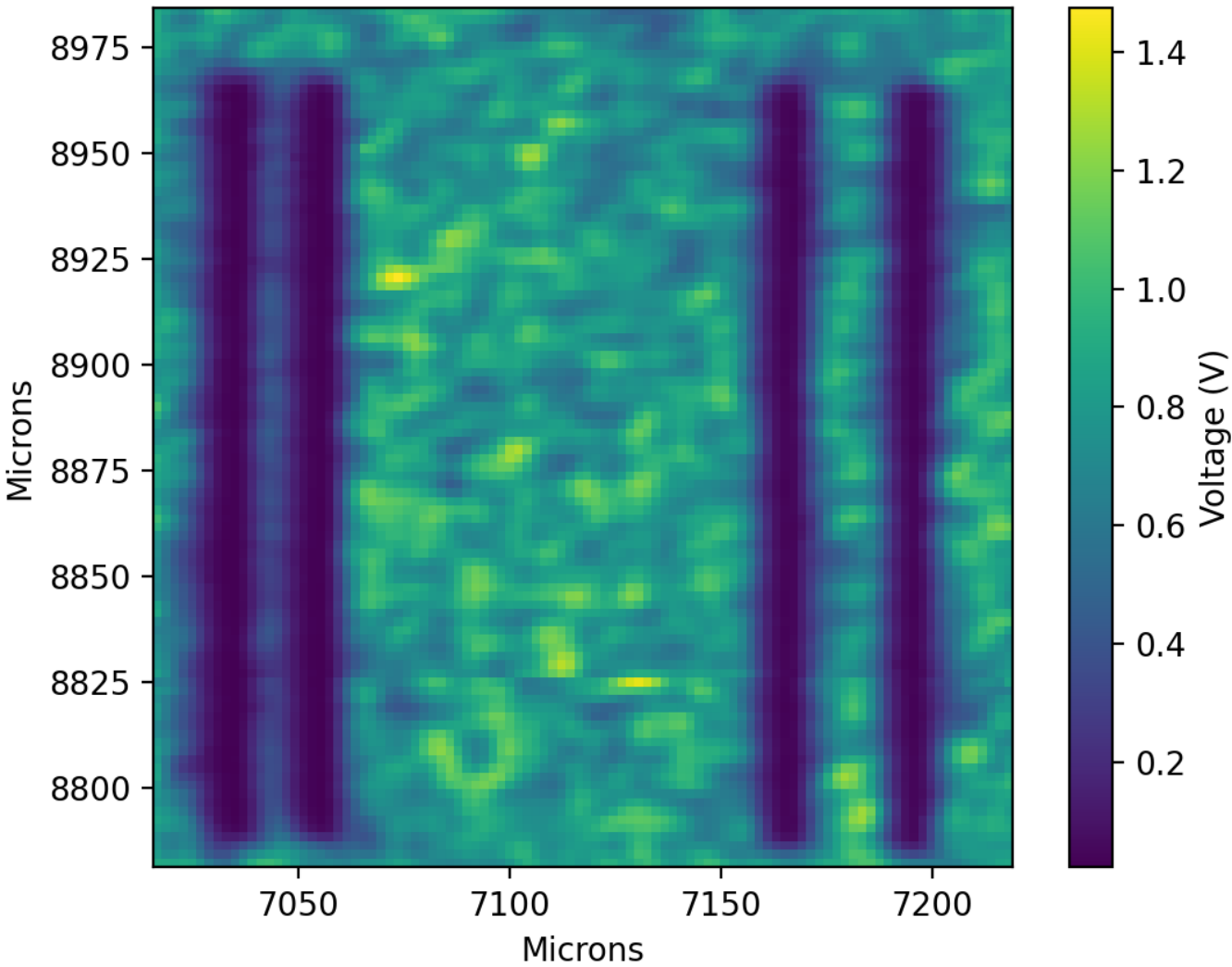


Figure 35: Scan 12.

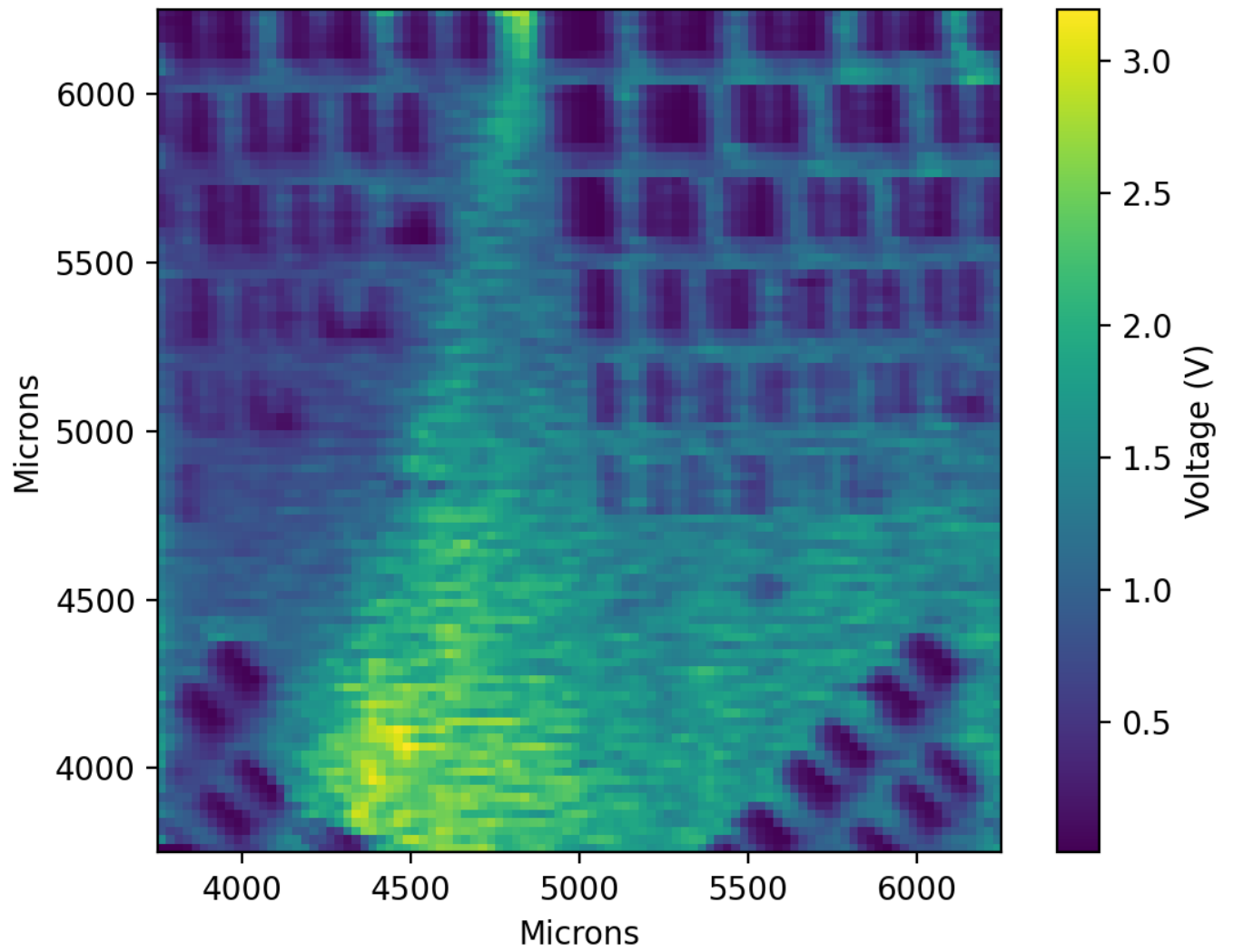


Figure 36: Scan 13.

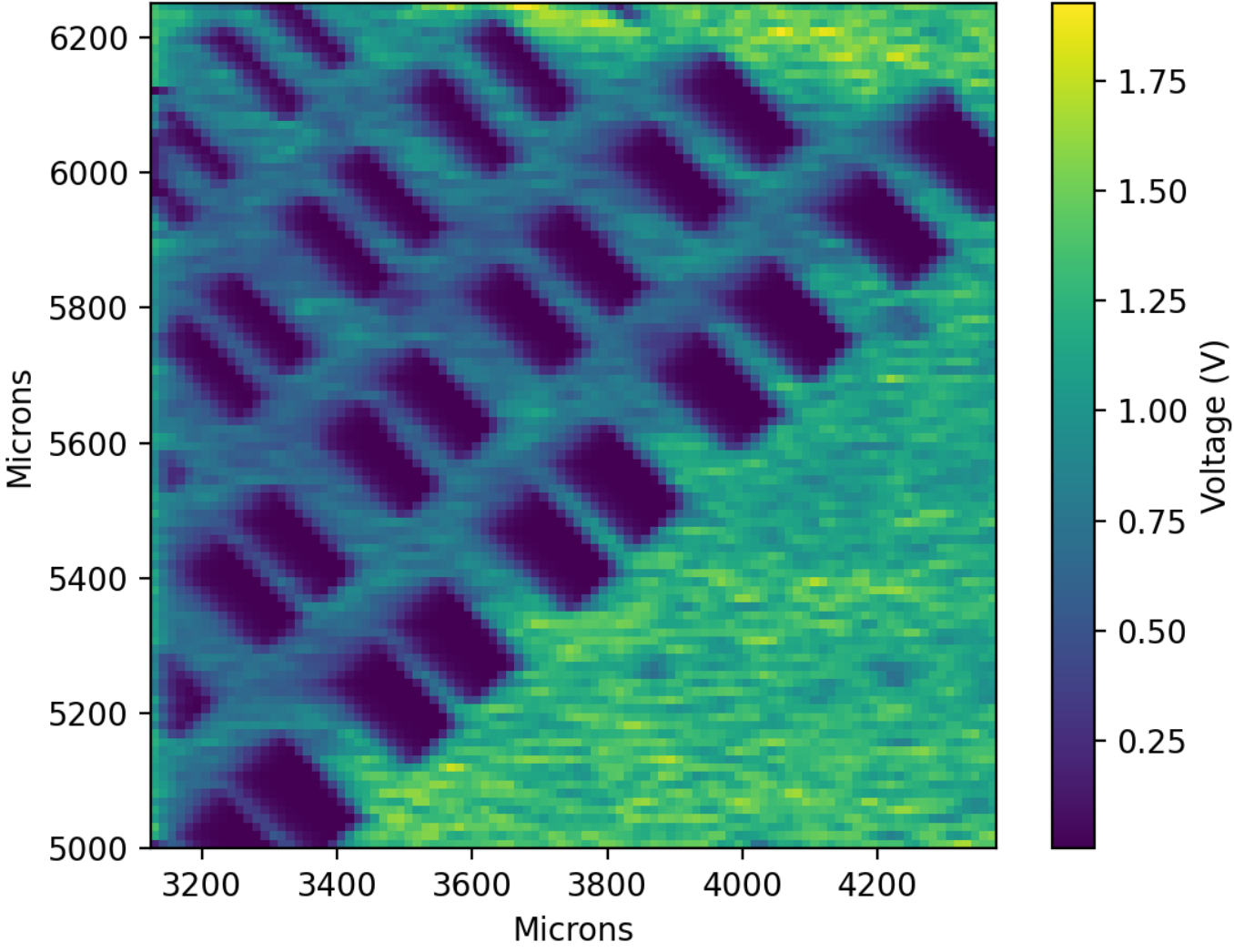


Figure 37: Scan 14.

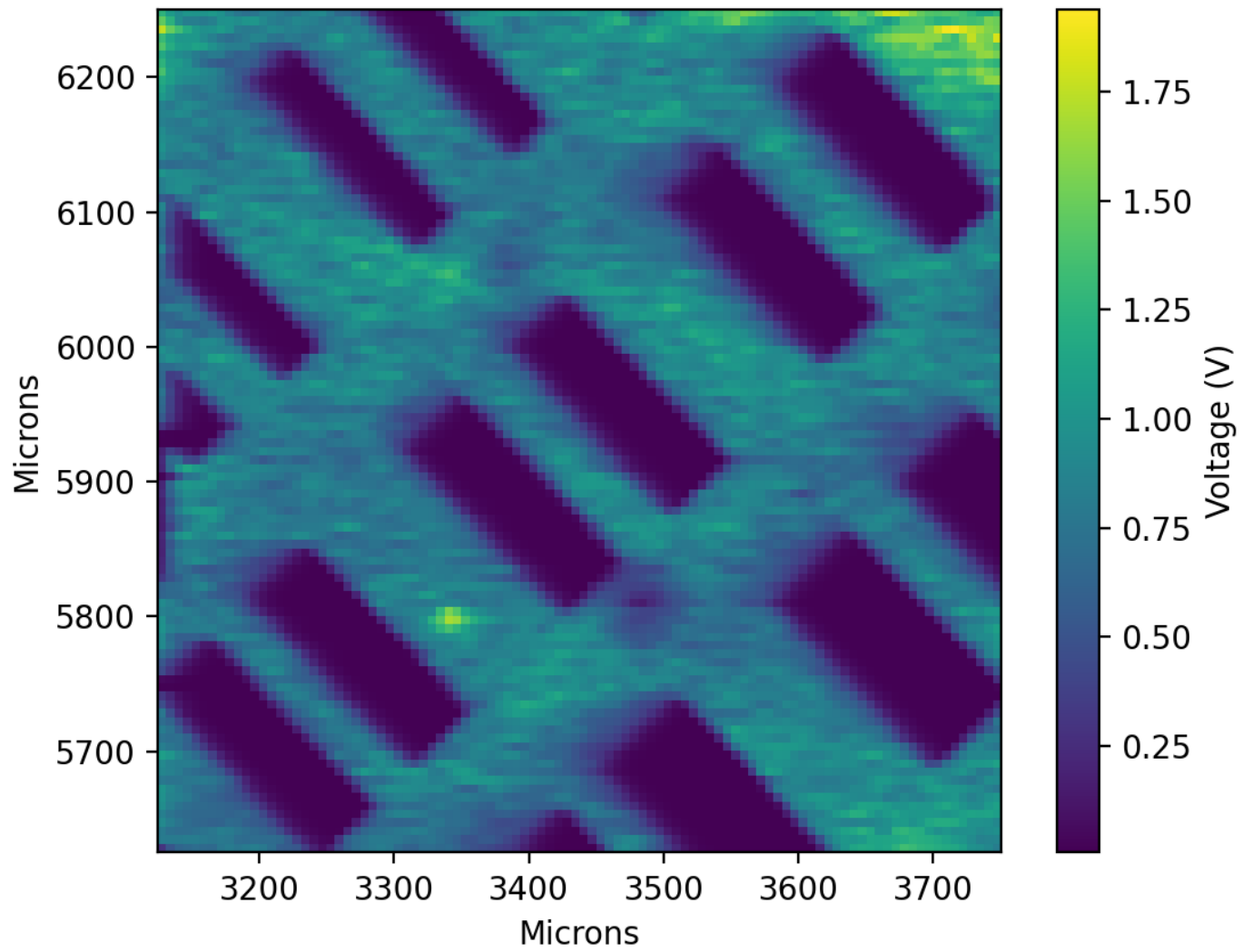


Figure 38: Scan 15.

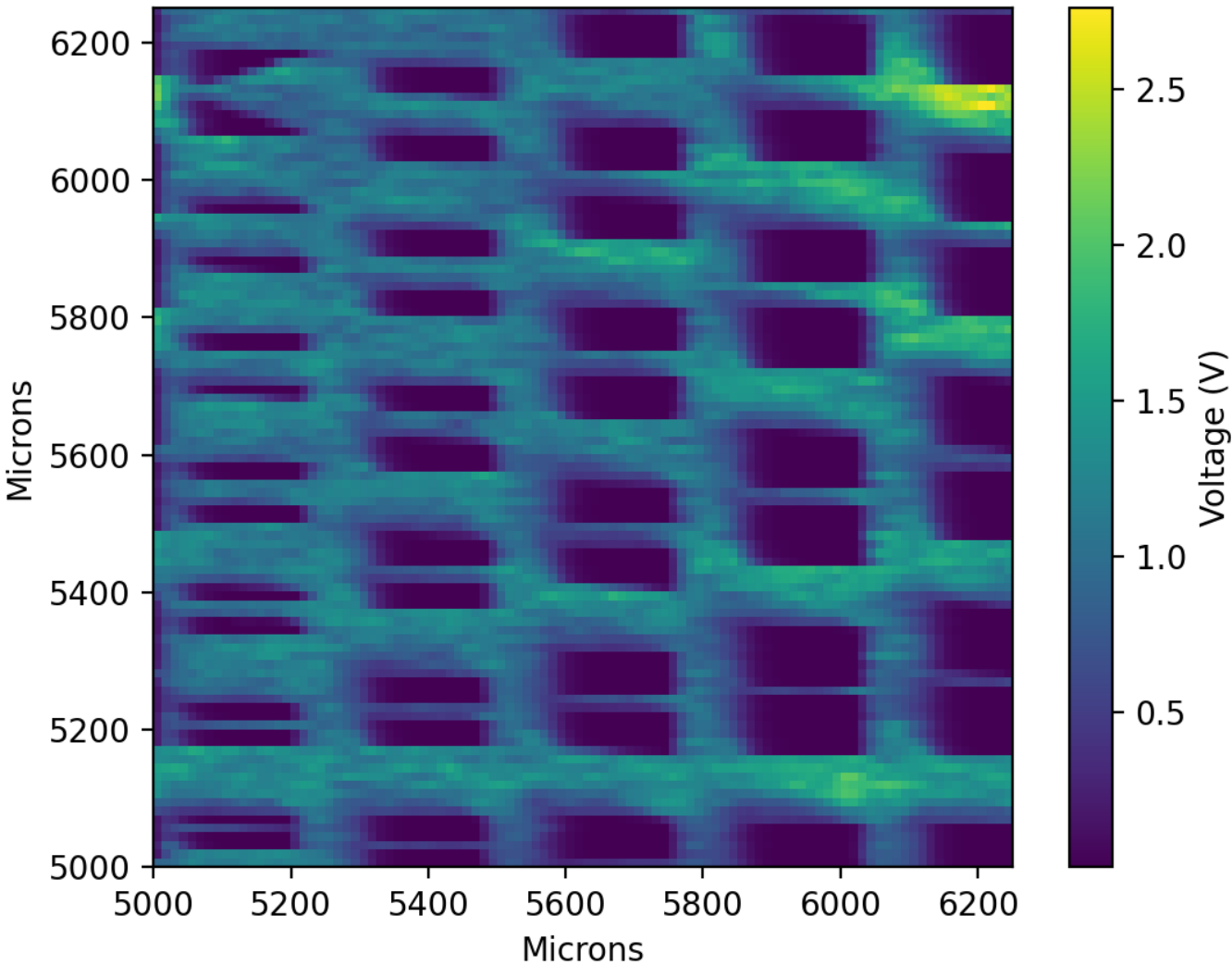


Figure 39: Scan 16.

Scan 1 covers an area of 0.391 mm^2 , where each point is $6.25 \text{ }\mu\text{m}$. The blur in the vertical side of the structures can be attributed to having no delay. Since the scan is obtained in the order X/Y, it is clear that a delay was necessary. This is expected because the time delay on the lock-in amplifier is 1 s, meaning while the lock-in was time averaging at a point, the stage had already moved to the next point. It is important to note that stage movement is not instantaneous; there is a mechanical delay. This means that setting the delay in the code to 1000 ms does not necessarily indicate that the 1 s time constant is matched. The most significant result seen in Scan 1 is that there is no PL on the structures, suggesting that the silica acted as non-growth centers, as expected. It is important to note that no PL does not necessarily mean there was no growth on silica. It is possible there is growth on the silica that is highly strained which will also result in no PL due to the high defect density.

Scan 2 scans the same region as Scan 1, however, the delay was increased to 650 ms. Adding this delay resulted in a clearer image of the structures meaning 650 ms delay is closely matched to the 1s time averaging of the lock-in. Another feature that seems more obvious in Scan 2 is that the structures seem to have a shadow effect. The PL is much weaker in the regions to the right and below the structures. There are also some regions that have no PL apart from the structures, such as at (7950, 8000). One possible explanation is that during the etching process something may have prevented that area from being etched down, such as dust or photoresist. This will have resulted in a speck of silica to be left on the sample, preventing growth in that region. Another possibility is the growth itself, where the heterostructure grown is highly non-uniform, resulting in areas with no growth. However, this second case is less likely given how uncommon this feature is seen in the scans.

Scan 3 is a zoomed out version of Scan 2, covering an area of 1.56 mm^2 , where each point

is $12.5\ \mu\text{m}$. The delay is slightly increased to 700 ms as it resulted in clearer images without taking a significant amount of time. This image is generally more blurry than Scan 2, which is expected given the distance covered is larger. An important feature to note here is high intensity PL in the top right corner of the image. This strong PL occurs in a region where there are no silica structures, indicating that not only do the structures themselves block PL, but they also reduce the intensity in neighbouring areas. Scan 6 is a repeat of Scan 3 with a longer delay time of 1000 ms in an attempt to increase image quality. There is a slight improvement however the added time was not worth the slight improvement.

Scan 4 is a zoom in to the bottom right of Scan 3, covering an area of $0.391\ \text{mm}^2$, where each point is $6.25\ \mu\text{m}$. The PL intensity between the structures is around 3 V, while the PL exceeds 10 V in the uniform region on Scan 3. Similarly, Scan 5 zooms into the bottom right of Scan 4, covering an area of $0.0977\ \text{mm}^2$, where each point is $3.13\ \mu\text{m}$. Looking at Figure 13, it is clear that the structures in Scan 5 are the second last column which has a mask width of $20\ \mu\text{m}$. This image confirms the width is approximately $20\ \mu\text{m}$ and therefore the photolithography process is successful for even thinner structures.

Scan 7 in Figure 30 captures a full group with an area scanned of approximately $3.36\ \text{mm}^2$. The increase in PL in the areas away from the structures is also evident in this scan. Another interesting feature is the higher PL response to the left ($x < 7450$) of the $100\ \mu\text{m}$ mask widths relative to the right ($x > 8950$) of the $10\ \mu\text{m}$ mask width. This is interesting because in both cases, the growth is further from the structures, yet it is much stronger near the wider masks. This is also seen on a much larger scale from left to right between $y = 8200$ and $y = 8800$. One thing to note is that on the furthest column to the right, there appears to be some missing pairs of the $10\ \mu\text{m}$ mask width. However, in Scan 8 these structures are

visible due to the improvement in resolution.

Scan 12 zooms into the bottom right two pairs of Scan 8, with a 700 ms delay. This is the most zoomed in image in this work, where each point is $2.03\ \mu\text{m}$. The structures are horizontal however they appear vertical since the scan is done in the order Y/X. The effect of blurring is more prominent here, which is expected given how fine the steps taken are and therefore the image is approaching the resolution limit. An important feature seen here is the increase in PL intensity in the regions with larger mask openings. At a fixed Y position, a slice of points can be extracted to showcase this change in PL intensity. Figure 40 is a plot of the PL intensity vs X at $Y \approx 8883$ (the 50th row in Y). The PL intensity between the pair on the right (around $X = 165$) is about 0.87 V, noticeably higher than the left pair (around $X = 27$) with an intensity of about 0.42 V. This is consistent with what is seen on a much larger scale in other scans where PL intensity is reduced within the vicinity of the structures.

Unlike the previous scans, Scans 13-16 look at a different region with vertical and diagonal structures. Scan 13 covers an area of $6.25\ \text{mm}^2$ at a wavelength of 880 nm. Scans 14 and 15 are a close up of the bottom right of Scan 13, done in the stage order Y/X. Similar features are seen, where the PL is weaker near the structures. Scan 16 is a zoom of the top right of Scan 13, also done in the order Y/X. The regions with higher PL are around the wider masks ($X = 6200$), specifically near the top where the mask opening is larger. This is also seen diagonally in the middle of Scan 14, where the mask opening is largest. Sugiyama et al. found that a mask width should be more than $100\ \mu\text{m}$ in order to obtain substantial modulation of the wavelength [7]. Even though the peak wavelength is not shifting, the larger mask widths may have affected the growth rate leading to a higher PL intensity, relative to

the smaller mask widths. Another possibility is that because the widest masks are closer to the areas with no silica masks (between the groups), then the PL suppression from the presence of silica masks is not as prominent. The latter conjecture is more likely because this is also seen in the top right of Scan 14, where the mask widths are smaller. Nonetheless, the most apparent feature is the PL suppression in regions near the silica structures, regardless of mask width and/or opening, which was not expected. One possible mechanism affecting the PL intensity is the quality of the DH growth. Lower PL intensity can be the result of damage, dislocations, or strain from lattice mismatch.

There are two ways SAG can alter growth: thickness modulation and alloy composition shift. It is possible the InGaP is changing in a way that degrades confinement. Compared to the GaAs, the InGaP layers are very thin making them relatively sensitive to changes from SAG. Since there is only one group-III element in a binary compound, there should be no change in atomic content of GaAs and hence no wavelength shifts observed in PL. However, the InGaP buffer and cap layers are ternary compounds and can experience compositional changes. These compositional changes will not be detected by analyzing the wavelength since the PL wavelength is governed by the GaAs. Alternately, looking at the PL intensity may shed some light on the quality of the InGaP grown. One possibility is that as the group-III ratio of the InGaP changes, the growth conditions change, increasing the defect density and hence lowering the PL intensity. If the group-III ratio changes, then the effect of strain from lattice mismatch will be more prominent depending on how drastic the compositional changes are. Another possibility is that because of the atomic content variations in InGaP, the bandgap will change and thus reduce the confinement, ultimately lowering the PL intensity.

In Figure 40, the structures are the regions where the PL dips toward zero. The slope is

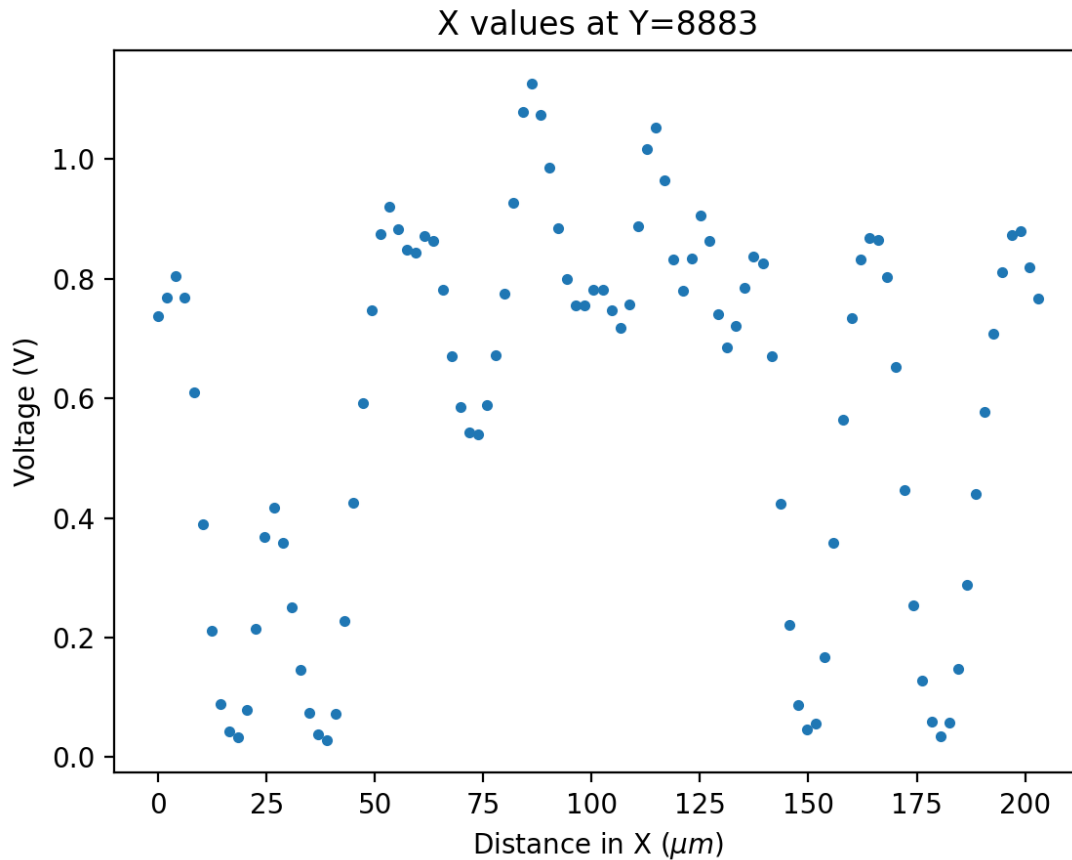


Figure 40: PL intensity of the X values corresponding to $Y = 8883$ of Scan 12.

not perfectly sharp; it is about 3 points wide which is attributed to the blurring seen around the structures. The resolution is likely around 3 points, or about $6 \mu\text{m}$ (since each point is $2 \mu\text{m}$). There are many factors affecting resolution of the image. The most obvious case is that the lens is not in perfect focus; the focal length is very sensitive to small changes in distance. However, one of the more likely factors affecting the resolution is that the wavelength range of the objective lens is 435-655 nm. This is sufficient for allowing the laser light to excite the carriers, however the PL captured at 880 nm will be somewhat aberrated. The resolving power of this objective lens is $0.4 \mu\text{m}$ with NA (numerical aperture) = 0.7. Abbe's diffraction formula for lateral (i.e. XY) resolution is $d = \frac{\lambda}{2NA}$. Using $\lambda = 880$

nm, the theoretical resolution is slightly better, at $0.3\ \mu\text{m}$. Given these values, the spatial resolution of the scans may be improved by 10x. However, the stage repeatability is $< 2\ \mu\text{m}$, and therefore a spatial resolution better than $2\ \mu\text{m}$ is not expected. It is possible that the resolution is also affected by the exciton diffusion length, however this is dependant on the material quality and therefore more information is needed.

Scan 9 is a repeat of Scan 8 with a shorter time delay of 700 ms. The longer delay time in Scan 8 did not improve the image significantly, and thus 700 ms is sufficient. Scans 9-11 scan the area under the same conditions at different wavelengths. According to Figure 20, the peak voltage is around 880 nm, and therefore having the PL at 870, 880 and 890 nm will allow fitting to a parabola to extract the peak wavelength. Scans 9, 10 and 11 have a constant wavelength of 880, 870 and 890 nm, respectively. Overall, the PL intensity is strongest at 880 nm and weakest at 890 nm. This is consistent with the general shape of a GaAs peak; the shape of the curve is not symmetric. As seen in Figure 21, the PL intensity picks up fast towards the peak, and then relaxes even faster. Figure 41 shows the peak wavelength of Scans 9-11 by fitting the 3 points to a parabola using polyfit in Python. Since the structures have no PL regardless of wavelength, the fitting in those regions is not useful. However, in the neighbouring region, the peak wavelength is on average approximately 878.5 nm. This was calculated by ignoring wavelength values below 871 nm and greater than 889 nm. These values are evident in Figure 42 where the spikes at 870 nm and 890 nm correspond to the wavelength fitting in the regions near the structures or on the structures themselves. This is also the case in Figure 43 where there is a high frequency of values at 0 V and leading up to 1 V due to the structures and the vicinity of the structures, respectively. The accuracy of this fitting is limited by the non-symmetric shape of a GaAs peak. Since a wavelength

shift is not expected for MBE SAG, exploring better fitting options is beyond the scope of this work. Figure 44 is the corresponding peak voltage to the peak wavelength extracted from the fitting. This image is most similar to Scan 9, which is expected because the peak wavelength is closest to 880 nm.

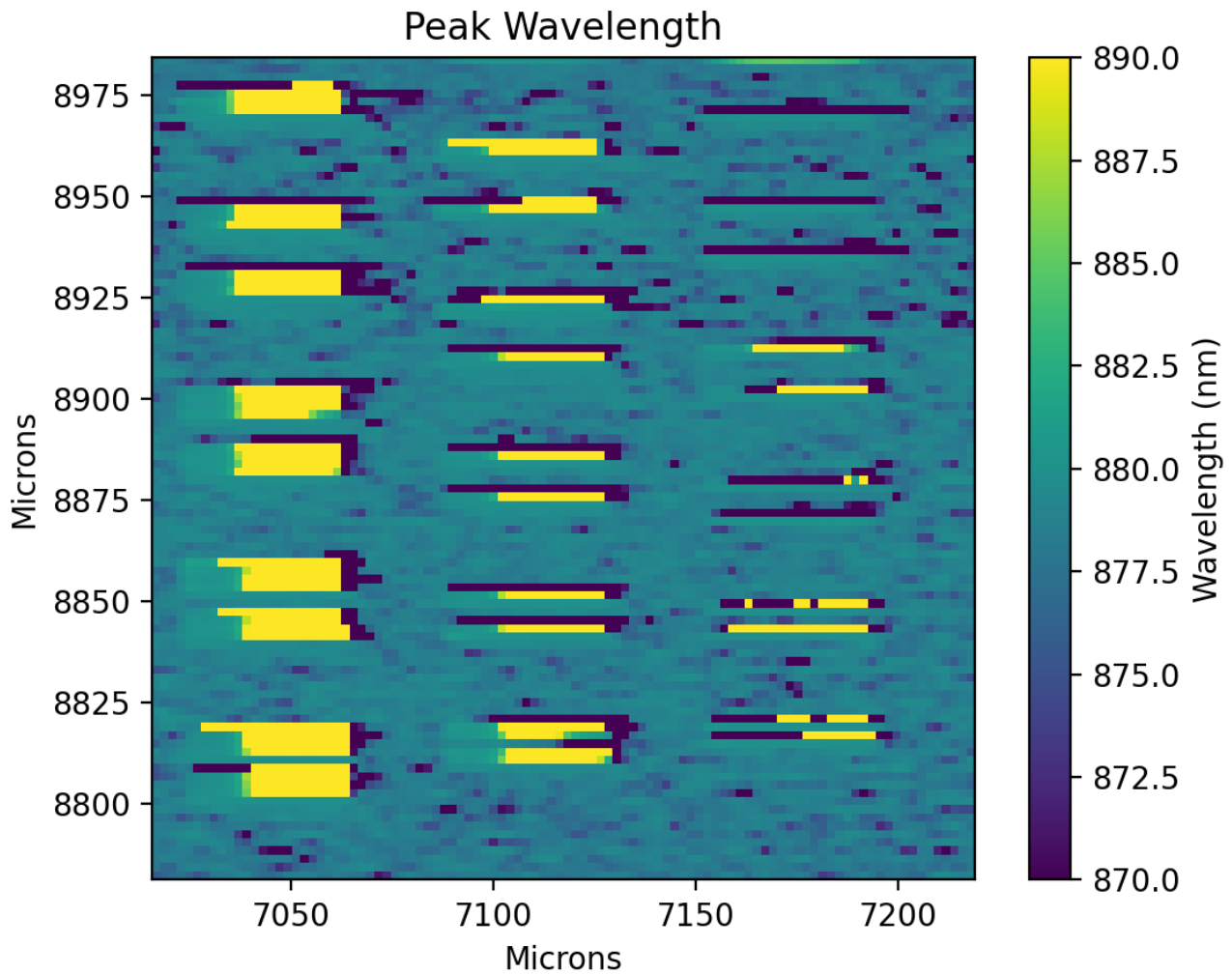


Figure 41: Peak wavelength of the Scans 9-11.

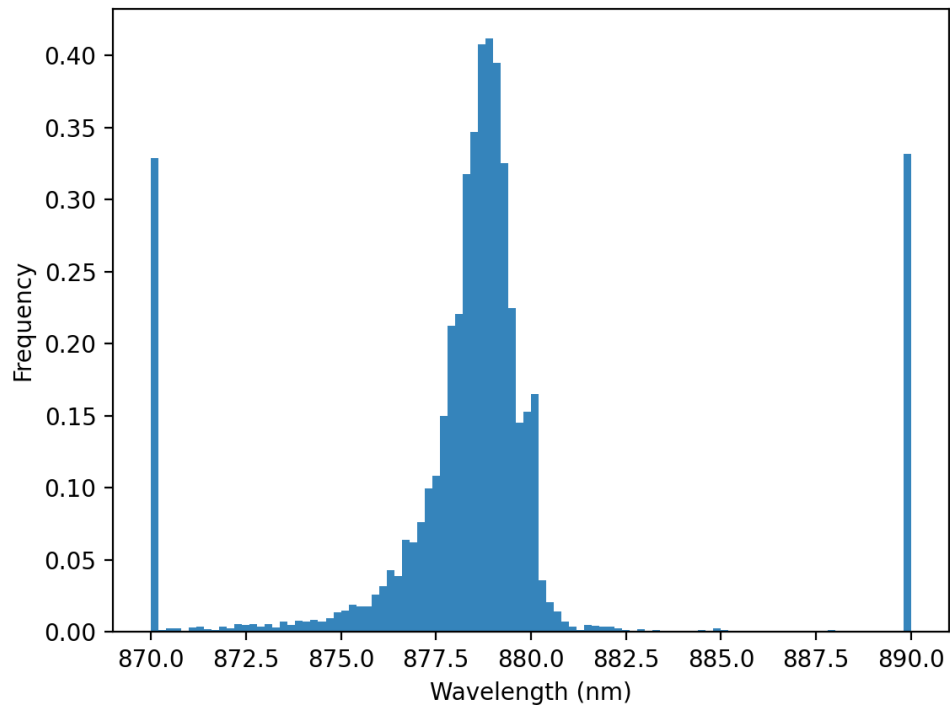


Figure 42: Histogram of peak wavelength of the Scans 9-11.

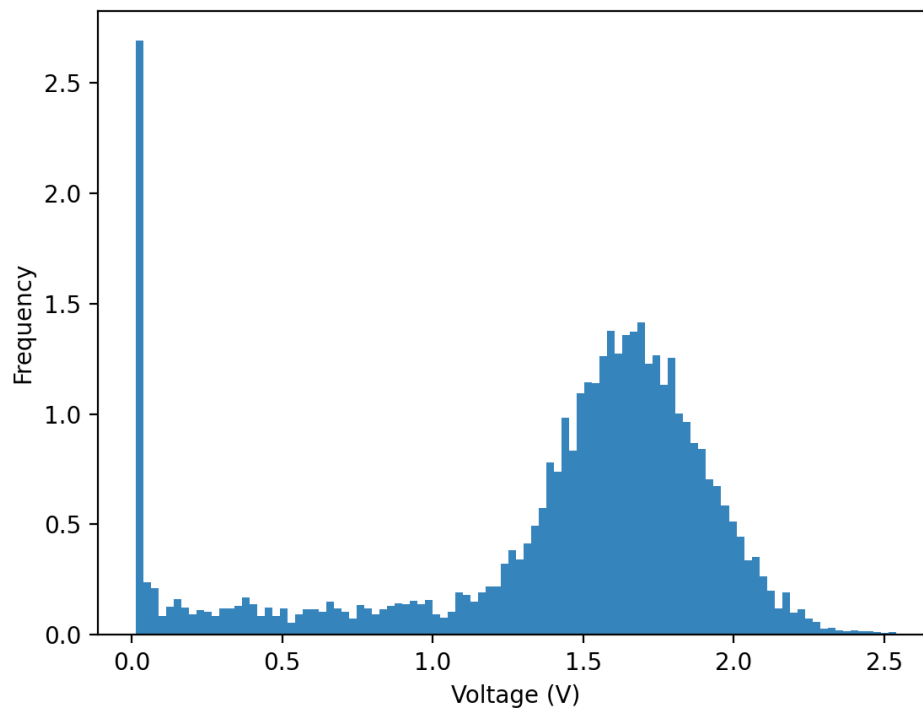


Figure 43: Histogram of peak voltage of the Scans 9-11.

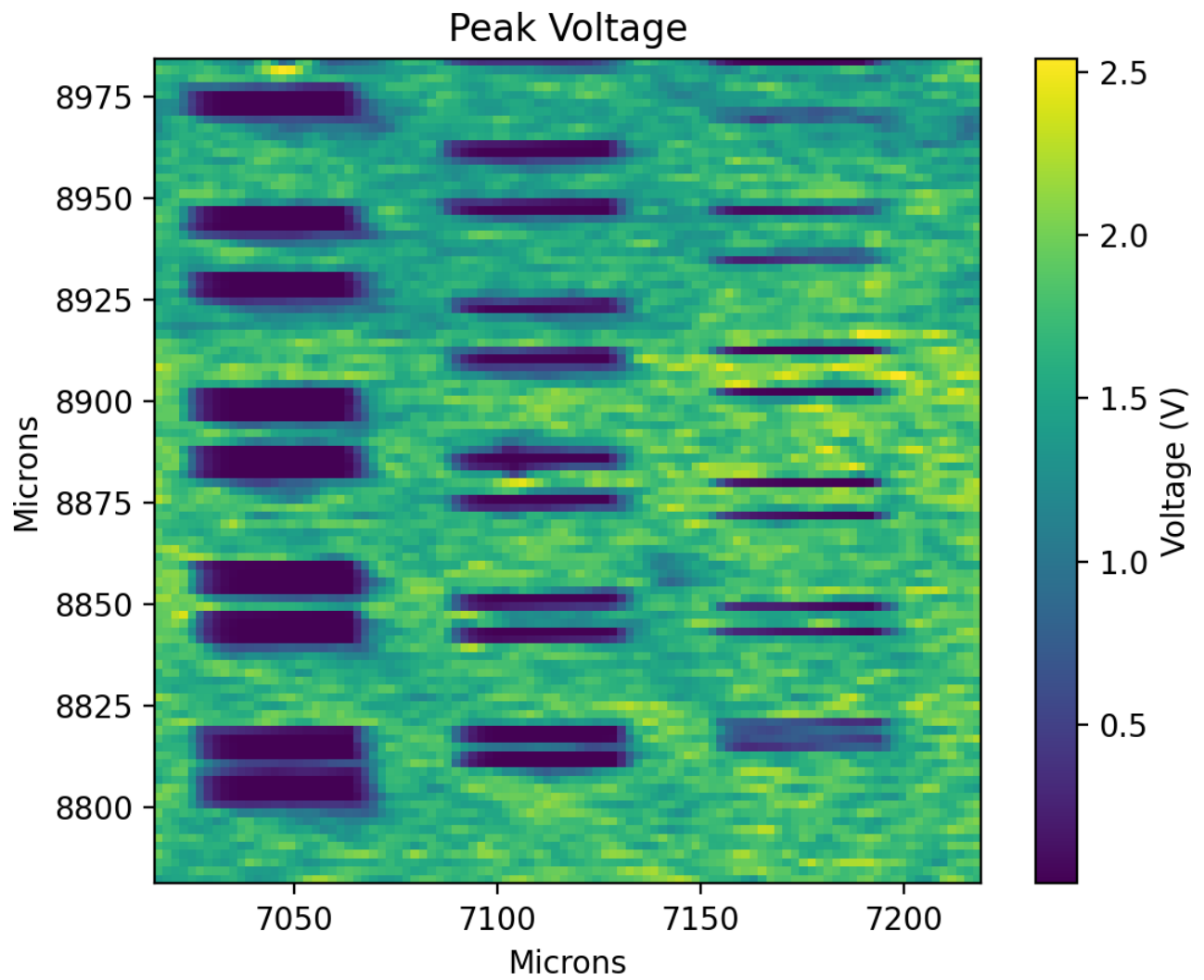


Figure 44: Peak voltage of the Scans 9-11.

4.2 Microscope Imaging

The patterned SI-GaAs sample was taken to McMaster's clean room facility to be analyzed under the microscope. The microscope is a Leica HC microscope with 5x, 10x, 20x, 50x, and 100x magnification objective lenses. The sample was placed in the same orientation as the PL imaging setup.

It is clear from the 5x (Figure 45) and 10x (Figure 46) magnification that there are defects present on the sample around the structures and in between them. This was also seen in the PL imaging where there are points that have no PL that are not the structures. These defects can arise from the processing where the silica is not etched in certain regions due to residual photoresist. Another possibility is the sample was damaged during processing or potentially during growth. Defects can also arise during growth. Generally, this is less likely because the heterostructure is lattice-matched, however the PL images show that the silica masks have an effect on the growth quality.

Figures 47-49 and 50-52 showcase the different structure orientations under 20x and 50x magnification, respectively. Like the previous magnifications (5x and 10x), it is clear that the photolithography was successful in creating the silica structures, including the tapered structures in Figure 52. There is an interesting feature that is seen in Figure 47 (20x lens) where the right sides of the structures are not straight. This is also seen more clearly in Figures 56-58 in the 100x magnification. This curved side is only seen on the right sides of the structures, regardless of structure orientation. This is most likely from the lithography, where exposure may not have been precise.

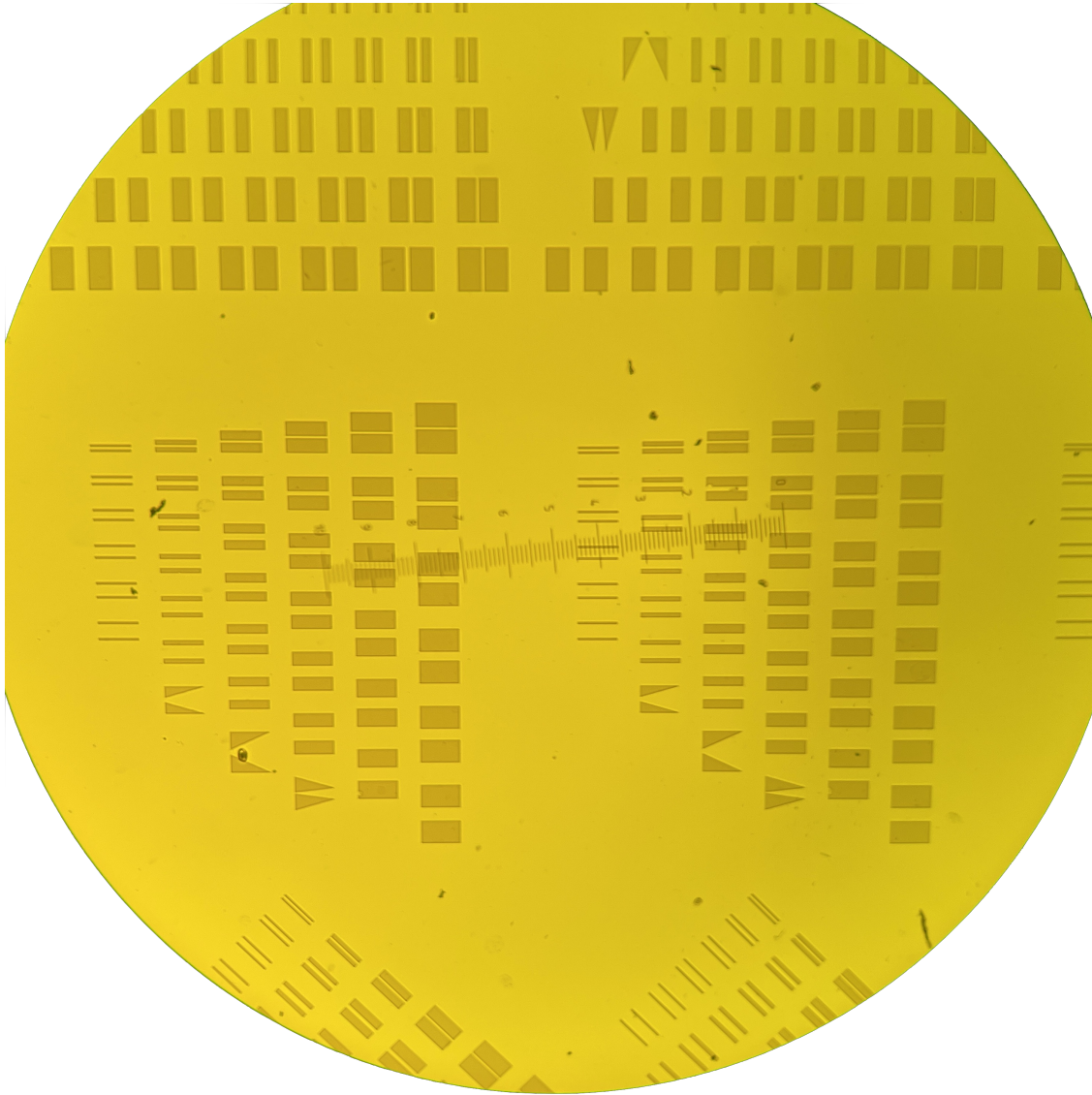


Figure 45: 5x objective.

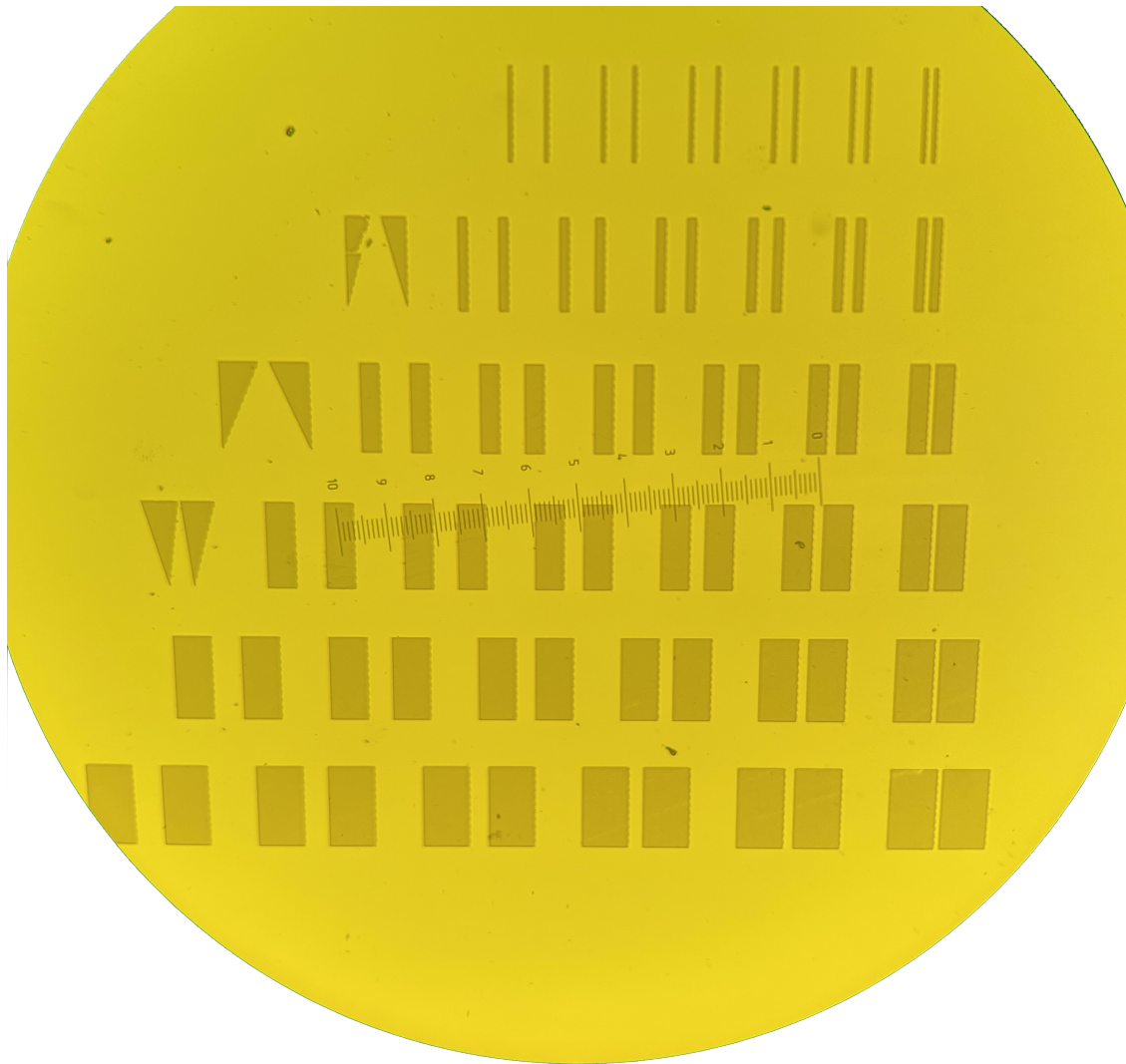


Figure 46: 10x objective.

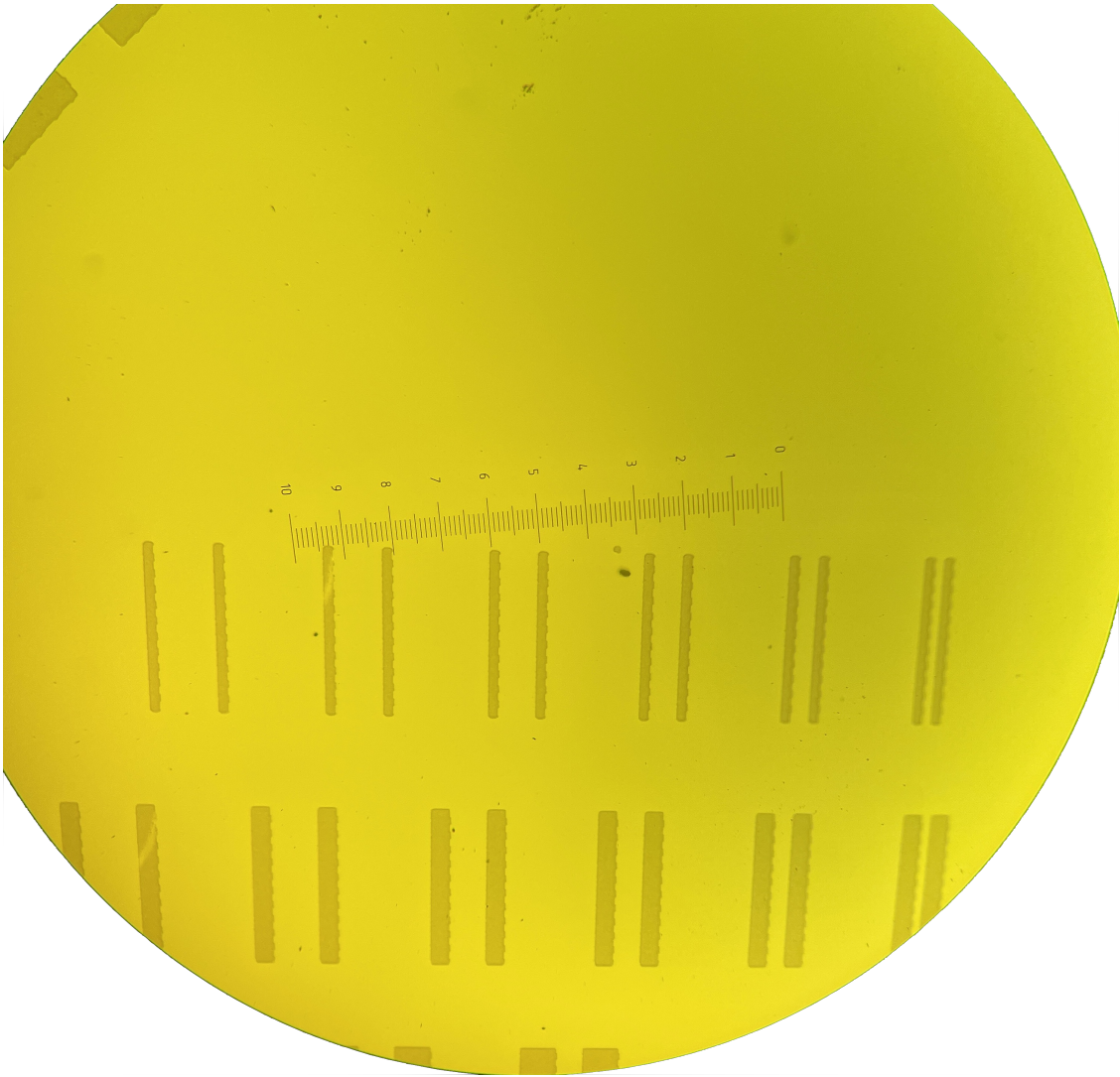


Figure 47: 20x objective: vertical structures.

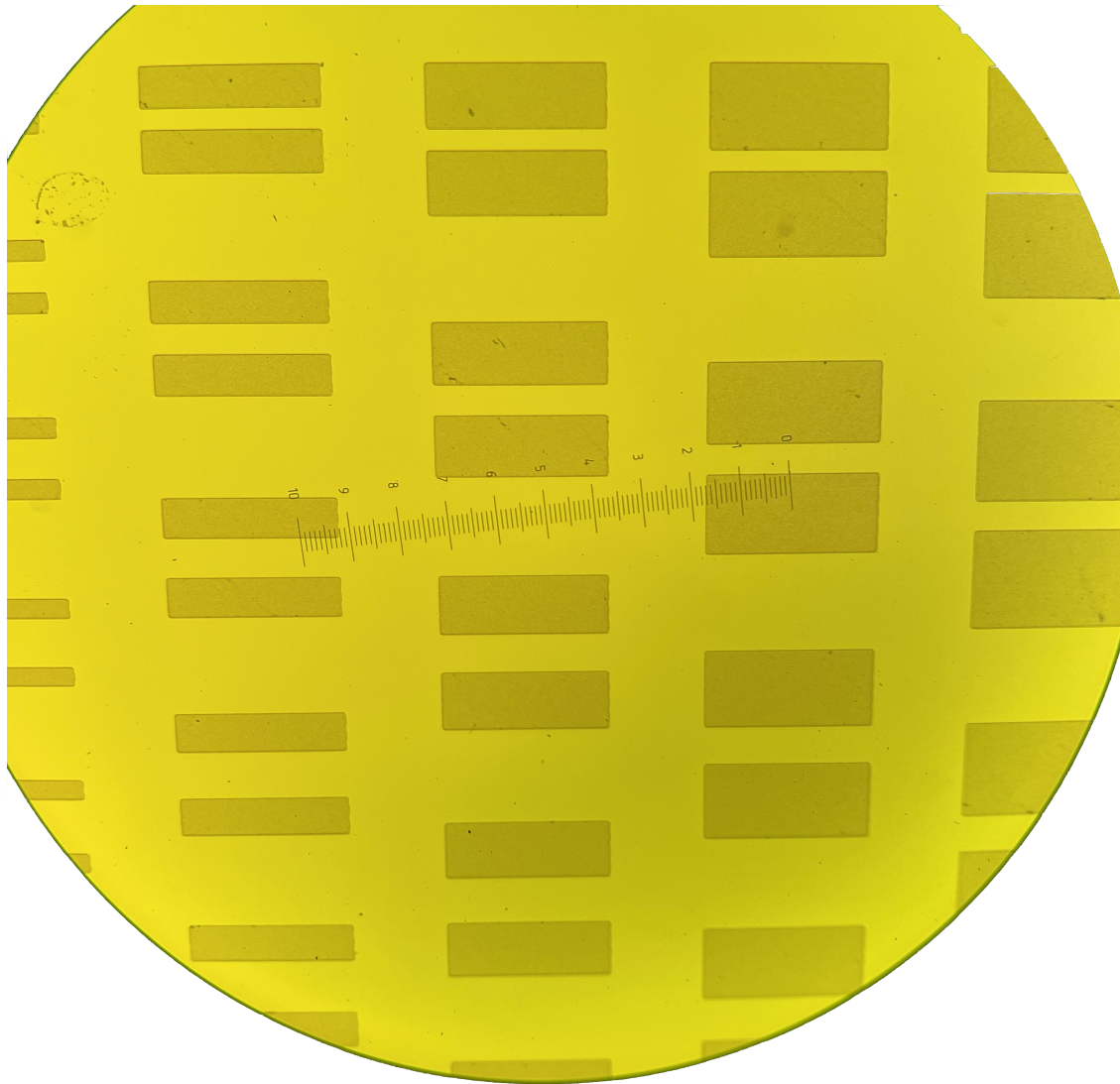


Figure 48: 20x objective: horizontal structures.

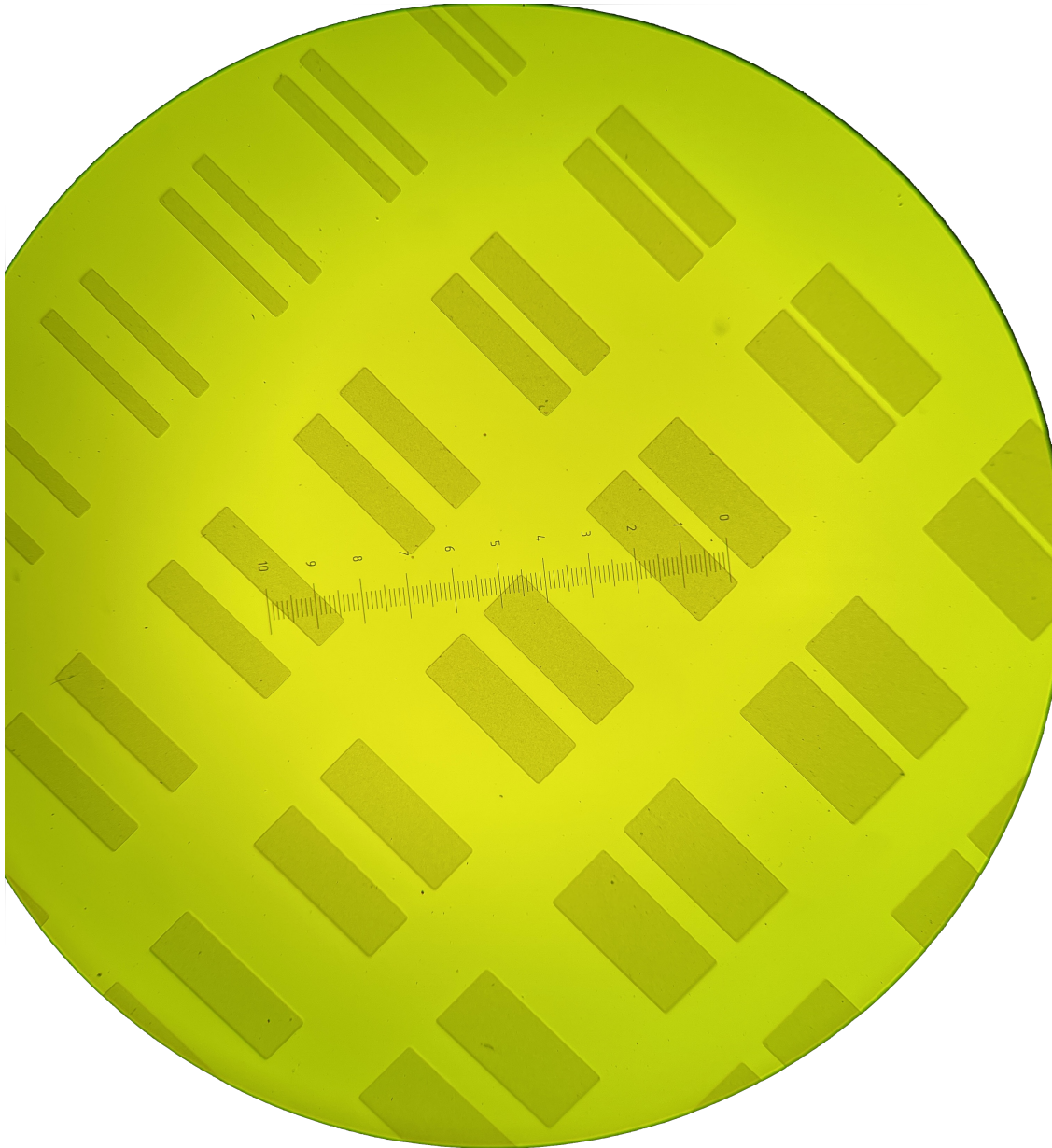


Figure 49: 20x objective: diagonal structures.

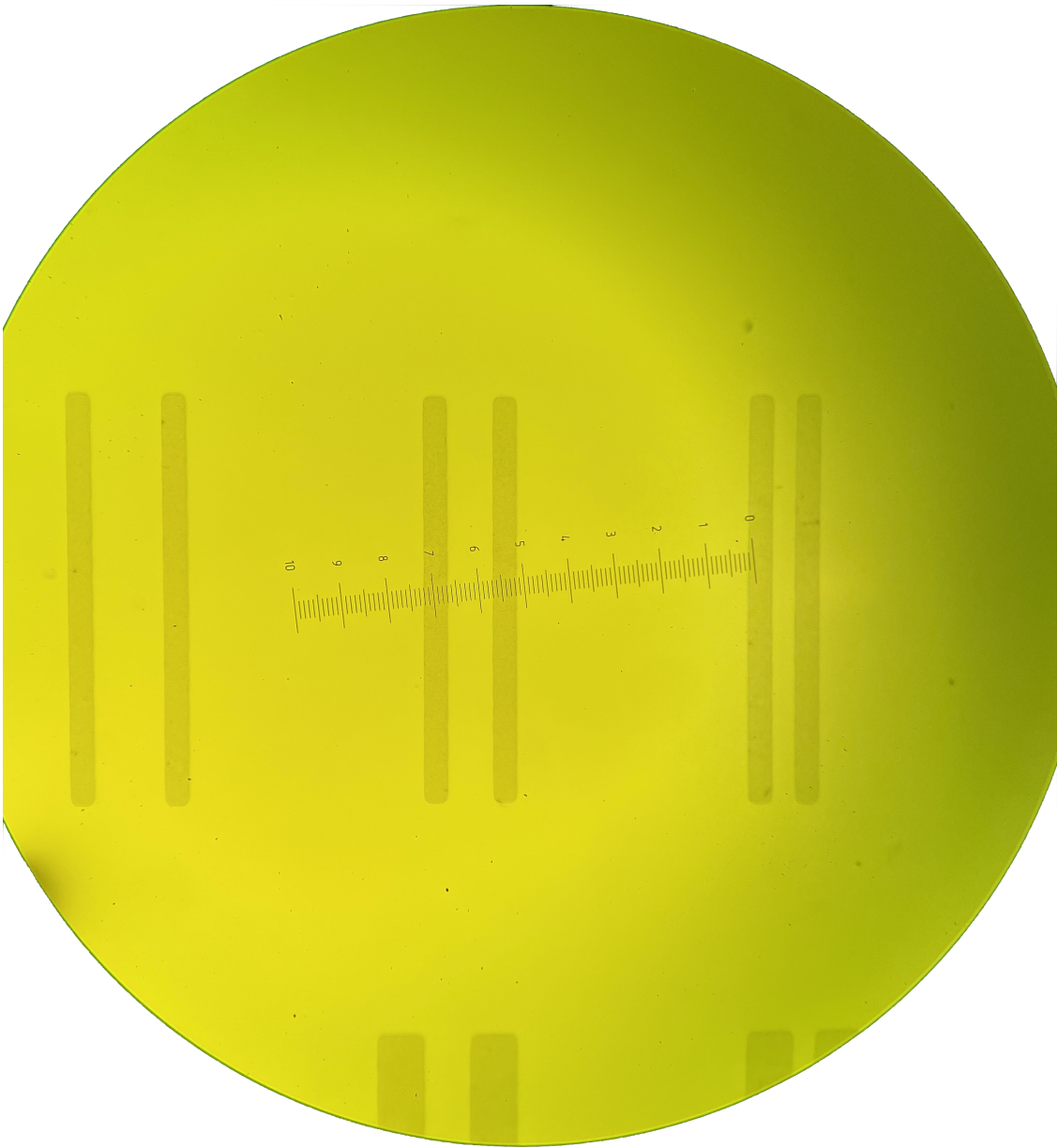


Figure 50: 50x objective: vertical structures.



Figure 51: 50x objective: horizontal structures.

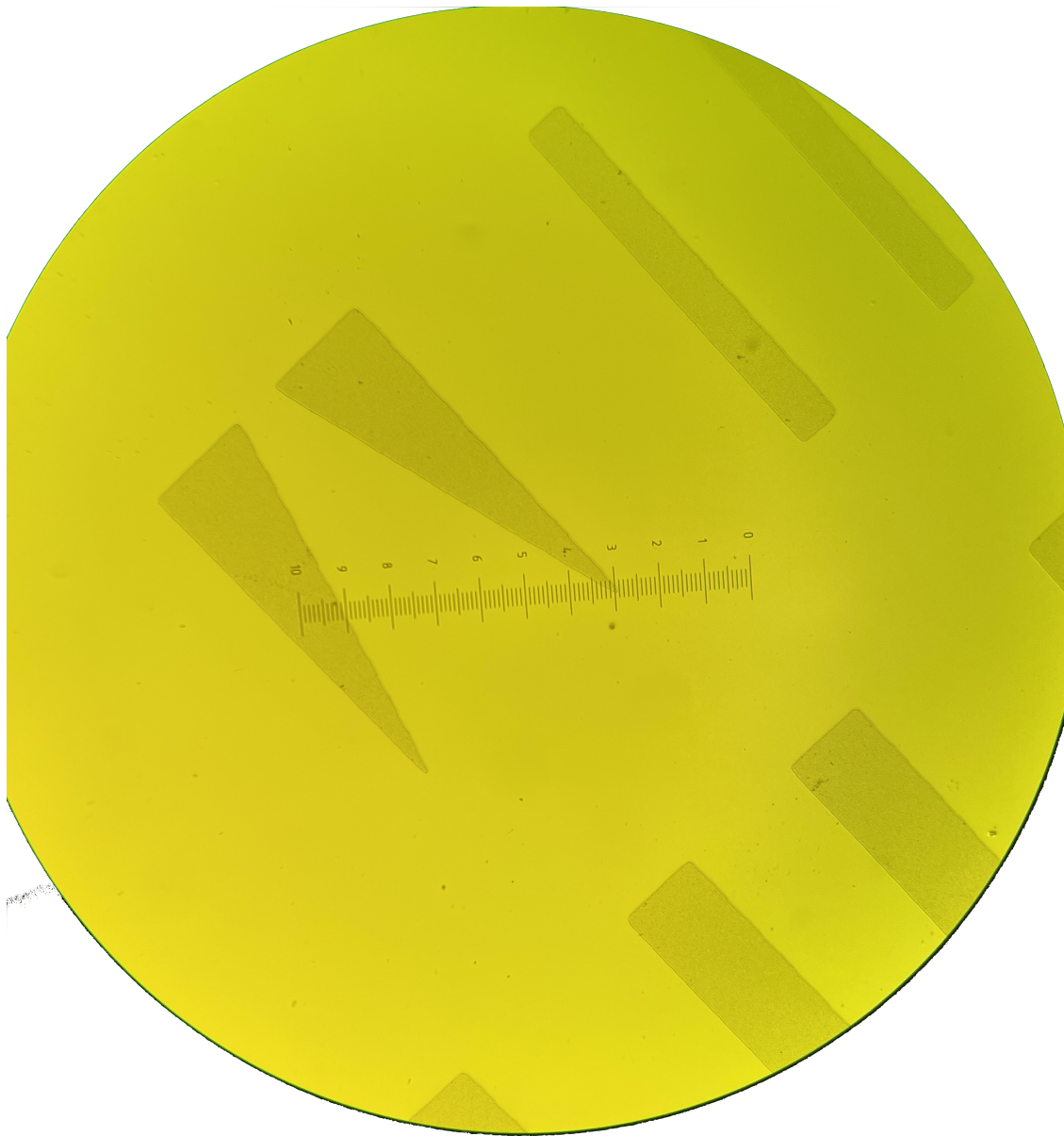


Figure 52: 50x objective: diagonal structures.

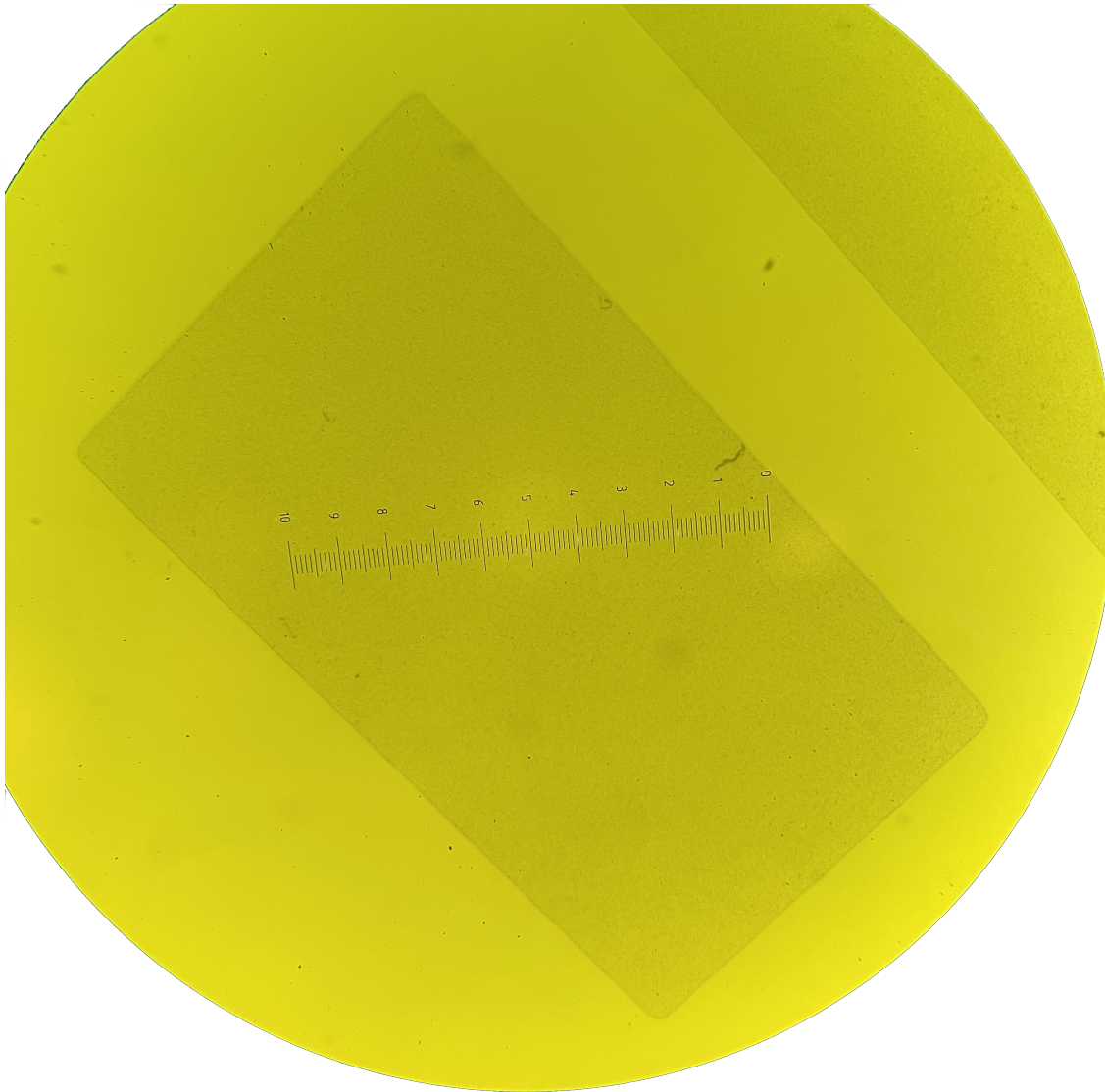


Figure 53: 100x objective: vertical structures.

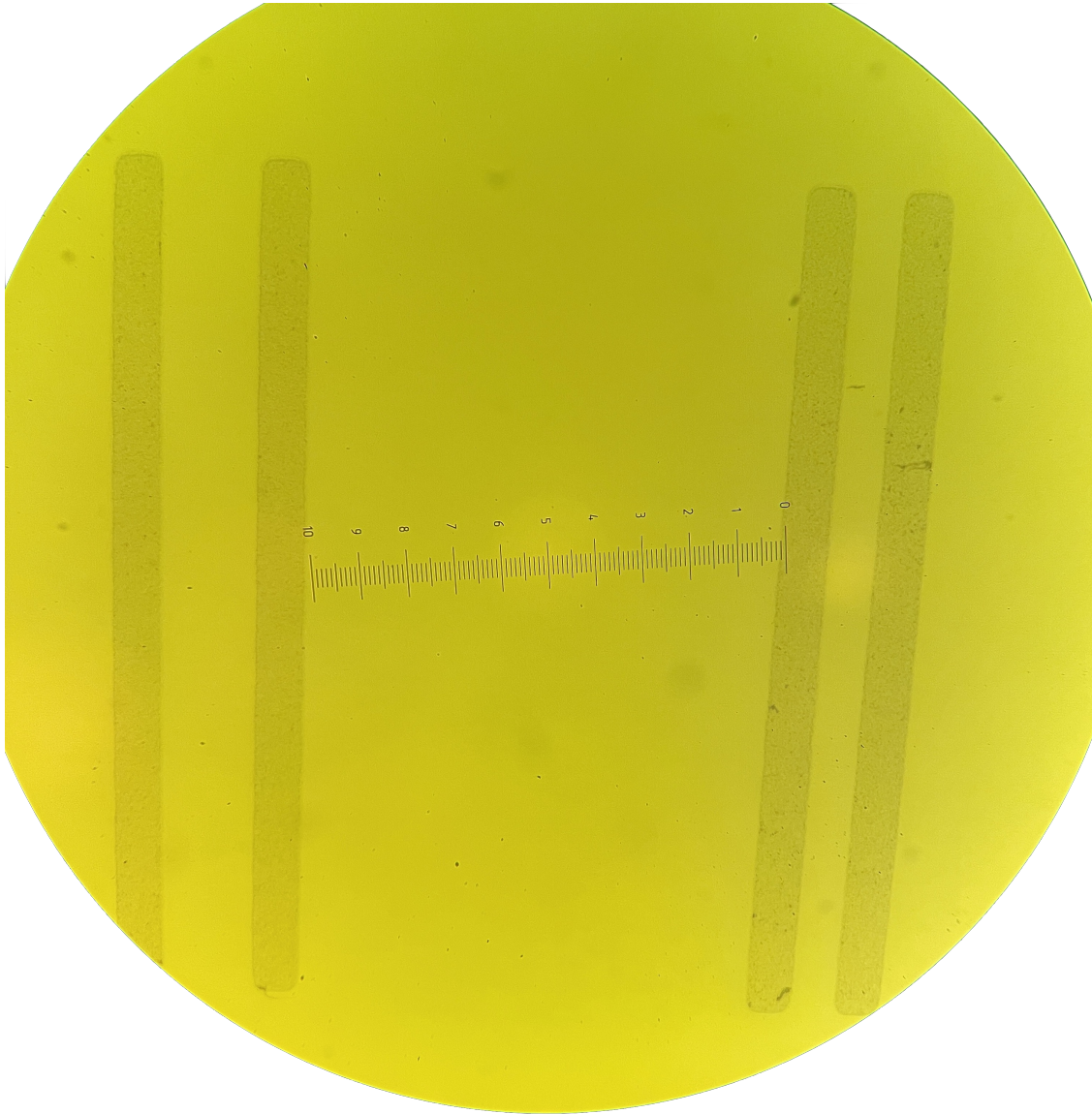


Figure 54: 100x objective: vertical structures.

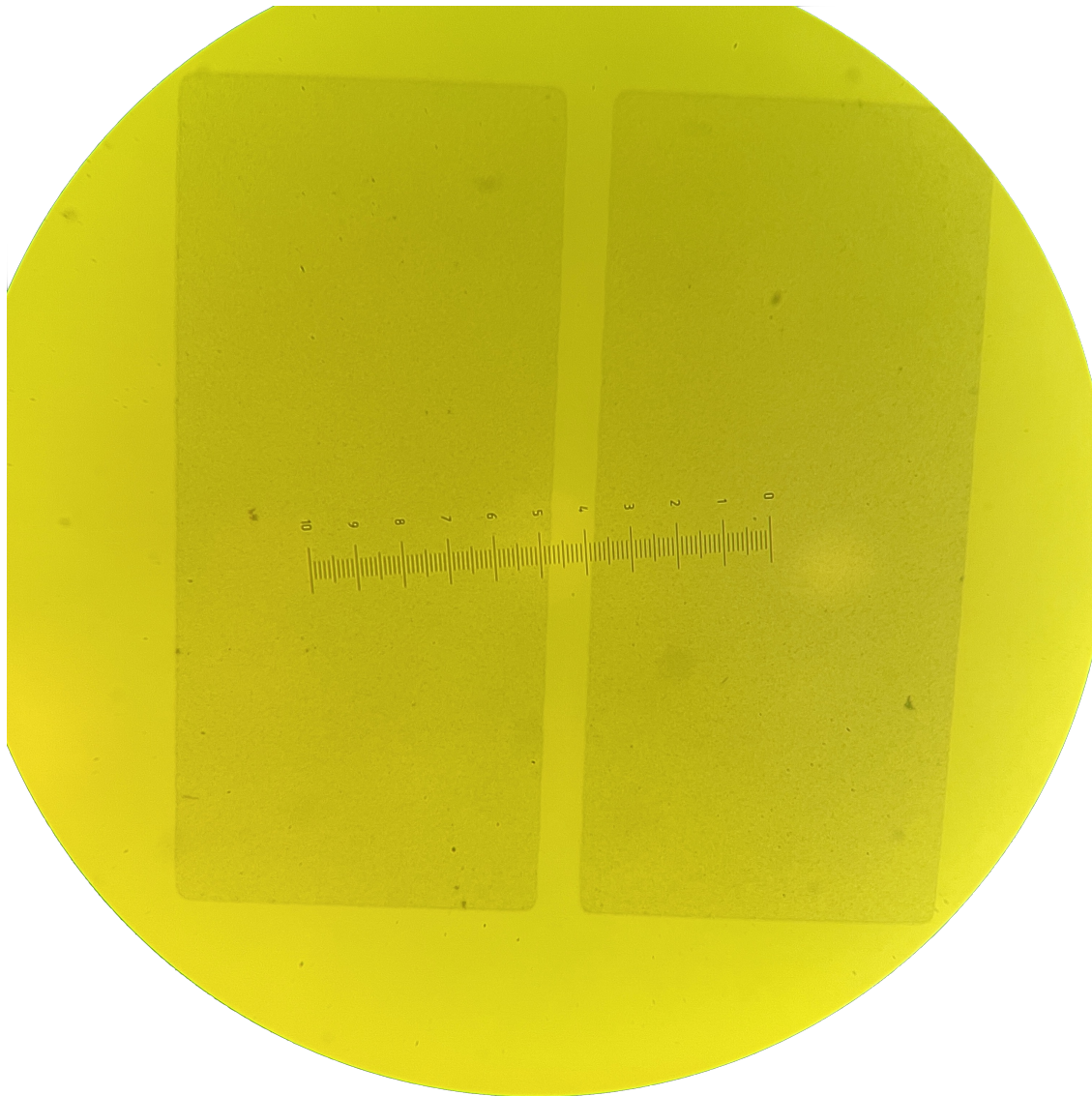


Figure 55: 100x objective: horizontal structures.

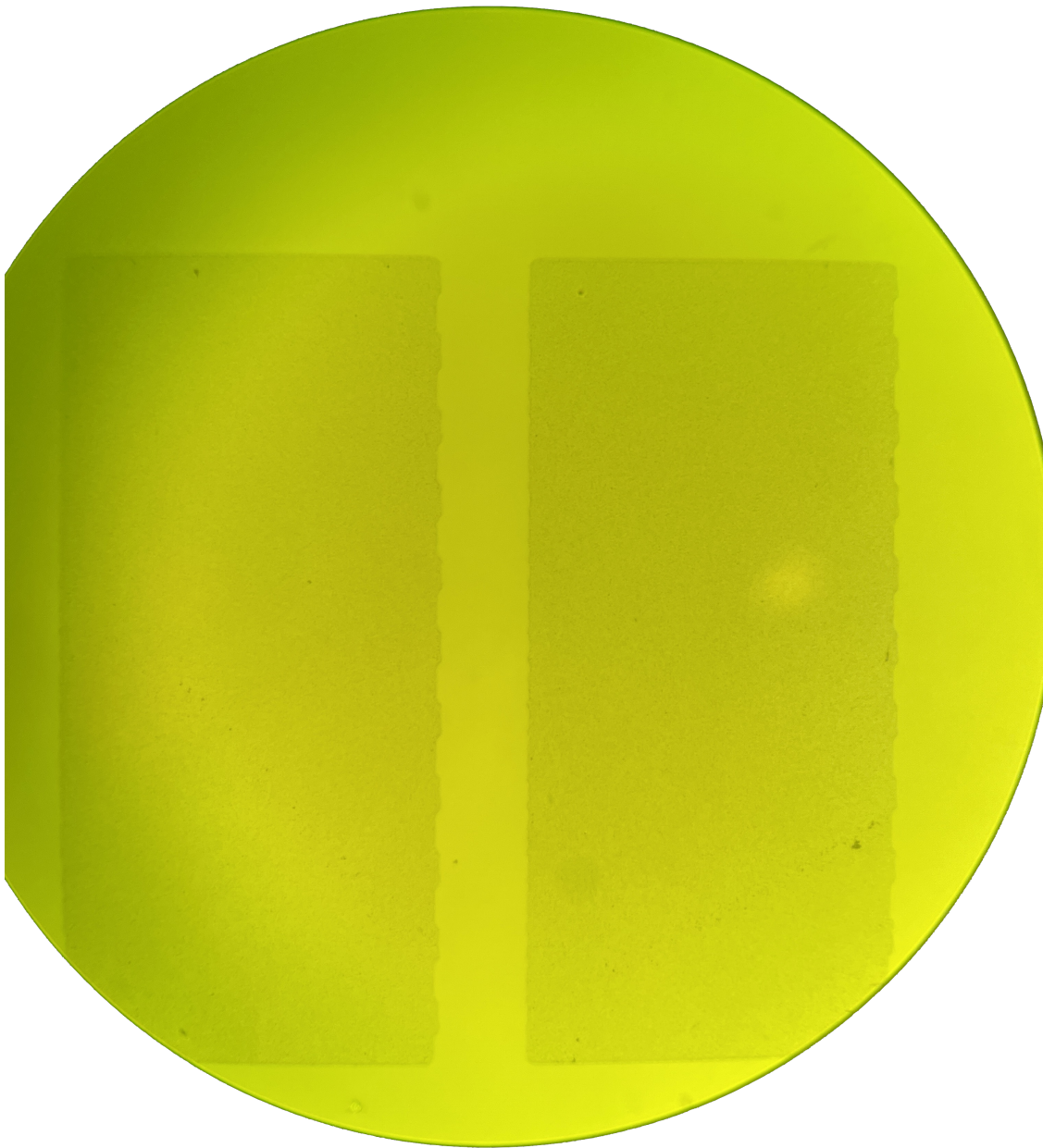


Figure 56: 100x objective: vertical structures with curved side.

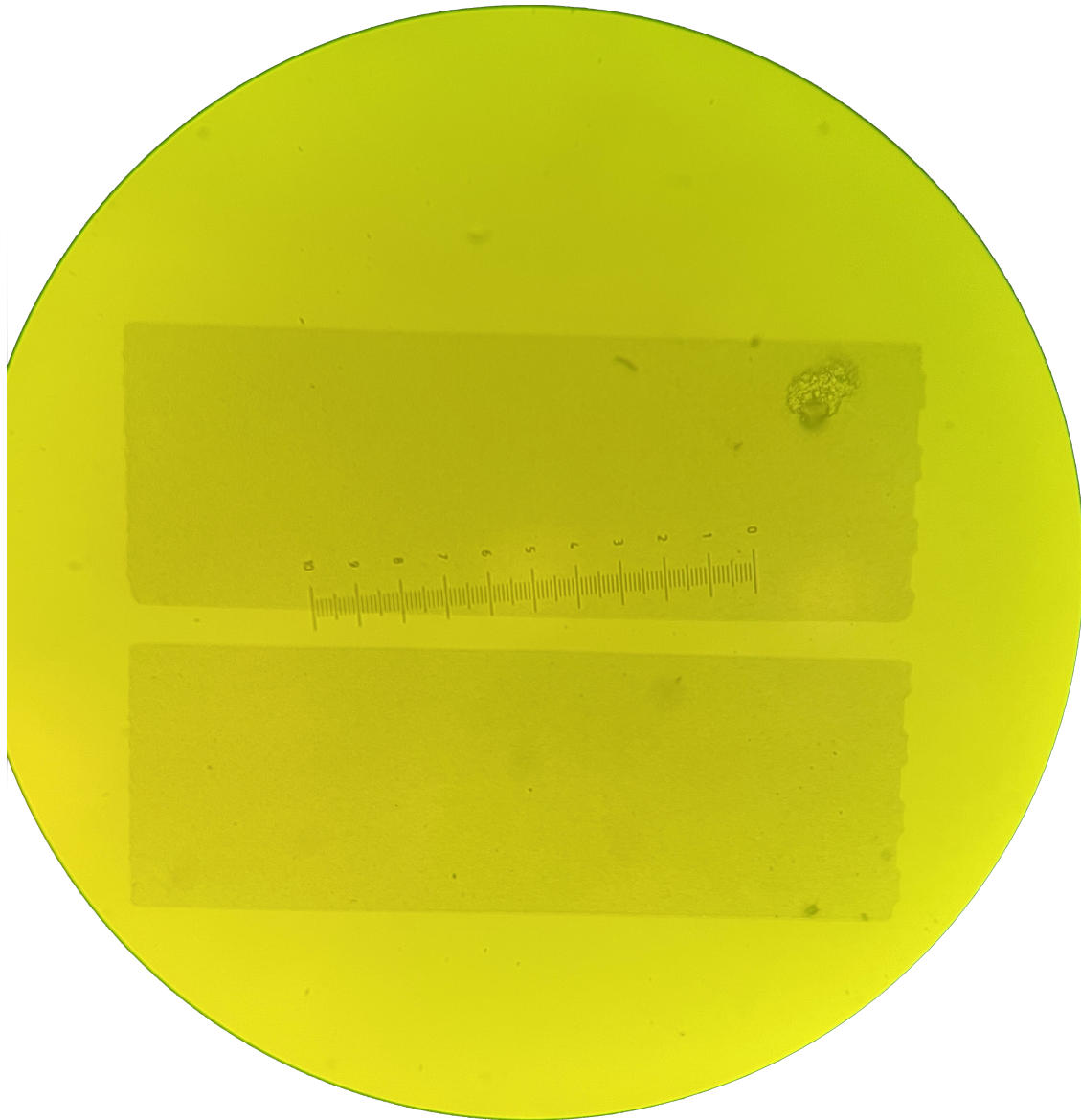


Figure 57: 100x objective: horizontal structures with curved side.



Figure 58: 100x objective: vertical tapered structures with curved side.

4.2.1 SEM Imaging

The scanning electron microscope (SEM) is a powerful technique that allows the study of material surfaces. At the earlier stages of this work, an InGaAs/GaAs quantum well heterostructure was grown by MOCVD on an n-type GaAs wafer. The semiconductor wafer processing is identical to that of the MBE samples. The differences between the samples are the doping of the substrate, the growth method, and the DH materials. This sample was analyzed using the SEM as shown in Figure 59. One of the most important features to notice is that none of the growth occurs on the silica, as expected.



Figure 59: SEM of the InGaAs/GaAs quantum well structure.

5 Conclusion & Future Work

The objective of this research is to advance semiconductor manufacturing methods for fiber optic communications. For WDM applications, single chip integration of functional components necessitates multiple laser wavelengths on a chip. SAG can accomplish this by simultaneously growing semiconductors with different bandgaps in a single epitaxial growth.

In this work, SAG was accomplished using a lithographic direct-write laser system that created silica masks deposited on the surface of a GaAs substrate. An InGaP/GaAs/InGaP heterostructure is grown using MBE to investigate SAG. There is no growth on silica structures due to the low sticking coefficient of SiO_2 . The growth will occur in the mask openings and any adatoms on the mask will migrate near the vicinity of the mask. A μ -PL apparatus with spatial resolution was successfully built to capture the emission spectrum. The PL was measured across the sample around the peak wavelength of 880 nm and was converted to an image of PL intensity. The images show that the silica structures did suppress the growth quality due to their lack of PL. The images also show a reduction in PL intensity in areas with many structures and especially near the mask edge. This is hypothesized to be due to variations in the InGaP layers that ultimately affect growth quality and carrier confinement.

According to literature, SAG leads to thickness and stoichiometric modulation laterally across the sample. The degree of modulation is dependent on multiple conditions: the growth method, the diffusion length of the material, the number of group-III precursors, and the type of heterostructure. To achieve high modulation in thickness and atomic content, MOCVD is used for selective area epitaxial growth and ternary or quaternary quantum well heterostructures are grown. Unlike the MOCVD, the MBE uses elemental group-III

materials making the suppression of growth on the masks more difficult.

This work paves the road for PL imaging of selectively grown heterostructure materials. The μ -PL apparatus can be further optimized and improved to allow for faster and clearer imaging. Future work can begin by trying to understand the behaviours of the InGaP and its effect on PL intensity. A possible first step is to look at the SEM image of the sample to analyze thickness variation. Another possibility is to grow bulk GaAs and InGaP separately on processed SI-GaAs wafers with silica structures to confirm which of these compounds is affecting the PL intensity. The next step is to selectively grow quantum well heterostructures using the MOCVD to achieve modulation that will result in PL wavelength shift across the sample. This will allow integration of multiple wavelength lasers on a chip for fiber optic transmission. This allows the development of faster, more reliable, and cheaper methods for manufacturing at the device level.

6 References

- [1] “Photonic integrated circuit,” Synopsys.com. [Online]. Available: <https://www.synopsys.com/glossary/what-is-a-photonic-integrated-circuit.html>. [Accessed: 07-Sep-2022].
- [2] Y. Koike and K. Koike, “Optical Fibers,” in *Polymer Science: A Comprehensive Reference*, Elsevier, 2012, pp. 283–304.
- [3] J. Sinopoli, “The foundations of a smart building,” in *Smart Building Systems for Architects, Owners and Builders*, Elsevier, 2010, pp. 7–30.
- [4] R. Tricker, “Optical Fibres in Power Systems,” in *Electrical Engineer’s Reference Book*, Elsevier, 2003, pp. 37-1-37–17.
- [5] M. Fujiwara, N. K. Dutta, and A. K. Dutta, *WDM Technologies: Active Optical Components*. San Diego, CA: Academic Press, 2002.
- [6] S. Chandrasekhar and X. Liu, “Advances in Tb/s Superchannels,” in *Optical Fiber Telecommunications*, Elsevier, 2013, pp. 83–119.
- [7] M. Sugiyama, “Selective area growth of III-V semiconductors: From fundamental aspects to device structures”, 22nd International Conference on Indium Phosphide and Related Materials (IPRM), 2010.
- [8] N. Dupuis et al., “Mask pattern interference in AlGaInAs selective area metal-organic vapor-phase epitaxy: Experimental and modeling analysis,” *J. Appl. Phys.*, vol. 103, no. 11, p. 113113, 2008.
- [9] E. Colas et al., “Lateral and longitudinal patterning of semiconductor structures by crystal growth on nonplanar and dielectric-masked GaAs substrates: application to thickness-modulated waveguide structures,” *J. Cryst. Growth*, vol. 107, no. 1–4, pp. 226–230, 1991.
- [10] D. Nirmal and J. Ajayan, “InP-based high-electron-mobility transistors for high-frequency applications,” in *Nanoelectronics*, Elsevier, 2019, pp. 95–114.
- [11] Z. Liu, W. Ma, and X. Ye, “Shape control in the synthesis of colloidal semiconductor nanocrystals,” in *Anisotropic Particle Assemblies*, Elsevier, 2018, pp. 37–54.
- [12] T. Motooka and T. Uda, “Multiscale Modeling Methods,” in *Handbook of Silicon Based MEMS Materials and Technologies*, Elsevier, 2015, pp. 241–252.

- [13] T. E. Schlesinger, "Gallium Arsenide," in *Encyclopedia of Materials: Science and Technology*, Elsevier, 2001, pp. 3431–3435.
- [14] S. Bhagyaraj, O. S. Oluwafemi, and I. Krupa, "Polymers in optics," in *Polymer Science and Innovative Applications*, Elsevier, 2020, pp. 423–455.
- [15] Z. I. Alferov, "Nobel Lecture: The double heterostructure concept and its applications in physics, electronics, and technology," *Rev. Mod. Phys.*, vol. 73, no. 3, pp. 767–782, 2001.
- [16] Y. Wan, J. Norman, and J. Bowers, "Quantum dot microcavity lasers on silicon substrates," in *Future Directions in Silicon Photonics*, Elsevier, 2019, pp. 305–354.
- [17] V. P. Chaly, S. Y. Karpov, A. L. Ter-Martirosyan, D. V. Titov, and W. Z. Guo, "Mechanisms of optical confinement in phase-locked laser arrays," *Semicond. Sci. Technol.*, vol. 11, no. 3, pp. 372–379, 1996.
- [18] Y.-Z. Huang, Z. Pan, and R.-H. Wu, "Analysis of the optical confinement factor in semiconductor lasers," *J. Appl. Phys.*, vol. 79, no. 8, p. 3827, 1996.
- [19] S. Sanguinetti, M. Guzzi, and M. Gurioli, "Accessing structural and electronic properties of semiconductor nanostructures via photoluminescence," in *Characterization of Semiconductor Heterostructures and Nanostructures*, Elsevier, 2008, pp. 175–208.
- [20] S. Nakamura, "Background story of the invention of efficient InGaN blue-light-emitting diodes (Nobel lecture)," *Angew. Chem. Int. Ed Engl.*, vol. 54, no. 27, pp. 7770–7788, 2015.
- [21] T. Goudon, V. Miljanović, and C. Schmeiser, "On the Shockley–read–hall model: Generation-recombination in semiconductors," *SIAM J. Appl. Math.*, vol. 67, no. 4, pp. 1183–1201, 2007.
- [22] H. Fu and Y. Zhao, "Efficiency droop in GaInN/GaN LEDs," in *Nitride Semiconductor Light-Emitting Diodes (LEDs)*, Elsevier, 2018, pp. 299–325.
- [23] P. J. Delfyett, "Lasers, Semiconductor," in *Encyclopedia of Physical Science and Technology*, Elsevier, 2003, pp. 443–475.
- [24] C. Weisbuch and J. Nagle, "The physics of the quantum well laser," *Phys. Scr.*, vol. T19A, pp. 209–214, 1987.

- [25] J. Gibson, "Optical Sources for Telecommunication," in *The Communications Handbook*, 2nd ed., J. D. Gibson, Ed. Boca Raton, FL: CRC Press, 2002.
- [26] M. Razeghi, "Optoelectronic devices based on III-V compound semiconductors which have made a major scientific and technological impact in the past 20 years," *IEEE J. Sel. Top. Quantum Electron.*, vol. 6, no. 6, pp. 1344–1354, 2000.
- [27] C. Mo, W. Fang, Y. Pu, H. Liu, and F. Jiang, "Growth and characterization of InGaN blue LED structure on Si(111) by MOCVD," *J. Cryst. Growth*, vol. 285, no. 3, pp. 312–317, 2005.
- [28] P. S. Dutta, H. L. Bhat, and V. Kumar, "The physics and technology of gallium antimonide: An emerging optoelectronic material," *J. Appl. Phys.*, vol. 81, no. 9, pp. 5821–5870, 1997.
- [29] E. Tournié et al., "GaSb lasers grown on silicon substrate for telecom applications," in *Molecular Beam Epitaxy*, Elsevier, 2018, pp. 625–635.
- [30] J. J. Hsieh, "Measured compositions and laser emission wavelengths of GaXIn_{1-X}As_yP_{1-y} layers lattice-matched TO InP Substrates," *J. Electron. Mater.*, vol. 7, no. 1, pp. 31–37, 1978.
- [31] Y.-L. Tsai and C.-H. Wu, "Reduced dislocation density of an InP/GaAs virtual substrate grown by metalorganic chemical vapor deposition," *Coatings*, vol. 12, no. 6, p. 723, 2022.
- [32] R. D. Dupuis, "III-V semiconductor heterojunction devices grown by metalorganic chemical vapor deposition," *IEEE J. Sel. Top. Quantum Electron.*, vol. 6, no. 6, pp. 1040–1050, 2000.
- [33] "Metalorganic Chemical Vapor Deposition (MOCVD)," k-Space Associates, Inc. [Online]. Available: <https://k-space.com/application/mocvd/>. [Accessed: 08-Sep-2022].
- [34] J. R. Arthur, "Molecular beam epitaxy," *Surf. Sci.*, vol. 500, no. 1–3, pp. 189–217, 2002.
- [35] G. Bacchin, K. Tsunoda, and T. Nishinaga, "Selective area growth of AlGaAs on GaAs by PSE/MBE," *J. Cryst. Growth*, vol. 174, no. 1–4, pp. 616–621, 1997.
- [36] C. Caneau, R. Bhat, C. C. Chang, K. Kash, and M. A. Koza, "Selective organometallic vapor phase epitaxy of Ga and In compounds: a comparison of TMIn and TEGa versus TMIn and TMGa," *J. Cryst. Growth*, vol. 132, no. 3–4, pp. 364–370, 1993.

- [37] M.-S. Kim, C. Caneau, E. Colas, and R. Bhat, "Selective area growth of InGaAsP by OMVPE," *J. Cryst. Growth*, vol. 123, no. 1–2, pp. 69–74, 1992.
- [38] C. Caneau, R. Bhat, M. R. Frei, C. C. Chang, R. J. Deri, and M. A. Koza, "Studies on the selective OMVPE of (Ga,In)/(As,P)," *J. Cryst. Growth*, vol. 124, no. 1–4, pp. 243–248, 1992.
- [39] G. Bacchin and T. Nishinaga, "A detailed comparison of the degree of selectivity, morphology and growth mechanisms between PSE/MBE and conventional MBE," *J. Cryst. Growth*, vol. 198–199, pp. 1130–1135, 1999.
- [40] Q. Zhang, D. Sando, and V. Nagarajan, "Chemical route derived bismuth ferrite thin films and nanomaterials," *J. Mater. Chem. C Mater. Opt. Electron. Devices*, vol. 4, no. 19, pp. 4092–4124, 2016.
- [41] R. E. Sah et al., "Room-temperature, high-deposition-rate, plasma-enhanced chemical vapour deposition of silicon oxynitride thin films producing low surface damage on lattice-matched and pseudomorphic III–V quantum-well structures," *Thin Solid Films*, vol. 259, no. 2, pp. 225–230, 1995.
- [42] Y. Dong, R. M. Feenstra, M. P. Semtsiv, and W. T. Masselink, "Band offsets of InGaP-GaAs heterojunctions by scanning tunneling spectroscopy," *J. Appl. Phys.*, vol. 103, no. 7, p. 073704, 2008.